Stony Brook University

Overall properties of piezoelectric particulate composites: Homogenization estimates and finite-element simulations

A Thesis Presented
by
Sumantu Kaushik Iyer

to
The Graduate School
in Partial Fulfillment of the Requirements
for the Degree of
Master of Science
in
Mechanical Engineering
Stony Brook University

December 2010

Stony Brook University

The Graduate School

Sumantu Kaushik Iyer

We, the thesis committee for the above candidate for
the degree of Master of Science,
hereby recommend acceptance of this thesis.

Oscar Lopez-Pamies - Thesis Advisor
Assistant Professor, Department of Mechanical Engineering

T. A. Venkatesh - Thesis Advisor, Chairperson of Defense
Assistant Professor, Department of Materials Science and Engineering

Robert Kukta
Associate Professor, Department of Mechanical Engineering

This thesis is accepted by the Graduate School.

Lawrence Martin
Dean of the Graduate School

Abstract of the thesis

Overall properties of piezoelectric particulate composites: Homogenization estimates and finite-element simulations

by

Sumantu Kaushik Iyer

Master of Science

in

Mechanical Engineering

Stony Brook University

2010

This work presents a) an analytic model based on homogenization estimates to obtain explicit solutions for the effective properties of particulate piezoelectric composites and b) a three-dimensional finite-element model to compare finite-element results and study the behaviour of porous piezoelectric composites with four different geometric configurations. The analytic model extends the Suquet [29] estimates method to the piezoelectric domain where a complete set of electromechanical constants are obtained for three piezoelectric ceramics belonging to different symmetry classes. Specific results are generated for the cases of a square arrangement of cylindrical pores, where the alignment

of the pores is in the direction of poling of the matrix phase and a cubic arrangement of spherical pores. The trends obtained from the analytic model are compared with the finite-element model and found to be in good agreement for all components of effective piezoelectric constants upto large volume fractions. A three-dimensional finite element model is developed in part II of the thesis to completely characterize the behaviour of a general porous piezoelectric composite with pores of 0-3 type flat cuboidal, 0-3 type cylindrical, 0-3 type spherical, and 1-3 type cylindrical connectivities. By considering materials from different symmetry classes, it is demonstrated that piezoelectric composites designed with 0-3 type flat cuboidal pores are more suitable for hydrophone applications by identifying the variation in piezoelectric strain coefficient and the hydrostatic figure of merit with varying porosity volume fraction.

To my parents.

Contents

List of Figures

Acknowledgments

I would like thank my adivsors Prof. Oscar Lopez-Pamies and Prof. T. A. Venkatesh for their patience and guiding me in my effort to complete a comprehensive Masters thesis. Prof. Oscar Lopez having supervised the analytic part of the thesis and Prof Venkatesh the finite-element. A special mention would have to be made towards the grant from the National Science Foundation under Grant No. DMR-0836763 to Prof. Venkatesh's group which helped support the work carried out by me in his lab.

I would like to thank all the students working in Prof. Venkatesh's group: Srivatsa Bhat, Ming Tian and Guang Chen. I appreciate all the help and assistance they have provided me with over the last two years.

CHAPTER 1

Introduction

Piezoelectric materials have been investigated due to their unique property of coupling mechanical stress with a charge distribution on the surface. Shortcomings of monolithic piezoelectric materials(e.g. brittleness, environmental concerns, etc.) have led to the research of composite piezoelectric materials, for e.g. Xu et al. [40] developed sodium bismuth titanate (NBT) based piezoelectric materials using a citrate method as an alternative to lead based piezoelectric materials. It was found that piezoelectric composites can be fabricated such that the overall elastic, piezoelectric and dielectric properties can be enhanced. The two main approaches used to fabricate piezoelectric composites are - the additive approach, wherein a piezoelectrically active stiffer fiber phase is introduced into a complaint matrix phase thereby enhancing the overall electromechanical properties and figures of merit and the subtractive approach where controlled porosity is introduced into a piezoelectrically active matrix phase, thereby enhancing the piezoelectric charge coefficient (d_h) and hydrostatic figure of merit ($d_h g_h$) making them useful in hydrophone sensing applications [32, 14, 6, 5]. Many analytic theories have been proposed to explain the behaviour of piezoelectric composite materials. The first mention of the tensors and equations encountered in the realm of piezoelectric coupled phenomenon was made by Nye [33]. The initial theories that were proposed to explain the behaviour of piezoelectric composites were based on a "series",

"parallel" model [15] of Banno [2]. Their theories provided a good approximation for 2-2 type laminate composites. The next attempt to characterize the behaviour piezoelectric composites was made by [25, 27, 26]. The author extended the matrix method of Hashimoto to solve for the effective electromechanical properties of 1-3, 0-3, and 3-3 type piezoelectric composites. However the models were quite simplistic and provided good estimates for limited geometric configurations of inclusions embedded in a piezoelectric matrix.

Various experimental and analytic models have been developed to study the benefits of porous piezoelectric composites. For example, Haun and Newnham fabricated 1-3 and 1-3-0 type piezoelectric lead zirconate titanate (PZT)-Polymer composites using a single large void at the centre of the composite and showed that such a composite significantly enhances the hydrophone sensing abilities by increasing d_h and $d_h g_h$ [17]. Guy and Chan investigated the electromechanical properties of 1-3 piezoelectric composites where the polymer as well as the ceramic phase was piezoelectrically active [35]. The techniques adopted to fabricate the desired composite were layering and dice and fill. Problems encountered during the process of filling include reducing damage to the ceramic rods. Both type of composites yielded results that under predicted the values piezoelectric coefficients when compared with results from modeling . Ting studied the effects of several materials and processing parameters on the piezoelectric properties and identified an epoxy coating on a porous sample to generate improved piezoelectric figures of merit [36]. Bast and Wersing showed that the acoustic impedance (Z) for PZT materials with 3-1-type porosity decreases with increasing porosity volume fraction [3].

Even though some work had been done to extend Eshelby's solution [14] for anisotropic inclusions in the elastic domain [16, 37, 24, 38] no closed-form solution could be obtained for the components of the Eshelby tensor. A numerical scheme having been employed thereby to solve for the components of the Eshelby tensor for an anisotropic matrix [8]. Banno used a modified cubes model to explain the behaviour of composite piezoelectric materials.

The analytical solutions obtained by him were able to characterize the coupled response of piezoelectric ceramics with closed pores (3-0 type) and open pores (3-1 type) [2]. Prior work done by Deeg [10] and Wang [39] was extended by Dunn and Taya [11] in their solution to the piezoelectric inclusion problem. An alternate solution to the inclusion problem was studied by Beneveniste [4] and Chen [9] who extended the generalized solution of Hill and Walpole. Even though each had obtained the four tensors that comprise the equivalent of the Eshelby tensor in the piezoelectric domain none provided explicit closed-form expressions for them. Dunn et al. [13, 12] gave the explicit forms for the equivalent Eshelby tensor in terms of a surface integral over a unit sphere evaluated numerically. Mikata derived explicit solutions for the components of the Eshelby tensor by solving a "special" bi-cubic equation [30] which was specialized for the case of spheroidal inclusions in [31]. Topolov and Bowen provided a method to predict the behaviour of closed pore (0-3 type) and interconnected (3-3 type) phases [7]. Their paper is aimed at the comparative study of 0-3 and 3-3 composites containing $PbTiO_3$ based piezocomposite ceramics by varying the anisotropy factor $-d_{33}/d_{31}$. Gomez and Espinosa derived a model to predict the dielectric properties of porous piezoelectric materials and the dielectric coupling generated by the introduction of a second phase to the pores as well. Based on thermodynamic considerations, Gomez et al. identified solutions for the effective electromechanical constants of both porous and composite piezoelectric materials [1].

Finite element based models were developed by Pettermann and Suresh to predict the behaviour of long fibers (1-3 type). The linear response to mechanical and electric loading was determined for unidirectional fibers arranged in periodic hexagonal and square distributions [34]. A three dimensional finite element model was used by Kar-Gupta and Venkatesh to study the behaviour of various porous composite systems consisting of different alignment of the pores [20], pores being of the 1-3 type. They were able to completely characterize the electromechanical behaviour of the unit cell by applying mechanical and electrical loading through the master nodes [23, 22, 21, 19]. Bisegna and

Luciano [6, 5] provided variational bounds to estimate the homogenized properties of piezoelectric composites.

Overall, a comprehensive set of models and results exist to explain the behaviour of 1-3 long fibers and 0-3 closed pores. However there exist limited analytical models that explain the behaviour of porous piezoelectric materials other than 1-3 long pores and spheroidal 0-3 pores. The present work comprises of a study of pores of different geometric connectivity, highlighting the advantages of each and their potential use in select applications. The objectives of the present study are as follows: i) to develop a finite element based numerical model to study the behaviour of four distinct pore geometries of 1-3 cylindrical long pore, 0-3 short cylindrical pore, 0-3 spherical pore, and 0-3 flat cuboidal pore; ii) to identify the effects of porosity volume fraction, geometry, and orientation on the effective response of the porous piezoelectric material; iii) to study the effects of porosity geometry on figures of merit of piezoelectric materials.

To date, the existing analytic models have not provided closed-form solutions to anisotropic particulate inclusions in a piezoelectric matrix. Part I of the thesis focuses on building a theory to find the effective properties of homogenized piezoelectric composites with periodic microstructure. Results obtained from the theory are compared and found to be in good agreement with finite element model predictions. The present work is outlined as follows. Section 2 contains the mathematical formulation of the piezoelectric problem, constitutive equations, periodic fields, and jump conditions. Section 3 highlights the concepts used to solve the equilibrium equations. Fourier analysis is used to convert the equilibrium equations from differential equations to algebraic equations, piecewise constant polarization fields are introduced to simplify the equations for strain and electric field. In subsection 3.2 the equations for strain and electric field are solved for a two phase periodic composite. Section 4 looks at the derivation of the concentration tensors used to relate the average strains in the phases to the strains on the boundary. Expressions for the effective

properties are provided in terms of the concentrations tensors. Part II of the thesis present work is outlined as follows. Section 5 contains the classification of 1-3-type and 0-3-type porous piezoelectric composites. Section 6 highlights the constitutive relations that govern the behaviour of coupled piezoelectric materials in the linear elastic domain. Section 7 defines the characteristic figures of merit of significance to the applications of piezoelectric composite materials (e.g., in sensors). Section 8 looks at an available analytic model that provides solutions for the electromechanical constants of porous piezoelectric composites for select geometric constraints. Section 9 contains the details of the finite element-based numerical model used to study the effects of porosity on the electro elastic behaviour in piezoelectric composite materials for a wide range of geometric conditions. Section 10 reviews the results of the finite element-based numerical model and its implications. It contains plots based on the analytic model predictions compared with finite element models. Finally, concluding remarks are made with respect to current research and a possible direction for further study. Section 11 summarizes the inferences drawn from the study.

Part I

Homogenization estimates of piezoelectric particulate composites

CHAPTER 2

Preliminaries on piezoelectric composites with periodic microstructure

Consider an infinitely large composite made up of aligned long cylindrical fibers distributed periodically in a piezoelectric matrix phase i.e., the information about the microstructure is complete as opposed to the random case where only partial information is available about the microstructure of the composite. It is assumed here when discussing 'effective properties' that there is a separation of length-scales within the problem. The local or microscopic scale is one where the heterogeneities can be identified separately as shown in Fig.1. The macroscopic or overall scale is one where the heterogeneities can be 'averaged-out' A given sample of this material is assumed to occupy a volume Ω, with boundary $\partial\Omega$. The effective properties at the macroscopic scale are determined using geometric and material data of an appropriate representative volume element or unit cell. The infinitely large composite body can be generated by adding contiguously the unit cell in all three directions.

A material point within the given specimen is denoted by $\mathbf{x}$ (at the microscopic level). The symmetric part of the deformation gradient tensor, $\boldsymbol{\varepsilon}$, at $\mathbf{x}$

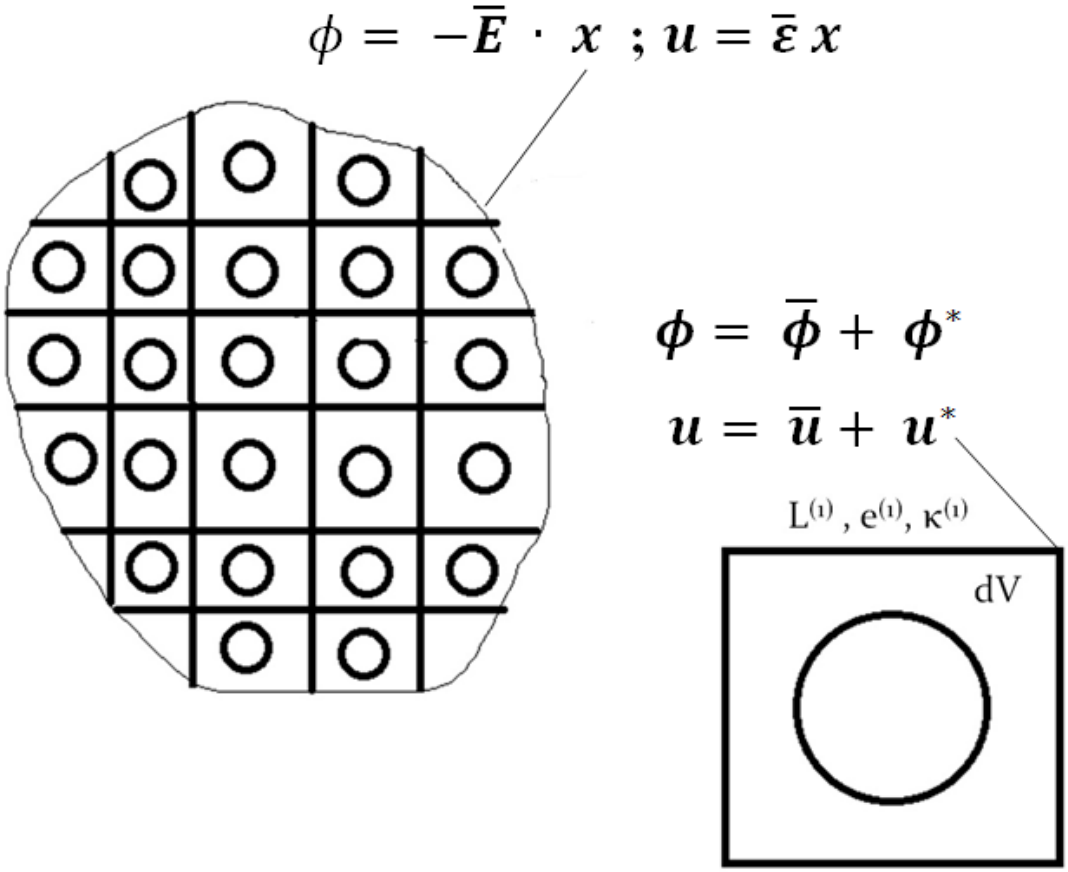

Figure 1: The schematic diagram of an infinite piezoelectric composite and representative volume fraction.

is defined for a displacement field, $\boldsymbol{u}$ as:

$$\varepsilon_{ij} = \frac{1}{2}(u_{i,j} + u_{j,i}) \tag{1}$$

The electric field, $\mathbf{E}$ is given as the gradient of a scalar potential ϕ and is defined as:

$$E_n = -\phi_{,n} \tag{2}$$

The constitutive behaviour of the matrix and the cylindrical fibers is assumed to be linear elastic and characterized, by the stored-energy functions, $W^{(1)}$ and $W^{(2)}$ respectively. The two functions are taken to be convex functions of the strain($\boldsymbol{\varepsilon}$) and electric field($\mathbf{E}$), so that the local energy function of the composite may be written as:

$$W(\mathbf{x}, \boldsymbol{\varepsilon}, \boldsymbol{E}) \;\; = \;\; (1 - \chi(\mathbf{x})W^{(1)}(\boldsymbol{\varepsilon}, \boldsymbol{E}) + \chi(\mathbf{x})W^{(2)}(\boldsymbol{\varepsilon}, \boldsymbol{E}) \tag{3}$$

where, χ is known as the characteristic function, equal to 1 if the position vector $\mathbf{x}$ is inside phase r and zero otherwise, describes the distribution of the phases (i.e.,the microstrucuture). Moreover, since the microstructure of the given composite is periodic a unit cell of volume,D, can be taken as a parallelopiped of dimensions,L_i, where, $i = (1, 2, 3)$, the periodic characteristic functions can be written as:

$$\chi^{(r)}(X_1, X_2, X_3) = \chi^{(r)}(X_1 + z_1L_1, X_2 + z_2L_2, X_3 + z_3L_3) \tag{4}$$

z_1, z_2, z_3 being arbitrary integers. Since piezoelectricity is a linear phenomenon the work function,$W^{(r)}(r = 1, 2)$, is assumed to be a convex function. The local constitutive behaviour for the composite is given by:

$$\boldsymbol{\sigma} = \frac{\partial W}{\partial \boldsymbol{\varepsilon}}(\boldsymbol{\varepsilon}, \boldsymbol{E}), \tag{5}$$

and

$$\boldsymbol{D} = -\frac{\partial W}{\partial \boldsymbol{E}}(\boldsymbol{\varepsilon}, \boldsymbol{E}) \tag{6}$$

where, $\boldsymbol{\sigma}$ is the Cauchy stress tensor and $\boldsymbol{D}$ is the electric displacement vector.

The effective stored energy function,$\widetilde{W}$, of the two-phase piezoelectric composite under the separation of length scales hypothesis is given by,

$$\widetilde{W}(\overline{\boldsymbol{\varepsilon}}, \overline{\boldsymbol{E}}) = \min_{\boldsymbol{\varepsilon} \in \mathcal{K}(\overline{\boldsymbol{\varepsilon}})} \max_{\boldsymbol{E} \in \mathcal{J}(\overline{\boldsymbol{E}})} \sum_{r=1}^{2} c^{(r)} \langle W^{(r)}(\boldsymbol{\varepsilon}, \boldsymbol{E}) \rangle^{(r)} \tag{7}$$

where $\mathcal{K}$ denotes the set of all kinematically admissible strain fields:

$$\mathcal{K}(\overline{\boldsymbol{\varepsilon}}) = \{\boldsymbol{\varepsilon} | \text{ with } \boldsymbol{\varepsilon} = \frac{1}{2}\left(\nabla \boldsymbol{u} + \nabla \boldsymbol{u}^{\boldsymbol{T}}\right) \text{ in } \Omega, \ \boldsymbol{u} = \overline{\boldsymbol{\varepsilon}}\mathbf{x} \text{ on } \partial\Omega\} \tag{8}$$

and

$$\mathcal{J}(\overline{\boldsymbol{E}}) = \{\boldsymbol{E} | \text{ with } \boldsymbol{E} = \nabla \phi \text{ in } \Omega, \ \phi = -\overline{\boldsymbol{E}} \cdot \mathbf{x} \text{ on } \partial\Omega\} \tag{9}$$

In all the expressions presented above, the triangular brackets $\langle \cdot \rangle$ and $\langle \cdot \rangle^{(r)}$ denote, respectively, the volume averages over the specimen,(Ω), and the phase r $(\Omega^{(r)})$. The scalars, $c^{(1)}$ and $c^{(2)}$ denote the volume fractions of the two constituent phases of the periodic composite. It is also important to note that the average electroelastic energy, $\widetilde{W}$, stored in the fibre-reinforced composite when subjected to an affine strain and electric field is consistent with the condition $\langle \boldsymbol{\varepsilon} \rangle = \overline{\boldsymbol{\varepsilon}}$. From the arguments presented above we can then say that the macroscopic constitutive behaviour for composite can then be expressed by:

$$\overline{\boldsymbol{\sigma}} = \frac{\partial \widetilde{W}}{\partial \overline{\boldsymbol{\varepsilon}}} \text{ and } \overline{\boldsymbol{D}} = -\frac{\partial \widetilde{W}}{\partial \overline{\boldsymbol{E}}} \tag{10}$$

where, $\overline{\boldsymbol{\sigma}} = \langle \boldsymbol{\sigma} \rangle$ and $\overline{\boldsymbol{D}} = \langle \boldsymbol{D} \rangle$ are the average stress and the average electric displacement in the fibre-reinforced composite respectively.

The variational problem for electroelastic composites in the linear elastic domain (7) with periodic microstructure can be expressed explicitly as follows:

$$\widetilde{W}(\mathbf{x}, \overline{\boldsymbol{\varepsilon}}, \overline{\boldsymbol{E}}) = \min_{\boldsymbol{\varepsilon} \in \mathcal{K}(\overline{\boldsymbol{\varepsilon}})} \max_{\boldsymbol{E} \in \mathcal{J}(\overline{\boldsymbol{E}})} \frac{1}{|D|} \int_D W(\mathbf{x}, \boldsymbol{\varepsilon}, \boldsymbol{E}) \mathrm{d}\mathbf{x} \tag{11}$$

CHAPTER 3

Suquet estimates for linear piezoelectric constituents

Based on the framework presented in the previous section, the main objective of the current study is to provide explicit homogenization estimates for the electromechanical properties of a periodic distribution of particulate inclusions/exclusions of arbitrary geometrical shape in a general piezoelectric matrix phase of anisotropic material symmetry. This is accomplished by extending Suquet's homogenization estimates [29] to the domain of periodic piezoelectric composites. This method has already been applied to elastic materials and provides good estimates for the effective properties of composite materials with periodic microstructure. It uses the assumption of piece-wise constant polarization fields in the phases(zero in the matrix phase), converting the equilibrium equations into algebraic equation by using Fourier transform and the use of concentration tensors to express effective properties in terms of the properties of the constituent phases. This section outlines the basic framework of how the Suquet estimates have been used to derive estimates for effective electromechanical constants.

Making use of the results provided by Suquet for two-phase composites with periodic microstructure, an estimate for the overall stored-energy function, $\widetilde{W}$ is provided using the volume fraction of the fibres, $c^{(2)}$, with stored-energy

function, $W^{(2)}$, distributed periodically in a piezoelectric matrix with stored-energy function,$W^{(1)}$.

The linear constitutive equations derived from 5 and 6 are written as:

$$\sigma_{ij} = L_{ijkl}\varepsilon_{kl} + e_{kij}\phi_{,k} \tag{12}$$

$$D_i = e_{ikl}\varepsilon_{kl} - \kappa_{ik}\phi_{,k} \tag{13}$$

The above relations 12 and 13 are the linear constitutive relations that characterize the complete electromechanical response of a piezoelectric composite. The following tensors, $\boldsymbol{L, e, \kappa}$, denote the fourth-order elastic modulus tensor with major and minor symmetry, the piezoelectric constants tensor with minor symmetry in i and j, and the dielectric constants tensor with major symmetry. In addition the piezoelectric composite has to satisfy the following stress equilibrium and Maxwell's equations respectively:

$$\frac{\partial \sigma_{ij}}{\partial x_j} = \left[L_{ijkl}\varepsilon_{kl} + e_{kij}\phi_{,k}\right]_{,j} = 0 \tag{14}$$

$$\frac{\partial D_i}{\partial x_i} = \left[e_{ikl}\varepsilon_{kl} - \kappa_{ik}\phi_{,k}\right]_{,i} = 0 \tag{15}$$

At this point it is useful to introduce a homogeneous reference medium [16] with constant properties Fig.2 ($\boldsymbol{L^{(0)}, e^{(0)}, \kappa^{(0)}}$) and piece-wise constant polarization fields defined by, $\boldsymbol{\tau^{(L)} = [L^{(r)} - L^{(0)}]\varepsilon}$, $\boldsymbol{\tau^{(cE)} = [e^{(r)} - e^{(0)}]E}$, $\boldsymbol{\tau^{(c\varepsilon)} = [e^{(r)} - e^{(0)}]\varepsilon}$, $\boldsymbol{\tau^{(\kappa)} = [\kappa^{(r)} - \kappa^{(0)}]E}$. The form of the equilibrium equations for stress on the introduction of the reference medium and the polarization fields is:

$$\sigma_{ij,j} = L^{(0)}_{ijmn}u_{m,nj} + \tau^{(L)}_{ij,j} + e^{(0)}_{kij}\phi_{,kj} + \tau^{(cE)}_{ij,j} \tag{16}$$

where $u_{m,n}$ and $-\phi_{,k}$ is used to denote the strain and electric field respectively.

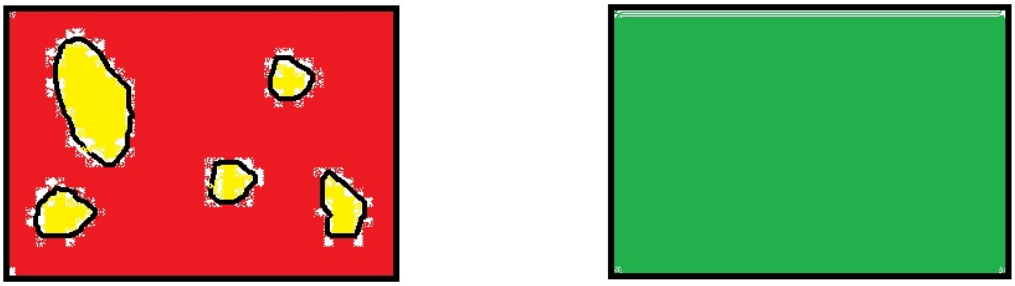

Figure 2: The schematic diagram shows a heterogeneous material (red and yellow) with varying material parameters and a reference medium with constant material parameters (green).

The local problem for the displacement and electric field can be split into its overall and periodic parts such that $\boldsymbol{u} = \overline{\boldsymbol{u}} + \boldsymbol{u}^*$ and $\boldsymbol{\phi} = \overline{\boldsymbol{\phi}} + \boldsymbol{\phi}^*$. The equilibrium equations for stress can then be written as the super-position of the strain and electric fields are:

$$L^{(0)}_{ijmn}\overline{u}_{m,nj} + e^{(0)}_{nij}\overline{\phi}_{,nj} = 0 \tag{17}$$

where polarization constant is $\tau^{(\gamma)}_{ij,j} = 0$ for $\gamma = 1, 2$ in the matrix, and

$$L^{(0)}_{ijmn}u^*_{m,nj} + e^{(0)}_{nij}\phi^*_{,nj} + \tau^{(L)}_{ij,j} + \tau^{(cE)}_{ij,j} = 0. \tag{18}$$

Similarly for the equilibrium of electric displacement the following equations are derived as:

$$e^{(0)}_{imn}\overline{u}_{m,ni} - \kappa^{(0)}_{in}\overline{\phi}_{,ni} = 0 \tag{19}$$

$$e^{(0)}_{imn}u^*_{m,ni} + \tau^{(c\varepsilon)}_{i,i} - \kappa^{(0)}_{in}\phi^*_{,ni} + \tau^{(\kappa)}_{i,i} = 0 \tag{20}$$

3.1 Fourier analysis

To solve the equilibrium equations, Fourier transform method is used to convert the system of partial differential equations to linear equations. The form

of the equation 18 in Fourier space is given by:

$$\widehat{u^*_{m,n}} = (N^0_{im})\xi_j\xi_n[-e^{(0)}_{pij}\widehat{\phi^*_{,p}} - \widehat{\tau_{ij}}^{(L)} - \widehat{\tau_{ij}}^{(cE)}] \tag{21}$$

$$\widehat{u^*_{m,n}} = -J_{mnp}\widehat{\phi^*_{,p}} - H_{ijmn}\widehat{\tau_{ij}}^{(L)} - H_{ijmn}\widehat{\tau_{ij}}^{(cE)} \tag{22}$$

where, $H_{ijmn} = (N^0_{im})\xi_j\xi_n$ and $\boldsymbol{N^0(\xi)}$ is the inverse of the acoustic tensor of the homogeneous material, $\boldsymbol{\xi}$ being a position vector in Fourier space, $J_{mnp} = H_{ijmn}e^{(0)}_{pij}$ and i $= \sqrt{-1}$.
Similarly converting the equation 19 to Fourier space and solving for the electric field we get,

$$\widehat{\phi^*_{,k}} = \left[\kappa^{(0)}_{pq}\xi_p\xi_q\right]^{-1}\xi_i\xi_k[e^{(0)}_{imn}\widehat{u^*_{m,n}} + \widehat{\tau}_i^{(c\varepsilon)} - \widehat{\tau}_i^{(\kappa)}] \tag{23}$$

$$\widehat{\phi^*_{,k}} = J_{kmn}\widehat{u^*_{m,n}} + G_{ik}\widehat{\tau}_i^{(c\varepsilon)} - G_{ik}\widehat{\tau}_i^{(\kappa)} \tag{24}$$

where, $G_{ik} = [\kappa^{(0)}_{pq}\xi_p\xi_q]^{-1}\xi_i\xi_k$ and $J_{kmn} = G_{ik}e^{(0)}_{imn}$.

The basis vectors for a long fibre system in Fig.3 are given below:
Base vectors

$$\boldsymbol{y_1} = l(1,0,0) \tag{25}$$

$$\boldsymbol{y_2} = l(0,1,0) \tag{26}$$

$$\boldsymbol{y_3} = l(0,0,N) \tag{27}$$

where, $N \to \infty$ Base vectors in reciprocal lattice

$$\boldsymbol{g_1} = 2\pi\frac{\boldsymbol{y_2}\times\boldsymbol{y_3}}{\boldsymbol{y_1}\cdot(\boldsymbol{y_2}\times\boldsymbol{y_3})} = 2\pi(\frac{1}{l},0,0) \tag{28}$$

$$\boldsymbol{g_2} = 2\pi\frac{\boldsymbol{y_3}\times\boldsymbol{y_1}}{\boldsymbol{y_1}\cdot(\boldsymbol{y_2}\times\boldsymbol{y_3})} = 2\pi(0,\frac{1}{l},0) \tag{29}$$

$$\boldsymbol{g_3} = 2\pi\frac{\boldsymbol{y_1}\times\boldsymbol{y_2}}{\boldsymbol{y_1}\cdot(\boldsymbol{y_2}\times\boldsymbol{y_3})} = 2\pi(0,0,\frac{1}{N}) \tag{30}$$

$$\boldsymbol{\xi} = \frac{2\pi}{l}(p) + \frac{2\pi}{l}(q) \tag{31}$$

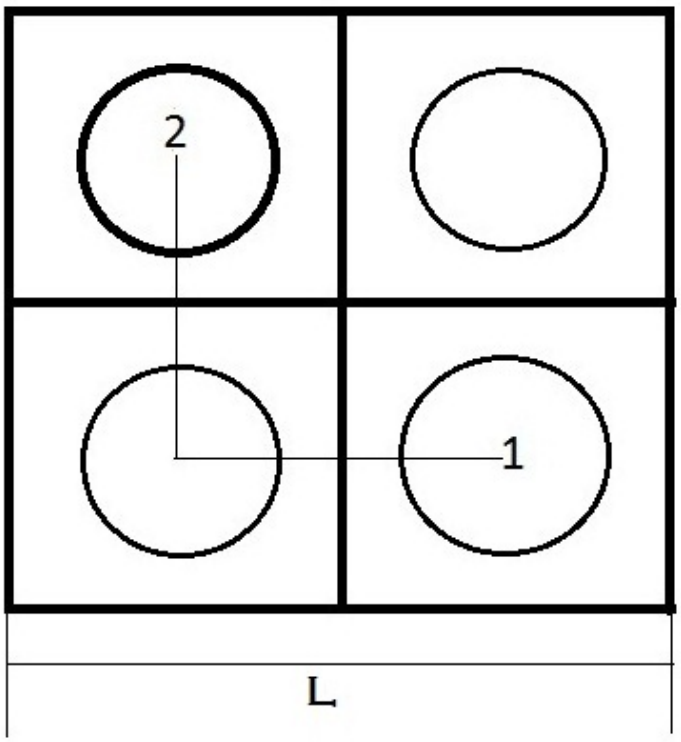

Figure 3: The schematic diagram shows a square distribution of long cylindrical fibres aligned with the direction of poling.

Substituting 24 in 22

$$\begin{aligned}\widehat{u^*_{m,n}} &= -J_{mnp}\left[J_{pkl}\widehat{u^*_{k,l}} + G_{sp}\widehat{\tau}_s^{(c\varepsilon)} - G_{sp}\widehat{\tau}_s^{(\kappa)}\right] - H_{ijmn}\widehat{\tau_{ij}}^{(L)} - H_{ijmn}\widehat{\tau_{ij}}^{(cE)} \\ \widehat{u^*_{m,n}} &= -J_{mnp}J_{pkl}\widehat{u^*_{k,l}} - J_{mnp}G_{sp}\left\{\widehat{\tau}_s^{(c\varepsilon)} - \widehat{\tau}_s^{(\kappa)}\right\} - H_{ijmn}\left\{\widehat{\tau_{ij}}^{(L)} + \widehat{\tau_{ij}}^{(cE)}\right\}\end{aligned} \tag{32}$$

Solving for the periodic strain

$$\left[I_{mnkl} + J_{mnp}J_{pkl}\right]\widehat{u^*_{k,l}} = -J_{mnp}G_{sp}\left\{\widehat{\tau}_s^{(c\varepsilon)} - \widehat{\tau}_s^{(\kappa)}\right\} - H_{ijmn}\left\{\widehat{\tau_{ij}}^{(L)} + \widehat{\tau_{ij}}^{(cE)}\right\} \tag{33}$$

or

$$\widehat{u^*_{g,h}} = -E^{-1}_{ghmn}\left[J_{mnp}G_{sp}\left\{\widehat{\tau}_s^{(c\varepsilon)} - \widehat{\tau}_s^{(\kappa)}\right\} + H_{ijmn}\left\{\widehat{\tau_{ij}}^{(L)} + \widehat{\tau_{ij}}^{(cE)}\right\}\right] \tag{34}$$

where, $E_{mnkl} = [I_{mnkl} + J_{mnp}J_{pkl}]$
Similarly we can substitute 22 in 24 and get,

$$\widehat{\phi^*_{,k}} = J_{kmn}\left[-J_{mnp}\widehat{\phi^*_{,p}} - H_{ijmn}\widehat{\tau_{ij}}^{(L)} - H_{ijmn}\widehat{\tau_{ij}}^{(cE)}\right] + G_{ik}\widehat{\tau}_i^{(c\varepsilon)} - G_{ik}\widehat{\tau}_i^{(\kappa)} \tag{35}$$

$$\left[I_{kp} + J_{kmn}J_{mnp}\right]\widehat{\phi^*_{,p}} = -J_{kmn}H_{ijmn}\left\{\widehat{\tau_{ij}}^{(L)} + \widehat{\tau_{ij}}^{(cE)}\right\} + G_{ik}\left\{\widehat{\tau}_i^{(c\varepsilon)} - \widehat{\tau}_i^{(\kappa)}\right\} \tag{36}$$

or

$$\widehat{\phi^*_{,f}} = F^{-1}_{fk}\left[-J_{kmn}H_{ijmn}\left\{\widehat{\tau_{ij}}^{(L)} + \widehat{\tau_{ij}}^{(cE)}\right\} + G_{ik}\left\{\widehat{\tau}_i^{(c\varepsilon)} - \widehat{\tau}_i^{(\kappa)}\right\}\right] \tag{37}$$

where, $F_{pg} = [I_{pg} + J_{pkl}J_{klg}]$. The polarizations can be simplified and re-written as:

$$\widehat{\tau}_g^{(D)} = \widehat{\tau}_g^{(c\varepsilon)} - \widehat{\tau}_g^{(\kappa)}, \quad \widehat{\tau_{ij}}^{(\sigma)} = \widehat{\tau_{ij}}^{(L)} + \widehat{\tau_{ij}}^{(cE)}. \tag{38}$$

Applying an inverse Fourier transform to 34

$$u^*_{g,h} = \sum_{\boldsymbol{\xi}\in\mathcal{R}^*-\{0\}} -E^{-1}_{ghmn}\left[J_{mnp}G_{sp}\widehat{\tau_s}^{(D)} + H_{ijmn}\widehat{\tau_{ij}}^{(\sigma)}\right]e^{\mathrm{i}\boldsymbol{\xi}\cdot\mathbf{x}} \quad (39)$$

The polarizations can accordingly be converted to real space by using the formulae:

$$\widehat{\tau_{ij}}^{(\sigma)} = \left\langle \tau^{(\sigma)}_{ij} e^{-\mathrm{i}\boldsymbol{\xi}\cdot\mathbf{x}} \right\rangle \quad (40)$$

$$\widehat{\tau}^{(D)}_{j} = \left\langle \tau^{(D)}_{j} e^{-\mathrm{i}\boldsymbol{\xi}\cdot\mathbf{x}} \right\rangle \quad (41)$$

The equation for the periodic strain in real space is then given by:

$$\sum_{\boldsymbol{\xi}\in\mathcal{R}^*-\{0\}} -E^{-1}_{ghmn}\left[J_{mnp}G_{sp}\left\langle \tau^{(D)}_{s} e^{-\mathrm{i}\boldsymbol{\xi}\cdot\mathbf{x}} \right\rangle + H_{ijmn}\left\langle \tau^{(\sigma)}_{ij} e^{-\mathrm{i}\boldsymbol{\xi}\cdot\mathbf{x}} \right\rangle\right]e^{\mathrm{i}\boldsymbol{\xi}\cdot\mathbf{x}} \quad (42)$$

Similarly using an inverse Fourier transform to 37 using the relations 40,41

$$\phi^*_{,f} = \sum_{\boldsymbol{\xi}\in\mathcal{R}^*-\{0\}} F^{-1}_{fk}\left[-J_{kmn}H_{ijmn}\left\langle \tau^{(\sigma)}_{ij} e^{-\mathrm{i}\boldsymbol{\xi}\cdot\mathbf{x}} \right\rangle + G_{ik}\left\langle \tau^{(D)}_{i} e^{-\mathrm{i}\boldsymbol{\xi}\cdot\mathbf{x}} \right\rangle\right]e^{-\mathrm{i}\boldsymbol{\xi}\cdot\mathbf{x}} \quad (43)$$

The equations for the periodic strain and electric field [41 and 43] are exact. To solve for the strain and electric field in the inclusion an approximation has to be made regarding the polarization fields. The approximation of using piece-wise constant polarization fields is discussed in the following section.

3.2 Piece-wise constant fields

For a polarization field (τ_{ij}) that is assumed to be piece-wise constant the following relation is implied,

$$\widehat{\tau_{ij}} = \langle \tau_{ij} e^{\mathrm{i}\boldsymbol{\xi}\cdot\mathbf{x}} \rangle$$

$$\text{where} \qquad \tau_{ij}(x) = \sum_{r=1}^{n} \chi^{(r)}\overline{\tau}^{(r)}_{ij} \quad (44)$$

Applying the above relation (43) to the polarization fields used in the current problem the following relation is derived,

$$\tau_{ij}^{(L)}(x) = \left[L_{ijkl}(x) - L_{ijkl}^{(0)}\right] \varepsilon_{kl} \tag{45}$$

$$\left\langle \tau_{ij}^{(L)}(x) \right\rangle^{(r)} = \left[L_{ijkl}^{(r)}(x) - L_{ijkl}^{(0)}(x)\right] \langle \varepsilon_{kl} \rangle^{(r)} \tag{46}$$

$$\overline{\tau_{ij}}^{(L)(r)} = \left[L_{ijkl}^{(r)}(x) - L_{ijkl}^{(0)}(x)\right] \overline{\varepsilon}_{mn}^{(r)} \tag{47}$$

Similarly for the other trial polarization fields we can make the piece-wise constant assumption. The assumptions are based on the fact that we require to obtain sharper bounds than Voigt and Reuss type bounds (which we realise is a case of choosing the polarizations to be constant throughout).

$$\overline{\tau_{ij}}^{(cE)(r)}(x) = \left[e_{kij}(x) - e_{kij}^{(0)}(x)\right] \overline{\phi}_{,k}^{(r)} \tag{48}$$

$$\overline{\tau_{ij}}^{(c\varepsilon)(r)}(x) = \left[e_{imn}(x) - e_{imn}^{(0)}(x)\right] \overline{\varepsilon}_{mn}^{(r)} \tag{49}$$

$$\overline{\tau_{i}}^{(\kappa)(r)}(x) = \left[\kappa_{ik}(x) - \kappa_{ik}^{(0)}(x)\right] \overline{\phi}_{,k}^{(r)} \tag{50}$$

Similarly assuming piece-wise constant fields for 40 and 41

$$\overline{\tau_{ij}}^{(\sigma)(r)} = \left[L_{ijkl}^{(r)}(x) - L_{ijkl}^{(0)}\right] \overline{\varepsilon_{kl}}^{(r)} + \left[e_{kij}^{(r)}(x) - e_{kij}^{(0)}(x)\right] \overline{\phi}_{,k}^{(r)} \tag{51}$$

$$\overline{\tau_{ij}}^{(\sigma)(r)} = \Delta L_{ijkl}^{(r)} \overline{\varepsilon_{kl}}^{(r)} + \Delta e_{kij}^{(r)} \overline{\phi}_{,k}^{(r)} \tag{52}$$

$$\overline{\tau_{i}}^{(D)(r)} = \Delta e_{imn}^{(r)} \overline{\varepsilon_{mn}}^{(r)} - \Delta \kappa_{ik}^{(r)} \overline{\phi}_{,k}^{(r)} \tag{53}$$

Applying the assumption of piece-wise constant fields to 43

$$\begin{aligned} u_{g,h}^{*} = \sum_{\boldsymbol{\xi} \in \mathcal{R}^{*} - \{0\}} -E_{ghmn}^{-1} \Bigg[& J_{mnp} G_{sp} \sum_{r=1}^{p} c^{(r)} \left\{ \Delta e_{srt}^{(r)} \overline{\varepsilon_{rt}}^{(r)} - \Delta \kappa_{so}^{(r)} \overline{\phi}_{,o}^{(r)} \right\} \left\langle e^{-\mathrm{i}\boldsymbol{\xi}\cdot\mathbf{x}} \right\rangle^{(r)} \\ & + H_{ijmn} \sum_{r=1}^{p} c^{(r)} \left\{ \Delta L_{ijxy}^{(r)} \overline{\varepsilon_{xy}}^{(r)} + \Delta e_{aij}^{(r)} \overline{\phi}_{,a}^{(r)} \right\} \left\langle e^{-\mathrm{i}\boldsymbol{\xi}\cdot\mathbf{x}} \right\rangle^{(r)} \Bigg] e^{\mathrm{i}\boldsymbol{\xi}\cdot\mathbf{x}} \end{aligned} \tag{54}$$

Taking the average over the phase s

$$\overline{u^*}^{(s)}_{g,h} = \sum_{\boldsymbol{\xi}\in\mathcal{R}^*-\{0\}} -E^{-1}_{ghmn}\Bigg[J_{mnp}G_{sp}\sum_{r=1}^{p}c^{(r)}\left\{\Delta e^{(r)}_{srt}\overline{\varepsilon_{rt}}^{(r)} - \Delta\kappa^{(r)}_{so}\overline{\phi}^{(r)}_{,o}\right\}\left\langle e^{-\mathrm{i}\boldsymbol{\xi}\cdot\mathbf{x}}\right\rangle^{(r)} + H_{ijmn}\sum_{r=1}^{p}c^{(r)}\left\{\Delta L^{(r)}_{ijxy}\overline{\varepsilon_{xy}}^{(r)} + \Delta e^{(r)}_{aij}\overline{\phi}^{(r)}_{,a}\right\}\left\langle e^{-\mathrm{i}\boldsymbol{\xi}\cdot\mathbf{x}}\right\rangle^{(r)}\Bigg]\left\langle e^{\mathrm{i}\boldsymbol{\xi}\cdot\mathbf{x}}\right\rangle^{(s)} \quad (55)$$

Further simplifying the above equation, the expressions can be solved for periodic strain and electric field after summing over the constituent phases and recognizing the following microstructural tensors, $P^{(rs)}_{ghij}$ and $V^{(rs)}_{ghs}$ given by,

$$P^{(rs)}_{ghij} = \sum_{\boldsymbol{\xi}\in\mathcal{R}^*-\{0\}} E^{-1}_{ghmn}H_{ijmn}\left\langle e^{-\mathrm{i}\boldsymbol{\xi}\cdot\mathbf{x}}\right\rangle^{(r)}\left\langle e^{\mathrm{i}\boldsymbol{\xi}\cdot\mathbf{x}}\right\rangle^{(s)} \quad (56)$$

and

$$V^{(rs)}_{rsp} = \sum_{\boldsymbol{\xi}\in\mathcal{R}^*-\{0\}} E^{-1}_{rsmn}J_{mnp}G_{ip}\left\langle e^{-\mathrm{i}\boldsymbol{\xi}\cdot\mathbf{x}}\right\rangle^{(r)}\left\langle e^{\mathrm{i}\boldsymbol{\xi}\cdot\mathbf{x}}\right\rangle^{(s)} \quad (57)$$

Symmetrising $\boldsymbol{P}$, such that

$$P^{(rs)}_{ghij} = \frac{1}{4}\left[P^{(rs)}_{ghij} + P^{(rs)}_{ghji} + P^{(rs)}_{hgij} + P^{(rs)}_{ijgh}\right] \quad (58)$$

we get the expression for the periodic strain as,

$$\overline{\varepsilon^*_{gh}}^{(s)} = -\sum_{r=1}^{p}c^{(r)}P^{(rs)}_{ghij}\left[\Delta L^{(r)}_{ijxy}\overline{\varepsilon_{xy}}^{(r)} + \Delta e^{(r)}_{aij}\overline{\phi}^{(r)}_{,a}\right] - \quad (59)$$

$$\sum_{r=1}^{p}c^{(r)}V^{(rs)}_{ghs}\left[\Delta e^{(r)}_{srt}\overline{\varepsilon_{rt}}^{(r)} - \Delta\kappa^{(r)}_{so}\overline{\phi}^{(r)}_{,o}\right] \quad (60)$$

The equivalent equation of 60 for the electric field is given as:

$$\overline{\phi^*}_{,f}^{(s)} = -\sum_{r=1}^{p} c^{(r)} V_{fij}^{(rs)} \left[\Delta L_{ijcd}^{(r)} \overline{\varepsilon_{cd}}^{(r)} + \Delta e_{tij}^{(r)} \overline{\phi}_{,t}^{(r)} \right] + \sum_{r=1}^{p} c^{(r)} T_{fs}^{(rs)} \left[\Delta e_{scd}^{(r)} \overline{\varepsilon_{cd}}^{(r)} - \Delta \kappa_{sc}^{(r)} \overline{\phi}_{,c}^{(r)} \right] \tag{61}$$

where the microstructural tensor $T_{fs}^{(rs)}$ is given by:

$$T_{gi}^{(rs)} = \sum_{\boldsymbol{\xi} \in \mathcal{R}^* - \{0\}} F_{gp}^{-1} G_{ip} \left\langle e^{-\mathrm{i}\boldsymbol{\xi}\cdot\mathbf{x}} \right\rangle^{(r)} \left\langle e^{\mathrm{i}\boldsymbol{\xi}\cdot\mathbf{x}} \right\rangle^{(s)} \tag{62}$$

Note:- The equivalent form of the third order microstructural tensor is used in the equation 61 which is given by,

$$V_{grs}^{(rs)} = \sum_{\boldsymbol{\xi} \in \mathcal{R}^* - \{0\}} F_{gp}^{-1} J_{pkl} H_{rskl} \left\langle e^{-\mathrm{i}\boldsymbol{\xi}\cdot\mathbf{x}} \right\rangle^{(r)} \left\langle e^{\mathrm{i}\boldsymbol{\xi}\cdot\mathbf{x}} \right\rangle^{(s)} \tag{63}$$

Solving equations 60 and 61 to derive the expressions for the average strain and electric field in the particle $\overline{\varepsilon_{mn}}^{(2)}$ and $\overline{\phi_{,n}}^{(2)}$. The key idea in solving the equations for strain and electric field is making the polarization fields in the matrix zero. This is achieved by choosing a reference medium with the material parameters of the matrix.

3.3 Solving for strain and electric field

Choosing $\boldsymbol{L^{(0)}}$, $\boldsymbol{e^{(0)}}$, $\boldsymbol{\kappa^{(0)}} = \boldsymbol{L^{(1)}}$, $\boldsymbol{e^{(1)}}$, $\boldsymbol{\kappa^{(1)}}$ and substituting the relations 60 and 61 into $\overline{\varepsilon_{gh}}^{(s)} = \overline{\varepsilon_{gh}} + \overline{\varepsilon_{gh}^*}^{(s)}$ and $\overline{\phi_{,g}}^{(s)} = \overline{\phi_{,g}} + \overline{\phi_{,g}^*}^{(s)}$. The equation for strain and electric field for a two phase composite are derived as follows;

$$\overline{\varepsilon_{xy}}^{(2)} = \alpha_{pqgh}^{-1} \left[\overline{\varepsilon_{gh}} - \beta_{gha} \overline{\phi_{,a}}^{(2)} \right] \tag{64}$$

where, $\alpha_{ghxy} = \left[I_{ghxy} + c^{(2)} \left\{ P_{ghij}^{(22)} \Delta L_{ijxy}^{(2)} + V_{ghs}^{(22)} \Delta e_{sxy}^{(2)} \right\} \right]$ and
$\beta_{gha} = c^{(2)} \left\{ P_{ghij}^{(22)} \Delta e_{aij}^{(2)} - V_{ghs}^{(22)} \Delta \kappa_{sa}^{(2)} \right\}$.

Similarly by solving for the electric field

$$\overline{\phi_{,q}}^{(2)} = \gamma_{qf}^{-1}\left[\overline{\phi_{,f}} + \rho_{fcd}\overline{\varepsilon_{cd}}^{(2)}\right] \tag{65}$$

where, $\gamma_{ft} = \left[I_{ft} + c^{(2)}\left\{V_{fij}^{(22)}\Delta e_{tij}^{(2)} + T_{fs}^{(22)}\Delta\kappa_{st}^{(2)}\right\}\right]$ and
$\rho_{fcd} = c^{(2)}\left\{-V_{fij}^{(22)}\Delta L_{ijcd}^{(2)} + T_{fs}^{(22)}\Delta e_{scd}^{(2)}\right\}$. Substituting 65 in 64 and solving for the strain in the inclusion we get,

$$\overline{\varepsilon}_{ij}^{(2)} = W_{ijpq}^{-1}\alpha_{pqgh}^{-1}\left\{\overline{\varepsilon}_{gh} - \beta_{gha}\gamma_{af}^{-1}\overline{\phi}_{,f}\right\} \tag{66}$$

where, $W_{pqcd} = [I_{pqcd} + \alpha_{pqgh}^{-1}\beta_{gha}\gamma_{af}^{-1}\rho_{fcd}]$. Using the results obtained in 66 to find the electric field in the particle, we get,

$$\overline{\phi}_{,r}^{(2)} = U_{ra}^{-1}\gamma_{af}^{-1}\left[\rho_{fcd}W_{cdpq}^{-1}\alpha_{pqgh}^{-1}\overline{\varepsilon}_{gh} + \overline{\phi}_{,f}\right] \tag{67}$$

where, $U_{ak} = \left[I_{ak} + \gamma_{af}^{-1}\rho_{fcd}W_{cdpq}^{-1}\alpha_{pqgh}^{-1}\beta_{ghb}\gamma_{bk}^{-1}\right]$.

CHAPTER 4

Concentration Tensors

Let the concentration tensors be defined such that,

$$\overline{\varepsilon_{ij}}^{(r)} = A^{(r)}_{ijkl}\overline{\varepsilon}_{ij} + a^{(r)}_{ijk}\overline{\phi}_{,k} \tag{68}$$

$$\overline{\phi_{,k}}^{(r)} = B^{(r)}_{kmn}\overline{\varepsilon}_{mn} + b^{(r)}_{km}\overline{\phi}_{,k} \tag{69}$$

For a given homogeneous composite, the constitutive equation for stress is given by:

$$\overline{\sigma}_{ij} = \widetilde{L}_{ijkl}\overline{\varepsilon}_{kl} + \widetilde{e}_{kij}\overline{\phi}_{,k} \tag{70}$$

Writing $\overline{\sigma}_{ij}$ in terms of the phase average stresses $\overline{\sigma}^{(r)}_{ij}$
we get,

$$\overline{\sigma}_{ij} = \sum_{r=1}^{n} c^{(r)}\overline{\sigma}^{(r)}_{ij} \tag{71}$$

Equating 70 and 71

$$\sum_{r=1}^{n} c^{(r)}\overline{\sigma}^{(r)}_{ij} = \widetilde{L}_{ijkl}\overline{\varepsilon}_{kl} + \widetilde{e}_{kij}\overline{\phi}_{,k}$$

$$\sum_{r=1}^{n} c^{(r)}(L^{(r)}_{ijkl}\overline{\varepsilon}^{(r)}_{kl} + e^{(r)}_{kij}\overline{\phi}^{(r)}_{,k}) = \widetilde{L}_{ijkl}\overline{\varepsilon}_{kl} + \widetilde{e}_{kij}\overline{\phi}_{,k} \tag{72}$$

Substituting 68 and 69 in 72

$$\begin{aligned}
\widetilde{L}_{ijkl}\overline{\varepsilon}_{kl} + \widetilde{e}_{kij}\overline{\phi}_{,k} &= \sum_{r=1}^{n} c^{(r)} L^{(r)}_{ijkl}(A^{(r)}_{klmn}\overline{\varepsilon}_{mn} + a^{(r)}_{klm}\overline{\phi}_{,m}) \\
&+ \sum_{r=1}^{n} c^{(r)} e^{(r)}_{kij}(B^{(r)}_{kmn}\overline{\varepsilon}_{mn} + b^{(r)}_{km}\overline{\phi}_{,k}) \qquad (73) \\
&= \sum_{r=1}^{n} c^{(r)} L^{(r)}_{ijkl} A^{(r)}_{klmn}\overline{\varepsilon}_{mn} + \sum_{r=1}^{n} c^{(r)} L^{(r)}_{ijkl} a^{(r)}_{klm}\overline{\phi}_{,m} \\
&+ \sum_{r=1}^{n} c^{(r)} e^{(r)}_{kij} B^{(r)}_{kmn}\overline{\varepsilon}_{mn} + \sum_{r=1}^{n} c^{(r)} e^{(r)}_{kij} b^{(r)}_{km}\overline{\phi}_{,m} \qquad (74) \\
\widetilde{L}_{ijkl}\overline{\varepsilon}_{kl} + \widetilde{e}_{kij}\overline{\phi}_{,k} &= \sum_{r=1}^{n} c^{(r)}(L^{(r)}_{ijkl} A^{(r)}_{klmn} + e^{(r)}_{kij} B^{(r)}_{kmn})\overline{\varepsilon}_{mn} \\
&+ \sum_{r=1}^{n} c^{(r)}(L^{(r)}_{ijkl} a^{(r)}_{klm} + e^{(r)}_{kij} b^{(r)}_{km})\overline{\phi}_{,m}
\end{aligned}$$

Therefore,

$$\widetilde{L}_{ijkl} = \sum_{r=1}^{n} c^{(r)}(L^{(r)}_{ijmn} A^{(r)}_{mnkl} + e^{(r)}_{kij} B^{(r)}_{kmn}) \qquad (75)$$

$$\widetilde{e}_{mij} = \sum_{r=1}^{n} c^{(r)}(L^{(r)}_{ijkl} a^{(r)}_{klm} + e^{(r)}_{kij} b^{(r)}_{km}) \qquad (76)$$

Restrictions

$$\overline{\varepsilon}_{ij} = \sum_{r=1}^{n} c^{(r)} \overline{\varepsilon}^{(r)}_{ij} \qquad (77)$$

$$\text{And} \quad \overline{\varepsilon}^{(r)}_{ij} = A^{(r)}_{ijkl}\overline{\varepsilon}_{kl} + a^{(r)}_{ijk}\overline{\phi}_{,k} \qquad (78)$$

Substituting Equation 78 in 77

$$\begin{aligned}\overline{\varepsilon}_{ij} &= \sum_{r=1}^{n} c^{(r)}(A^{(r)}_{ijkl}\overline{\varepsilon}_{kl} + a^{(r)}_{ijk}\overline{\phi}_{,k}) \\ &= \sum_{r=1}^{n} c^{(r)}A^{(r)}_{ijkl}\overline{\varepsilon}_{kl} + \sum_{r=1}^{n} c^{(r)}a^{(r)}_{ijk}\overline{\phi}_{,k}\end{aligned}$$

Equating terms on either side:-

$$\sum_{r=1}^{n} c^{(r)}A^{(r)}_{ijkl} = I_{ijkl} \;\; ; \;\; \sum_{r=1}^{n} c^{(r)}a^{(r)}_{ijk} = 0 \tag{79}$$

Similarly,

$$\begin{aligned}\overline{\phi}_{,k} &= \sum_{r=1}^{n} c^{(r)}\overline{\phi}^{(r)}_{,k} \\ \overline{\phi}^{(r)}_{,k} &= B^{(r)}_{kmn}\overline{\varepsilon}_{mn} + b^{(r)}_{km}\overline{\phi}_{,m}\end{aligned} \tag{80}$$

Therefore,

$$\sum_{r=1}^{n} c^{(r)}B^{(r)}_{kmn} = 0 \;\; ; \;\; \sum_{r=1}^{n} c^{(r)}b^{(r)}_{km} = I_{km} \tag{81}$$

using 79 and 81

$$\begin{aligned}\sum_{r=1}^{n} c^{(r)}A^{(r)}_{ijkl} &= I_{ijkl} \\ c^{(n)}A^{(n)}_{ijkl} &= I_{ijkl} - \sum_{r=1}^{n-1} c^{(r)}A^{(r)}_{ijkl}\end{aligned}$$

Pre-Multiplying by $\boldsymbol{L^{(n)}}$

$$c^{(n)}L^{(n)}_{ijmn}A^{(n)}_{mnkl} = L^{(n)}_{ijkl} - \sum_{r=1}^{n-1} c^{(r)}L^{(n)}_{ijmn}A^{(r)}_{mnkl} \tag{82}$$

From 81

$$\begin{aligned}\sum_{r=1}^{n} c^{(r)} B^{(r)}_{kmn} &= 0 \\ c^{(n)} B^{(n)}_{kmn} &= -\sum_{r=1}^{n-1} c^{(r)} B^{(r)}_{kmn} \end{aligned} \tag{83}$$

Pre-multiplying with $\boldsymbol{e^{(n)}}$

$$c^{(n)} e^{(n)}_{kij} B^{(n)}_{kmn} = -\sum_{r=1}^{n-1} c^{(r)} e^{(n)}_{kij} B^{(r)}_{kmn} \tag{84}$$

Substituting in the equation for $\widetilde{\boldsymbol{L}}$ in 76

$$\begin{aligned}\widetilde{L}_{ijkl} &= \sum_{r=1}^{n-1} c^{(r)} L^{(r)}_{ijmn} A^{(r)}_{mnkl} + \sum_{r=1}^{n-1} c^{(r)} e^{(r)}_{pij} B^{(r)}_{pkl} + L^{(n)}_{ijkl} \\ &- \sum_{r=1}^{n-1} c^{(r)} L^{(n)}_{ijmn} A^{(r)}_{mnkl} - \sum_{r=1}^{n-1} c^{(r)} e^{(n)}_{pij} B^{(r)}_{pkl} \end{aligned} \tag{85}$$

or,

$$\widetilde{L}_{ijkl} = L^{(n)}_{ijkl} + \sum_{r=1}^{n-1} c^{(r)} (L^{(r)}_{ijmn} - L^{(n)}_{ijmn}) A^{(r)}_{mnkl} + \sum_{r=1}^{n-1} c^{(r)} (e^{(r)}_{pij} - e^{(n)}_{pij}) B^{(r)}_{pkl} \tag{86}$$

Also,

$$\begin{aligned}\sum_{r=1}^{n} c^{(r)} a^{(r)}_{klm} &= 0 \\ c^{(n)} a^{(n)}_{klm} &= -\sum_{r=1}^{n-1} c^{(r)} a^{(r)}_{klm} \end{aligned} \tag{87}$$

And,

$$\begin{aligned}\sum_{r=1}^{n} c^{(r)} b_{km}^{(r)} &= I_{km} \\ c^{(n)} b_{km}^{(n)} &= I_{km} - \sum_{r=1}^{n-1} c^{(r)} b_{km}^{(r)} \end{aligned} \tag{88}$$

Pre-Multiplying Equation 87 and 88 by $\boldsymbol{L^{(n)}}$ and $\boldsymbol{e^{(n)}}$ repectively

$$c^{(n)} L_{ijkl}^{(n)} a_{klm}^{(n)} = -\sum_{r=1}^{n-1} c^{(r)} L_{ijkl}^{(n)} a_{klm}^{(r)} \tag{89}$$

$$c^{(n)} e_{kij}^{(n)} b_{km}^{(n)} = e_{kij}^{(n)} I_{km} - \sum_{r=1}^{n-1} c^{(r)} e_{kij}^{(n)} b_{km}^{(r)} \tag{90}$$

Substituting in the equation for $\widetilde{\boldsymbol{e}}$ in 76

$$\begin{aligned}\widetilde{e}_{mij} &= \sum_{r=1}^{n-1} c^{(r)} L_{ijkl}^{(r)} a_{klm}^{(r)} - \sum_{r=1}^{n-1} c^{(r)} L_{ijkl}^{(n)} a_{klm}^{(r)} \\ &+ \sum_{r=1}^{n-1} c^{(r)} e_{kij}^{(r)} b_{km}^{(r)} + e_{kij}^{(n)} I_{km} - \sum_{r=1}^{n-1} c^{(r)} e_{kij}^{(n)} b_{km}^{(r)} \end{aligned} \tag{91}$$

$$\widetilde{e}_{mij} = e_{ijm}^{(n)} + \sum_{r=1}^{n-1} c^{(r)} (L_{ijkl}^{(r)} - L_{ijkl}^{(n)}) a_{klm}^{(r)} + \sum_{r=1}^{n-1} c^{(r)} (e_{kij}^{(r)} - e_{kij}^{(n)}) b_{km}^{(r)} \tag{92}$$

Similarly,

$$\overline{D}_i = \widetilde{e}_{ikl} \overline{\varepsilon}_{kl} - \widetilde{\kappa}_{ik} \overline{\phi}_{,k} \tag{93}$$

can be written as:

$$\overline{D}_i = \sum_{r=1}^{n} c^{(r)} \overline{D}_i^{(r)} \tag{94}$$

or,

$$\widetilde{e}_{imn} \overline{\varepsilon}_{mn} - \widetilde{\kappa}_{in} \overline{\phi}_{,n} = \sum_{r=1}^{n} c^{(r)} [e_{ikl}^{(r)} \overline{\varepsilon}_{kl}^{(r)} - \kappa_{ik}^{(r)} \overline{\phi}_{,k}^{(r)}] \tag{95}$$

Substituting $\overline{\varepsilon}_{kl}^{(r)}$ and $\overline{\phi}_{,k}^{(r)}$ from 68 and 69

$$\begin{aligned}\widetilde{e}_{imn}\overline{\varepsilon}_{mn} - \widetilde{\kappa}_{in}\overline{\phi}_{,n} &= \sum_{r=1}^{n} c^{(r)}[e_{ikl}^{(r)}A_{klmn}^{(r)} - \kappa_{ik}^{(r)}B_{kmn}^{(r)}]\overline{\varepsilon}_{mn} \\ &+ \sum_{r=1}^{n} c^{(r)}[e_{ikl}^{(r)}a_{kln}^{(r)} - \kappa_{ik}^{(r)}b_{kn}^{(r)}]\overline{\phi}_{,n}\end{aligned} \tag{96}$$

on comparing,

$$\begin{aligned}\widetilde{e}_{imn} &= \sum_{r=1}^{n} c^{(r)}[e_{ikl}^{(r)}A_{klmn}^{(r)} - \kappa_{ik}^{(r)}B_{kmn}^{(r)}] \\ -\widetilde{\kappa}_{in} &= \sum_{r=1}^{n} c^{(r)}[e_{ikl}^{(r)}a_{kln}^{(r)} - \kappa_{ik}^{(r)}b_{kn}^{(r)}]\end{aligned} \tag{97}$$

Using the relations 79 and 79

$$\begin{aligned}\sum_{r=1}^{n} c^{(r)}a_{kln}^{(r)} &= 0 \\ c^{(n)}a_{kln}^{(n)} &= -\sum_{r=1}^{n-1} c^{(r)}a_{kln}^{(r)}\end{aligned}$$

Pre-multiplying with $\boldsymbol{e^{(n)}}$

$$c^{(n)}e_{ikl}^{(n)}a_{kln}^{(n)} = -\sum_{r=1}^{n-1} c^{(r)}e_{ikl}^{(n)}a_{kln}^{(r)} \tag{98}$$

Similarly,

$$\begin{aligned}\sum_{r=1}^{n} c^{(r)}b_{kn}^{(r)} &= I_{kn} \\ c^{(n)}b_{kn}^{(n)} &= I_{kn} - \sum_{r=1}^{n-1} c^{(r)}b_{kn}^{(r)}\end{aligned}$$

Pre-multiplying with $\boldsymbol{\kappa^{(n)}}$

$$c^{(n)}\kappa_{ik}^{(n)}b_{kn}^{(n)} = \kappa_{in}^{(n)} - \sum_{r=1}^{n-1} c^{(r)}\kappa_{ik}^{(n)}b_{kn}^{(r)} \tag{99}$$

Substituting Equations 98 and 99 in 97

$$\begin{aligned} -\widetilde{\kappa}_{in} &= \sum_{r=1}^{n-1} c^{(r)}e_{ikl}^{(r)}a_{kln}^{(r)} - \sum_{r=1}^{n-1} c^{(r)}e_{ikl}^{(n)}a_{kln}^{(r)} - \kappa_{in}^{(r)} + \sum_{r=1}^{n-1} c^{(r)}\kappa_{ik}^{(n)}b_{kn}^{(r)} \\ &- \sum_{r=1}^{n-1} c^{(r)}\kappa_{ik}^{(r)}b_{kn}^{(r)} \end{aligned} \tag{100}$$

$$-\widetilde{\kappa}_{in} = \sum_{r=1}^{n-1} c^{(r)}(e_{ikl}^{(r)} - e_{ikl}^{(n)})a_{kln}^{(r)} + \sum_{r=1}^{n-1} c^{(r)}(\kappa_{ik}^{(n)} - \kappa_{ik}^{(r)})b_{kn}^{(r)} - \kappa_{in}^{(r)} \tag{101}$$

or,

$$\widetilde{\kappa}_{in} = \kappa_{in}^{(r)} + \sum_{r=1}^{n-1} c^{(r)}(\kappa_{ik}^{(r)} - \kappa_{ik}^{(n)})b_{kn}^{(r)} - \sum_{r=1}^{n-1} c^{(r)}(e_{ikl}^{(r)} - e_{ikl}^{(n)})a_{kln}^{(r)} \tag{102}$$

Also,

$$\widetilde{e}_{imn} = \sum_{r=1}^{n=1} c^{(r)}[e_{ikl}^{(r)}A_{klmn}^{(r)} - \kappa_{ik}^{(r)}B_{kmn}^{(r)}] \tag{103}$$

using the relations:

$$\sum_{r=1}^{n} c^{(r)}A_{ijkl}^{(r)} = I_{ijkl}$$

$$c^{(n)}A_{ijkl}^{(n)} = I_{ijkl} - \sum_{r=1}^{n-1} c^{(r)}A_{ijkl}^{(r)} \tag{104}$$

Pre-multiplying with $\boldsymbol{e^{(n)}}$

$$c^{(n)}e_{ikl}^{(n)}A_{klmn}^{(n)} = e_{ikl}^{(n)}I_{klmn} - \sum_{r=1}^{n-1} c^{(r)}e_{ikl}^{(n)}A_{klmn}^{(r)} \tag{105}$$

also,

$$\begin{aligned}\sum_{r=1}^{n} c^{(r)} B^{(r)}_{kmn} &= 0 \\ c^{(n)} B^{(n)}_{kmn} &= -\sum_{r=1}^{n-1} c^{(r)} B^{(r)}_{kmn} \end{aligned} \tag{106}$$

Pre-multiplying with $\boldsymbol{\kappa^{(n)}}$

$$\tag{107}$$

$$c^{(n)} \kappa^{(n)}_{ik} B^{(n)}_{kmn} = -\sum_{r=1}^{n-1} c^{(r)} \kappa^{(n)}_{ik} B^{(r)}_{kmn} \tag{108}$$

Substituting 104 and 108

$$\begin{aligned}\widetilde{e}_{imn} &= \sum_{r=1}^{n-1} c^{(r)} e^{(r)}_{ikl} A^{(r)}_{klmn} + e^{(n)}_{ikl} I_{klmn} - \sum_{r=1}^{n-1} c^{(r)} e^{(n)}_{ikl} A^{(r)}_{klmn} - \sum_{r=1}^{n-1} c^{(r)} \kappa^{(r)}_{ik} B^{(r)}_{kmn} \\ &+ \sum_{r=1}^{n-1} c^{(r)} \kappa^{(n)}_{ik} B^{(r)}_{kmn} \end{aligned} \tag{109}$$

$$\widetilde{e}_{imn} = e^{(n)}_{imn} + \sum_{r=1}^{n-1} c^{(r)} (e^{(r)}_{ikl} - e^{(n)}_{ikl}) A^{(r)}_{klmn} - \sum_{r=1}^{n-1} c^{(r)} (\kappa^{(r)}_{ik} - \kappa^{(n)}_{ik}) B^{(r)}_{kmn} \tag{110}$$

The concentration tensors derived in the above case are:

$$A^{(2)}_{ijkl} = W^{-1}_{ijmn} \alpha^{-1}_{mnkl} \tag{111}$$

$$a^{(2)}_{ijk} = -W^{-1}_{ijmn} \alpha^{-1}_{mngh} \beta_{gha} \gamma^{-1}_{ak} \tag{112}$$

$$B^{(2)}_{kmn} = U^{-1}_{ka} \gamma^{-1}_{af} \rho_{fcd} W^{-1}_{cdpq} \alpha^{-1}_{pqmn} \tag{113}$$

$$b^{(2)}_{km} = U^{-1}_{ka} \gamma^{-1}_{am} \tag{114}$$

Part II of the thesis will look in detail at the finite-element techniques used to compare the results of the analytic model.

Part II

Finite-element simulations of piezoelectric composites

CHAPTER 5

Classification of Piezoelectric Composites

In general, for a piezoelectric composite material there are many ways in which one can classify their geometry based on the connectivity of its individual constituents. Pioneering work was first done by Newnham [32] in which 10 distinct ways of creating a system based on the connectivity of each phase were presented, where connectivity is defined as the number of dimensions in which one constituent is connected to itself in an infinitely repeating composite assemblage. Furthermore piezoelectric composites can be classified in three distinct types: (i) 3-0 type, where the porosity is enclosed in all three dimensions by the continuous matrix phase; (ii) 3-3 type, where the porosity exists in an open inter-connecting network like configuration with both matrix and porosity exhibiting connectivity in all three directions; (iii) 3-1 type, where the porosity exhibits connectivity in the 1-direction (similar to the case of long fibers) embedded in the continuous matrix phase which is connected to itself in all three directions.

Results for the 3-1 type long cylindrical pore, 3-0 cylindrical pore, 3-0 spherical pore and 3-0 flat cuboidal pore have been presented in this study. In all simulations, the axis of poling is aligned with the 3-direction. An overview of the constitutive relations that govern the behaviour of piezoelectric materials

in the linear elastic domain is given in Section 6.

CHAPTER 6

Constitutive Relations for Piezoelectric Materials

The constitutive relations that govern the behaviour of piezoelectric materials in the linear elastic domain as represented (in stress-charge) form as follows:

$$\begin{aligned} \sigma_{ij} &= L^{E}_{ijkl}\varepsilon_{kl} - e_{kij}E_k \\ D_i &= e_{imn}\varepsilon_{mn} + \kappa^{\varepsilon}_{in}E_n \end{aligned} \tag{115}$$

where σ is the stress tensor, e is the strain tensor, E is the electric field vector, D is the electric displacement vector, L^E is the stiffness tensor with the superscript E indicating that the measurement of the components have been carried out at zero/constant electric field, κ^{ε} is the permittivity tensor with the superscript ε indicating that the components of κ have been measured at constant or zero strain, e is the piezoelectric coupling tensor.

Following the representation of Nye [33], Eqn. 115 can also be written as:

$$\begin{aligned} \sigma_a &= L^{E}_{ab}\varepsilon_b - e_{ab}E_b \\ D_a &= e_{ab}\varepsilon_b + \kappa^{\varepsilon}_{ab}E_b \end{aligned} \tag{116}$$

where a and b are derived from ij and kl as: for ij or $kl = 11, 22, 33, 23, 13, 12$ and a and b correspond to $1, 2, 3, 4, 5, 6$ respectively. Eqn. 115 is the most general representation of the constitutive behaviour of the piezoelectric phenomenon with 45 independent constants, 21 elastic, and 18 piezoelectric and 6 dielectric (or permittivity) constants. For the complete characterization of the piezoelectric behaviour of a material all 45 material constants have to be determined.

The three-dimensional finite element-based numerical model developed in the present study is used to determine all the electromechanical constants for 1-3 type long cylindrical pores, 0-3 type cylindrical pores, 0-3 type spherical pored and 0-3 type flat cuboidal pores.

To assess the utility of piezoelectric composites in practical applications, combinations of the fundamental electromechanical properties (i.e. figures of merit) are usually invoked. Some figures of merit are of direct importance to porous piezoelectric materials and their possible applications (e.g. in hydrophones) and are highlighted in the following section.

CHAPTER 7

Figures of Merit

The four figures of merit identified for the present study are: the piezoelectric coupling constant (k_t), the acoustic impedance (Z), the piezoelectric charge coefficient (d_h), and the hydrostatic figure of merit ($d_h g_h$). These figures of merit provide information with regards to the practical utility of piezoelectric composites. A brief description of each individual figure of merit, invoked in the present study, is given below.

7.1 Piezoelectric Coupling Constant

The piezoelectric coupling constant, $k_t = \sqrt{1 - \frac{L_{33}^E}{L_{33}^D}}$ describes the efficiency of the conversion between electrical and mechanical energy by the piezoelectric material. The ratio of the stored converted energy of one kind (mechanical or electrical) to the input energy of the second kind (electrical or mechanical) is defined as the square of the coupling coefficient. Materials with larger coupling constants (~ 1) are more desired.

7.2 Acoustic Impedance

The acoustic impedance given by, $Z = \sqrt{L_{33}^E \rho}$, represents the overall acoustic load at the interface between the hydrophone/device and the environment,

where ρ is the effective density of the material. Good impedance matching between the device and the surrounding media is essential to enhance the performance of the hydrophone. Since porous piezoelectric materials have lower densities than pore-free materials they targeted for use in hydrophone applications. The effective density is calculated using the formula, $\rho = c^{(1)}\rho_1 + c^{(2)}\rho_2$, where $c^{(1)}$, $c^{(2)}$ are the volume fractions of the two phases and ρ_1, ρ_2 are the respective densities.

7.3 Hydrostatic Strain Coefficient

The hydrostatic (or piezoelectric) strain coefficient,$d_h = d_{31} + d_{32} + d_{33}$, is the measure of the effective strength of electromechanical coupling in a piezoelectric material. Is it especially important in the conversion of mechanical loads (under hydrostatic loading) to electrical signals (in a given direction, 3). It describes the polarization that results from a change in hydrostatic stress. To enhance the sensitivity of the hydrophone to the detection of sound, a large value for the piezoelectric charge coefficient is desired. The piezoelectric strain coefficient ($\boldsymbol{d}$) can be evaluated from the piezoelectric stress coefficient ($\boldsymbol{e}$) as,

$$d_{ijk} = e_{imn} S^E_{mnjk} \tag{117}$$

where, S^E_{mnjk} is the elastic compliance tensor.

7.4 Hydrostatic Figure of Merit

The hydrostatic figure of merit, $d_h g_h$ defines the hydrophones sensing and actuating capability. The sensitivity of a hydrophone depends primarily on the voltage that is produced by a hydrostatic pressure wave. The hydrostatic voltage coefficient, g_h, relates the electric field across a transducer to the applied hydrostatic stress, and is therefore an important parameter for evaluating piezoelectric materials for use in hydrophones. The g_h coefficient is related to

the d_h coefficient by the permittivity constant (κ) as, $g_h = \frac{d_h}{\kappa}$. Porous piezoelectric materials usually show higher values for the hydrostatic figure of merit than purely piezoelectric or piezo-ceramic composites.

The important aspects of the analytic model used to compare the three-dimensional finite element model are given in the following section.

CHAPTER 8

Analytic model

Several analytic models exist that predict the behaviour of piezoelectric composite materials. The first attempt to solve the problem of a piezoelectric inclusion distributed uniformly within a homogeneous matrix phase in an infinite array was made by Banno [2]. His approach used the concept of the Banno unit cell, a representative volume element which when added contiguously in three dimensions produces the periodic composite. The model given by Banno uses a generalization of series parallel connections to characterize the complete electromechanical response of piezoelectric composites. The model given by Banno was developed further by Hashimoto and Yamaguchi [15]. They presented a matrix method that could help study the electromechanical response of piezoelectric composite materials regardless of the material symmetry of its constituent phases. The model presented in their paper gives accurate results for one-dimensional (2-2 laminate type) and two-dimensional (1-3 long fiber type) piezoelectric composite materials. The matrix method presented by Hashimoto and Yamaguchi was applied to 0-3 type and 3-3 type piezoelectric composites by Levassort et al. [25, 27, 26]. The present study uses this analytic scheme to compare the results obtained by the three-dimensional finite element model. The key aspects involved in the framework of the matrix method used in [15] are presented below.

The piezoelectric constitutive relations (in the contracted matrix notation) in the constituent phases are given by:

$$\begin{pmatrix} T \\ D \end{pmatrix} = \begin{pmatrix} C & -e^t \\ e & \varepsilon^S \end{pmatrix} \begin{pmatrix} S \\ E \end{pmatrix} = [K] \begin{pmatrix} S \\ E \end{pmatrix} \tag{118}$$

where T is the stress vector which includes all the stress components, $T = (T_1, T_2, T_3, T_4, T_5, T_6)$. Similarly S is the strain vector containing all 6 strain components, E is the electric field vector and D is the electric displacement vector. C^E,e,ε^S are the elastic (at constant electric field), piezoelectric, and dielectric(at constant strain) tensors. Writing the equations for each of the two constituent phases separately in a further contracted form gives:

$$(TD)^c = [K]^c (SE)^c \tag{119}$$

$$(TD)^p = [K]^p (SE)^p \tag{120}$$

$$\left(\overline{TD}\right)^c = [\overline{K}]^c \left(\overline{SE}\right)^c \tag{121}$$

where, $[K]^c$, $[K]^p$ are the effective electromechanical matrices for the ceramic and polymer phase respectively and $[\overline{K}]^p$ is the effective electromechanical matrix for the composite.
By defining two new vectors, (G) and (H) and transforming the (TD) and (SE) vectors

$$(TD) = [Q](H) - [P](G) \tag{122}$$

$$(SE) = [Q](G) - [P](H) \tag{123}$$

where (G) and (H) contain the continuous and averaged T, D, S, E boundary conditions respectively. The diagonal matrices $[P]$ and $[Q]$ are given by: $[Q] - [P] = [Id]$ where $[Id]$ is the ninth-order identity matrix. (TD) can then be written as : $(TD) = [K]\{[Q](G) - [P](H)\}$ and $(H) = [W](G)$ with $[W] = \{[Q] + [K][P]\}^{-1}\{[P] + [K][Q]\}$ and $[K] = \{[P] - [Q][W]\}\{[P][W] - [Q]\}^{-1}$. Writing the equations for the overall composite $[K] = \{[P] - [Q][W]\}\{[P][W] - [Q]\}^{-1}$ where $[\overline{W}] = \nu[W]^c + (1-\nu)[W]^p$, ν being the volume fraction of the

ceramic phase.

The three-dimensional finite element model used to study the four geometries of porous piezoelectric composites is presented in section 9.

CHAPTER 9

Three-Dimensional Finite Element Model to Study Piezoelectric Composite Materials

The finite element model utilized in the present study uses the basis that the complete electromechanical response of an infinitely large periodic piezoelectric composite material can be understood by characterizing the behaviour of a representative volume element or unit cell. A unit cell can then be repeated in all three axes to generate the infinitely large periodic piezoelectric composite. Since the unit cell captures the response of the entire composite material certain conditions must be enforced to make sure that the deformation and electric potential of a unit cell are compatible across its boundaries with adjacent unit cells. To be able to study the response of a 1-3 type long cylindrical pore, 0-3 type spherical pore, 0-3 cylindrical pore and 0-3 type flat cuboidal pore, four types of three-dimensional unit cells were constructed. A schematic diagram of the unit cells showing square and cubic distribution of pored is given in Fig.4

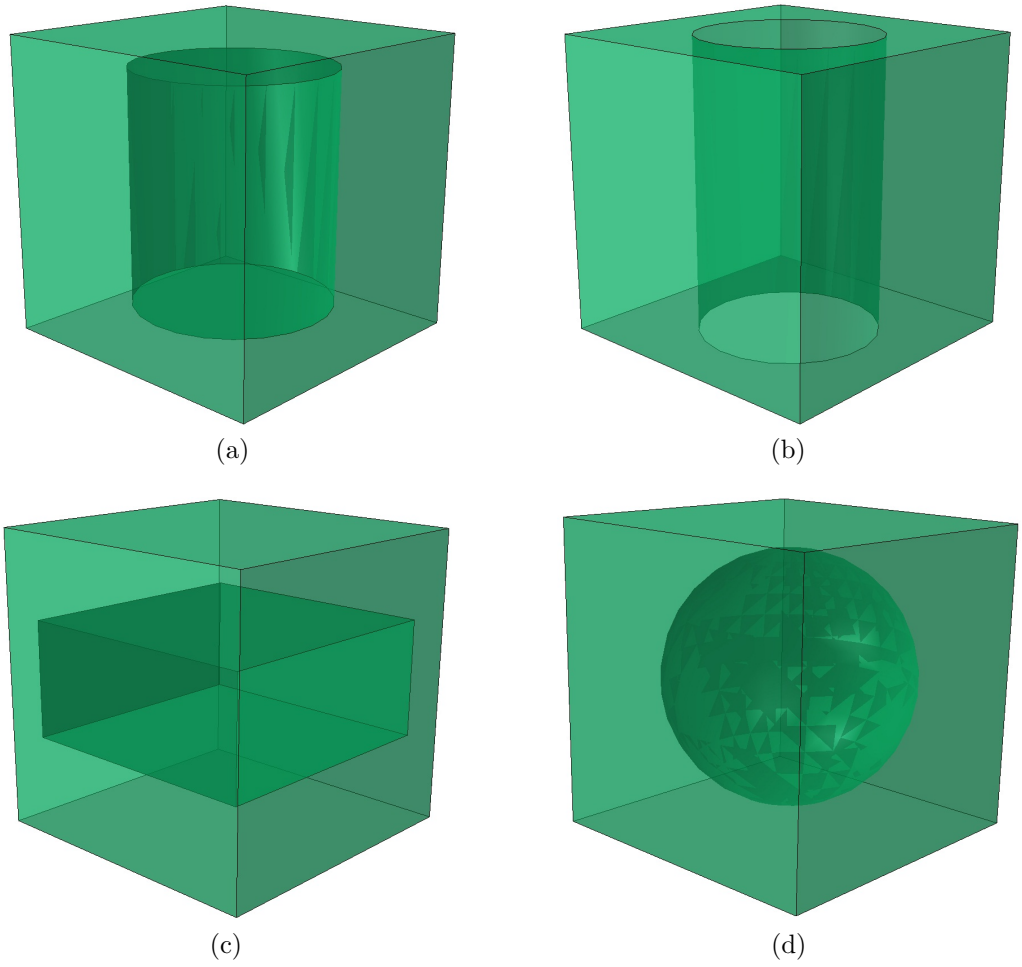

Figure 4: The schematic showing the various unit cells studied in the present work where, a) 0-3 type cylinder; b) 1-3 type cylinder; c) 0-3 type flat cuboidal; d)0-3 type sphere

The three-dimensional finite element model used in the current study was developed by Kar-Gupta and Venkatesh [23]. According to their formulation to maintain the periodicity of the electromechanical loading across the boundary of the unit cell the conditions that have to be imposed are:

(i) Periodicity in the $1-$ direction is given by :$P^R - P^A = P^S - P^B$;
$P^{RR} - P^{AA} = P^{SS} - P^{BB}$; $P^V - P^A = P^W - P^B$;
$P^{VV} - P^{DD} = P^{WW} - P^{CC}$; $P^{XM} - P^A = P^{XP} - P^B$

(ii) Periodicity in the $2-$ direction is given by :$P^T - P^D = P^U - P^A$;
$P^{TT} - P^{DD} = P^{UU} - P^{AA}$; $P^{WW} - P^C = P^W - P^B$;
$P^{YP} - P^C = P^{YM} - P^B$; $P^{XM} - P^A = P^{XP} - P^B$

(iii) Periodicity in the $3-$ direction is given by :$P^{UU} - P^{AA} = P^U - P^A$;
$P^{SS} - P^{AA} = P^S - P^A$; $P^{ZP} - P^{AA} = P^{ZM} - P^A$;

The unit cell for a 0-3 type unit cell with a cylindrical void is given in Fig.5

By subjecting a particular unit cell to a set of controlled mechanical and electrical loading conditions and studying its response all 45 corresponding material constants can be determined. The main feature of this three-dimensional finite element model is that all four types of unit cells are subject to a common set of electrical and mechanical loading conditions in order to determine the components of the electroelastic moduli of a given composite.
The finite element analysis for the unit cell is carried out by commercially available software (ABAQUS). Eight-node linear piezoelectric brick (C3D8E) elements are used to mesh the unit cell. Each node is allowed a total of four degrees of freedom (i.e. 1, 2, 3) and one electric potential degree of freedom (i.e. 9). The nodes located on the vertices of the unit cell, $A(AA)$, $B(BB)$, $C(CC)$, $D(DD)$, are designated as mater nodes, and P refers to all the four degrees of freedom (i.e. $P = 1, 2, 3, 9$). The constraint equations are such that they allow the master nodes to control the overall behaviour of the unit cell. All loads (mechanical and electrical) are applied to the master nodes only. The

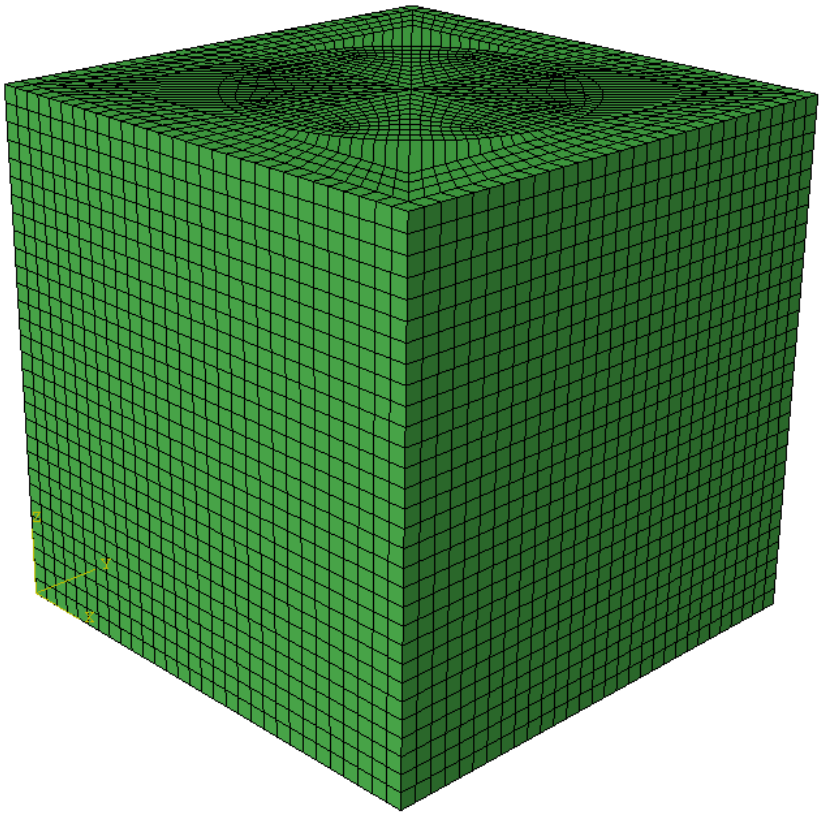

Figure 5: The diagram shows an example for a mesh for a 0-3 type cylindrical void of 30% volume fraction in a unit cell .

master node A is fixed and electrically grounded for all simulations to prevent rigid body motion ($P^A = 0$ for $P = 1, 2, 3, 9$). The masters nodes are shown in Fig.6

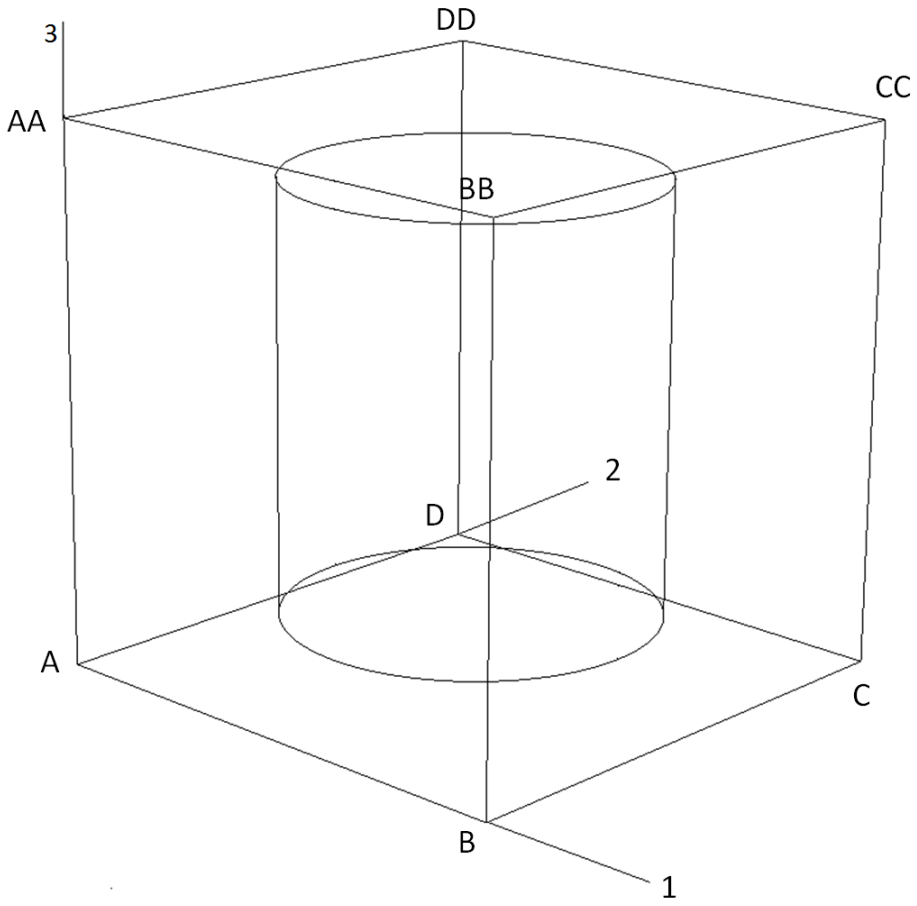

Figure 6: The diagram shows the master nodes used to control the boundary conditions and deformation of the unit cell.

A detailed description of the constraint equations and the method used to determine all 45 (21 elastic, 15 piezoelectric, and 6 dielectric) independent electroelastic constants has been given in the Appendix of Ref. [23]. The method to calculate the electric displacement using the weighted average method for

the case of 0-3 type cylindrical pore is given below.

Care has to be taken to mesh the 0-3 type porous cylindrical system in ABAQUS since the default meshing tool assigned for such a geometric configuration does not use hexes and wedges as the mesh element type. In order to mesh the system using a structured mesh (which is the standard mesh type) the unit cell has to be partitioned accordingly. A key feature in enabling ABAQUS to mesh the unit cell structurally involves the partitioning of the ZP and ZM faces. A circle with the same radius as that of the 0-3 type cylindrical pore has to be projected on the ZP (or ZM) face and extruded vertically through the entire unit cell. The circles then have to be divided into segments in order to enable accurate seeding of the mesh. In order for the constraint equations to control the electromechanical response of the unit cell, nodes on opposite faces and edges have to correspond to be exactly opposite to one another. For e.g. if node $R(1)$ is assigned the coordinates $(0, 1, 0)$, node $S(1)$ has to be $(30, 1, 0)$.

The appendix of Ref. [23] contains details on how to calculate the stress and electric displacement components. In order to completely characterize the behaviour of a unit cell containing a 0-3 type cylindrical pore all 81 components of the electromechanical moduli are calculated from a set of 9 finite element simulations. Each simulation helps in determining 9 constants. For e.g. in the first simulation, we assign, $\varepsilon_1 = \delta$, and, $\varepsilon_2, \varepsilon_3, \varepsilon_4, \varepsilon_5, \varepsilon_6, E_1, E_2, E_3 = 0$ we get all the nine constants in the first column $(L_{11}, L_{21}, L_{31}, L_{41}, L_{51}, L_{61}, e_{11}, e_{21}, e_{31})$.To determine the piezoelectric and permittivity constants in the longitudinal direction (e.g. e_{33}, κ_{33}) the electric displacement components have to be calculated using a weighted average method, a brief description of which is given below.

To determine the constants in the third column of the electromechanical constants matrix the following conditions are imposed.

1. The unit cell is subjected to a normal strain ε_3 in the +3 direction by prescribing a fixed displacement (δ). The displacement is assigned to the master nodes on the face having its outward normal vector in the +3 direction (i.e. nodes $AA-BB-CC-DD$ on the ZP face). The master nodes on the face having its outward normal in the -3 direction are fixed (i.e. nodes $A-B-C-D$ on the ZM face). The remaining strain components are fixed and all the master nodes are electrically grounded $\varepsilon_1, \varepsilon_2, \varepsilon_4, \varepsilon_5, \varepsilon_6, E_1, E_2, E_3 = 0$

$$P^{AA} = P^{BB} = P^{CC} = P^{DD} = \delta, \text{for } P = 3 \tag{124}$$

$$P^{AA} = P^{BB} = P^{CC} = P^{DD} = 0, \text{for } P = 1, 2, 9 \tag{125}$$

$$P^{A} = P^{B} = P^{C} = P^{D} = 0, \text{for } P = 1, 2, 3, 9 \tag{126}$$

2. All the six stress components ($\sigma_1, \sigma_2, \sigma_3, \sigma_4, \sigma_5, \sigma_6$) are calculated according to the method prescribed in the Appendix A of Ref. [23] which can be represented in matrix form as follows:

$$\begin{pmatrix} \sigma_1 \\ \sigma_2 \\ \vdots \\ D_3 \end{pmatrix} = \begin{pmatrix} L_{11} & L_{12} & \cdots & -e_{31} \\ L_{12} & L_{22} & \cdots & -e_{32} \\ \vdots & \vdots & \ddots & \vdots \\ e_{31} & e_{32} & \cdots & \kappa_{33} \end{pmatrix} \begin{pmatrix} \varepsilon_1 \\ \varepsilon_2 \\ \vdots \\ E_3 \end{pmatrix} \tag{127}$$

3. The three electric displacement components ($\langle D_1 \rangle, \langle D_2 \rangle, \langle D_3 \rangle$) required to determine the piezoelectric components in the third column (e_{13}, e_{23}, e_{33}) are calculated as a weighted area average.

For example,

$$e_{33} = \frac{\langle D_3 \rangle}{\varepsilon_3}$$

$\langle D_3 \rangle$ = magnitude of the electric displacement component normal to the face ZP evaluated as a weighted area average.

The formula employed to evaluate the weighted average of the electric displacement is

$\langle D_3 \rangle = (D_{face} \times A_{face})/N_{face} + (D_{circle} \times A_{circle})/N_{circle}$
D_{face} = electric displacement of the ZP face not including electric displacement the projected circle.
A_{face} = Area of the ZP face not including the area of the projected circle.
N_{face} = Number of elements on the ZP face not including the elements in the projected circle.
D_{circle}= electric displacement of the circle projected on the ZP.
A_{circle}= Area of the projected circle on the ZP face.
N_{circle}= Number of elements in the projected circle on the ZP face.

Similarly by using the other boundary conditions (e.g. $\varepsilon_2 \neq 0, \varepsilon_4 \neq 0, etc.$) all 81 constants in the material property matrix (of which 45 are truly independent) can be determined. It is essential to calculate the electric displacement components using the weighted area average in order for the electromechanical constants matrix to have major symmetry.

The following section highlights some of the important results and discussions inferred from the present study.

CHAPTER 10

Results and discussion

This section analyses the results of the explicit homogenization estimates of the analytic model and compares the trends in the fundamental properties with an existing finite-element model developed by Kar-Gupta and Venkatesh [23] and adapted to porous piezoelectric composites by [18]. Plots for the variations (Fig.7) in the trends of effective properties with respect to porosity volume fraction are given for two geometric configurations of pores embedded in a piezoelectric matrix, namely, square distribution of long cylindrical pores aligned with the axis of poling (e_3) in the $e_1 - e_2$ direction (SA) and cubic distribution of spherical voids (CA). Moreover to demonstrate the applicability of the analytic model three materials belonging to different crystal symmetry classes (Barium Titanate (4mm), Barium Sodium Niobate (mm2), and Lithium Niobate (3m)) have been taken as examples. The utility of the analytic model has been shown by identifying certain figures of merit to facilitate material selection for industrial applications.

This section has been organized as follows. First we plot the results for the comparison between trends obtained from the analytic model developed in the part I with finite-element simulations for barium titanate, barium sodium niobate, and lithium niobate. Next we plot the results showing the trends in certain figures of merit for both square and cubic distributions of voids with increasing porosity volume fraction. The motivation behind the selection of

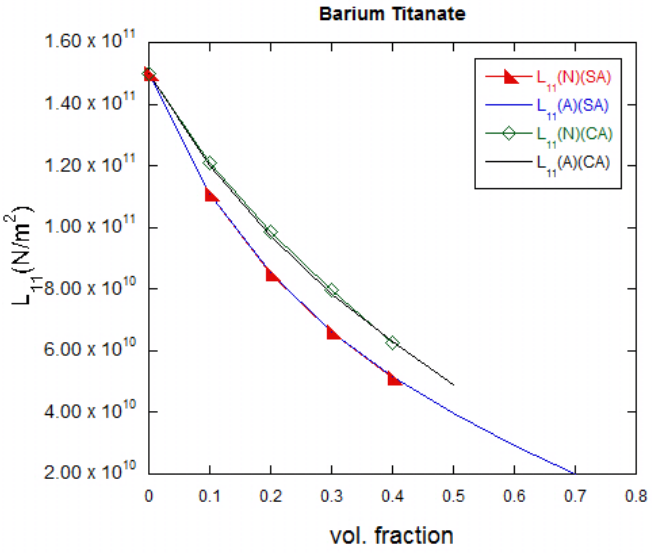

(a)

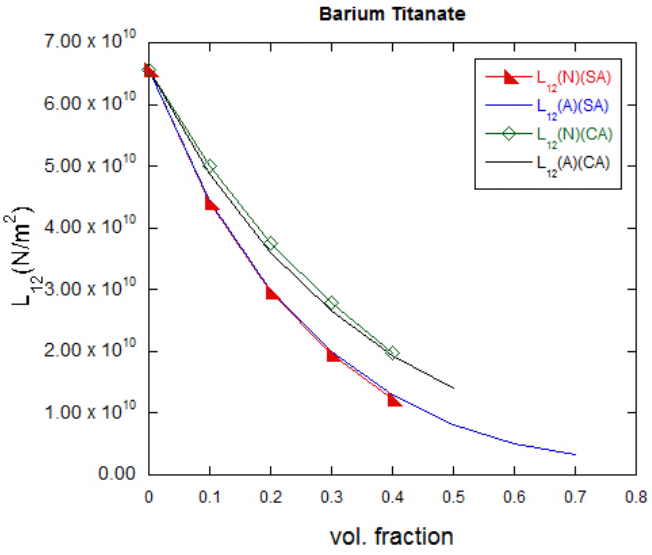

(b)

Figure 7: Trends showing the variation of elastic constants for Barium Titanate-1, (N) implying numerical results and (A) denotes the analytic line.

these results is to provide an overall understanding of the effective response of piezoelectric porous periodic composites. The square and cubic arrangements being the limiting cases of a general ellipsoidal particle.

10.1 Distribution of long cylindrical voids and spherical voids

The variation in the effective elastic properties with change in porosity volume fraction as predicted by the analytic model are compared with the three-dimensional finite element model for a square distribution (SA) of long hollow cylindrical voids and a cubic distribution (CA) spherical voids embedded in a piezoelectric matrix. The comparison between finite element and analytic predictions show a good agreement over the entire range of porosity volume fraction. The analytic model shows the change in effective properties upto 70% volume fraction (with percolation occurring at $\sim 78\%$) for long cylindrical voids and upto 50% (with percolation taking place at $\sim 52\%$). The trends are analysed for three materials, Barium Sodium Niobate, Lithium Niobate and Barium Titanate.

10.1.1 Barium Titanate

The analytic model was first applied to a square and cubic arrangement of cylindrical and spherical voids in a matrix Barium Titanate. The trends were observed for all fundamental electromechanical constants for a varying porosity volume fraction. The theory predicts values for the piezoelectric constants that are self consistent and satisfy the necessary symmetry conditions required for respective tensors. It was observed that effective properties show orthotropic symmetry in the material parameters. As predicted by earlier work properties in the longitudinal direction ($L_{33}, e_{33}, \kappa_{33}$) show a larger value for a square distribution of cylindrical voids when compared with a cubic arrangement of spherical voids. The prediction of transverse and shear properties also show good agreement with finite-element simulation thereby validating the

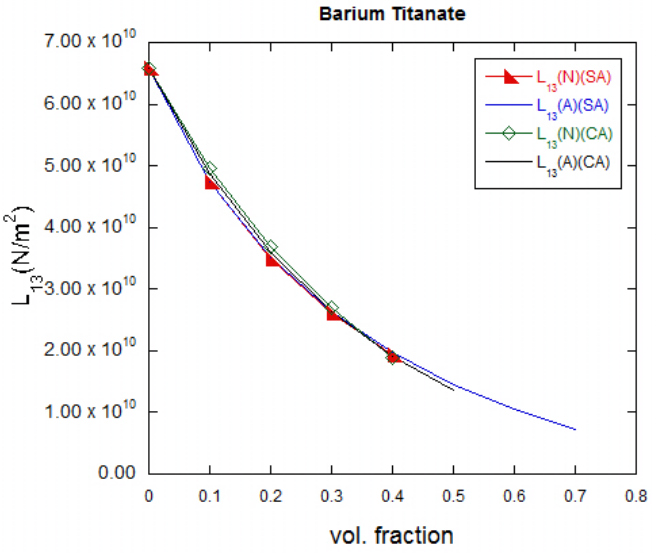

(a)

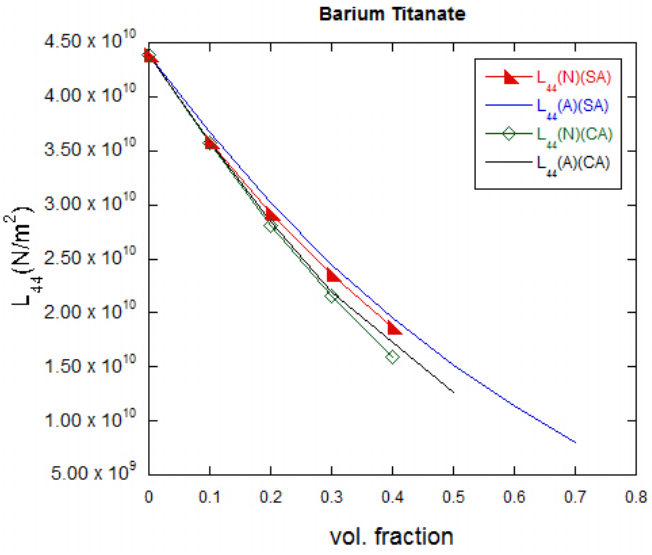

(b)

Figure 8: Trends showing the variation of elastic constants for Barium Titanate-2

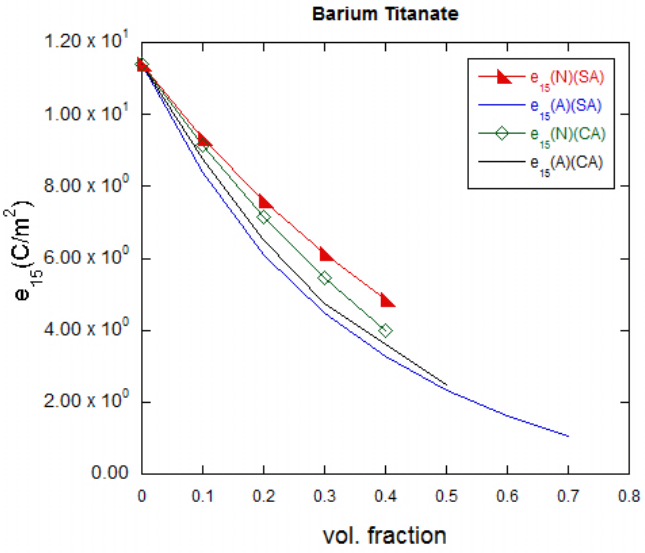

(a)

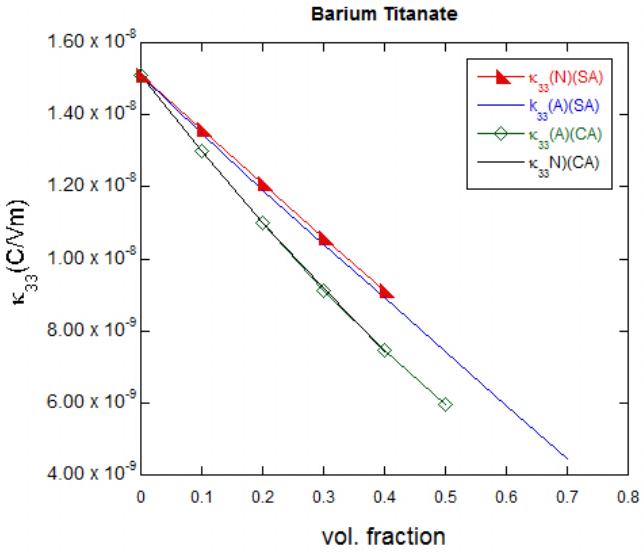

(b)

Figure 9: Trends showing the variation of piezoelectric and dielectric constants for Barium Titanate-3

assumption of piece-wise constant polarization fields. It is observed from the Figs.(8, 9) that the behaviour is monotonic in the variation of fundamental constants. A linear trend as predicted by previous finite-element models [18] is observed in the longitudinal constants.

10.1.2 Barium Sodium Niobate

To assess the applicability of the analytic model to materials with higher degree of anisotropy the model was applied to a square and cubic arrangement of cylindrical and spherical voids in a matrix of Barium Sodium Niobate (mm2)(Fig.10,11). It was observed that the fundamental constants predicted as a result of the homogenization estimates of the analytic model agreed well with finite-element simulations. The explicit solution for the effective properties are general and do not depend on the symmetry of the material parameters of the matrix phase. The trends observed were similar in comparison with those observed in Barium Titanate with the overall properties of the composite having orthotropic symmetries and satisfying the required symmetry conditions of the respective elastic, piezoelectric and dielectric modulus tensors.

10.1.3 Lithium Niobate

The analytic model predictions were finally compared with finite-element simulations by substituting the properties of Lithium Niobate (3m) for the properties of the matrix. The trends were seen to agree well with numerical model predictions upto large volume fractions. The symmetries of the effective constants were checked and found to exist for all fundamental properties. The trends for electromechanical constants for Lithium Niobate are given in Fig.12,44

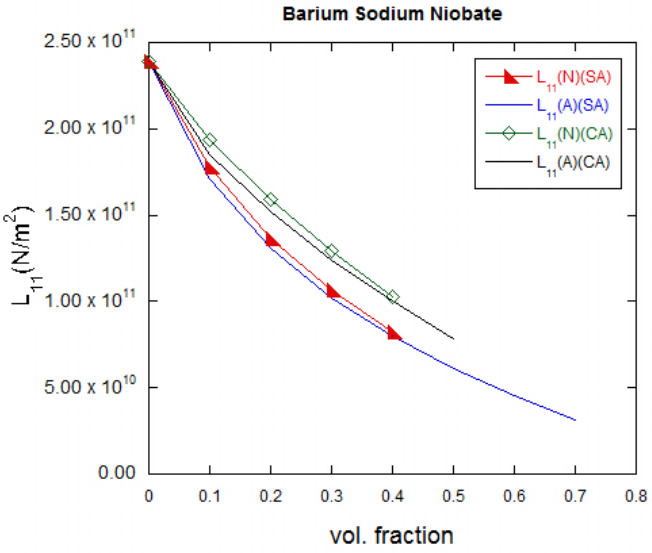

(a)

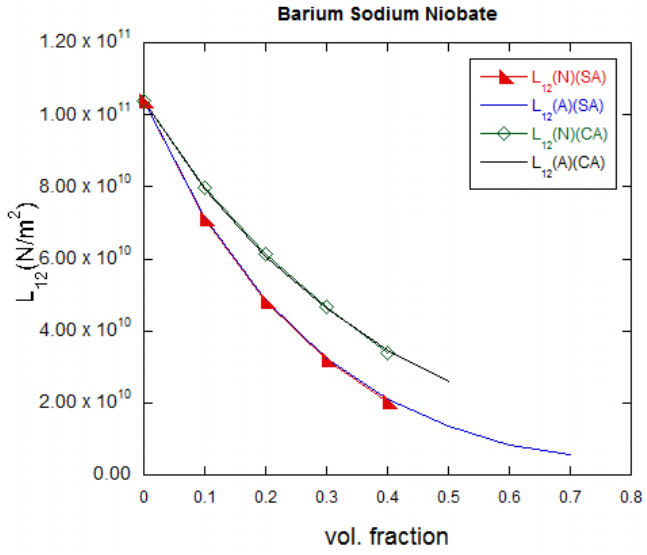

(b)

Figure 10: Trends showing the variation of elastic constants for Barium Sodium Niobate-1.

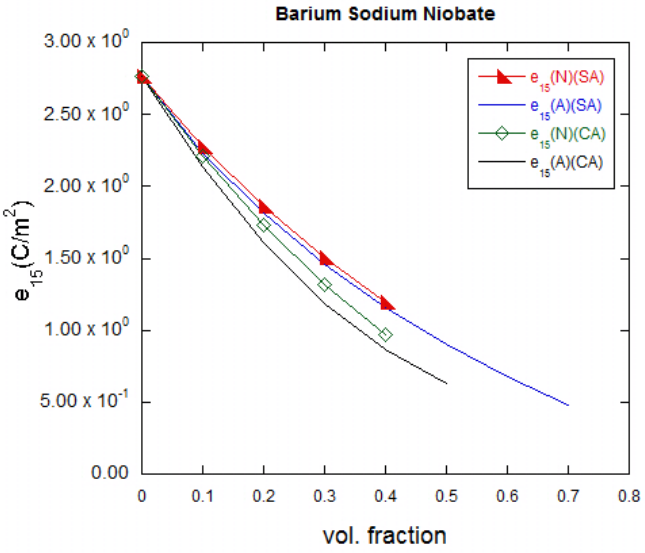

(a)

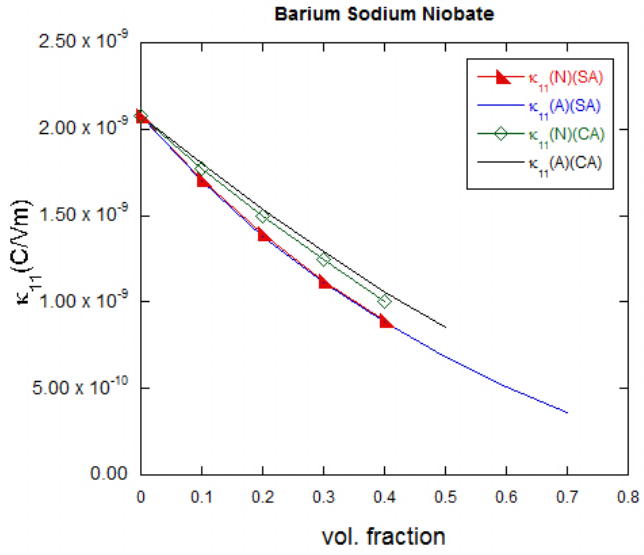

(b)

Figure 11: Trends showing the variation of piezoelectric and dielectric constants for Barium Sodium Niobate-2.

10.1.4 Remarks

The variation in fundamental properties provided by the analytic model helps in understanding the effects of changing porosity volume fraction. The model can be shown to recover the solution Eshelby in the dilute limit of porosity tending to zero. The explicit solutions provided for the effective properties can be applied to a wide range of materials with varying symmetries in their fundamental properties. The rigorous formulation and effectiveness of the homogenization estimates provide a strong substitute to popular finite-element schemes generally used to study the effective behaviour of periodic piezoelectric composites. Unlike some analytic model the estimates based on Suquet's method does not require the use of existing schemes to observe the change in properties for a finite volume fraction. Moreover for particulate composites where the inclusion and the matrix are both piezoelectric, the model provides explicit solutions for the Hashin-Shtrikman (HS) variational bounds depending on the choice of the reference medium. If the reference medium is chosen as the stiffer of the two phases, the model provides the HS upper bound. Similarly when the softer materials is chosen as the reference medium, we obtain the HS lower bound.

10.2 Finite-element model predictions

The three-dimensional finite element model was implemented for four geometric configurations of porous composites with three different crystal symmetries (4mm, mm2, and 3m). The results of the 1-3 type long porous composite is first verified with previous finite element models [23, 21, 22] developed for 1-3 type porous composites and found to be in good agreement. The model is then applied to 0-3 type cylindrical porous, 0-3 type flat cuboidal porous and 0-3 type spherical porous composites for all three crystal symmetries. The role of crystal symmetry and porosity connectivity on the fundamental properties is analysed for four geometric configurations of porous piezoelectric composites. The performance characteristics of each are determined in the light of relevant

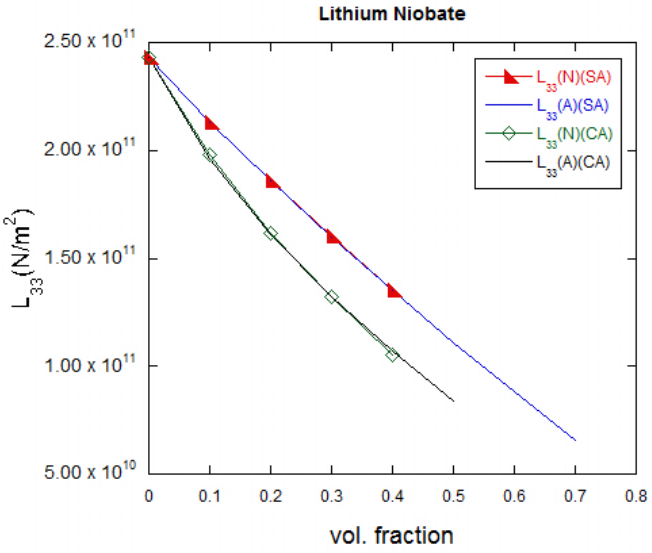

(a)

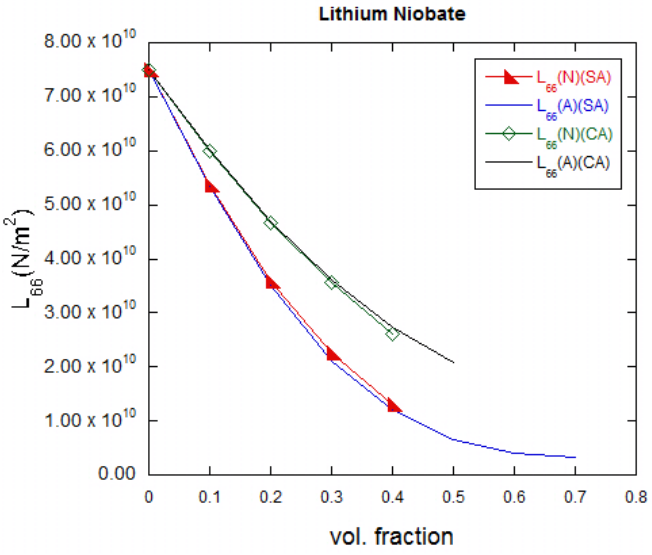

(b)

Figure 12: Trends showing the variation of elastic constants for Lithium Niobate-1.

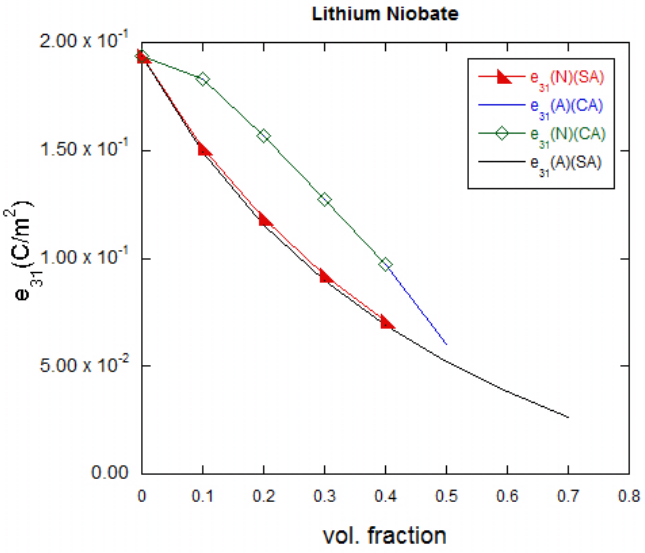

(a)

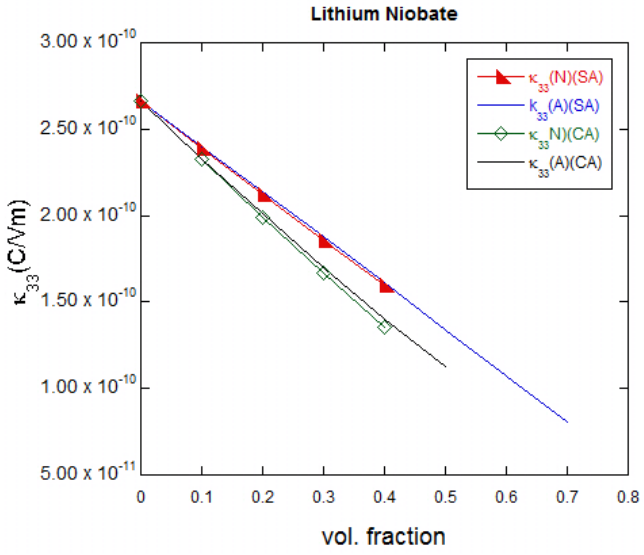

(b)

Figure 13: Trends showing the variation of piezoelectric and dielectric constants for Lithium Niobate-2.

figures of merit.

10.2.1 Effect on fundamental electromechanical properties

The variation of the fundamental elastic, piezoelectric and dielectric constants with increasing porosity volume fraction is shown in Fig. for ceramic $BaTiO_3$ for all four geometric connectivities (poled in the 3-direction). The general observations are as follows:

1. The variation of the electroelastic properties of all geometric configurations with increasing porosity volume fraction is similar across material symmetries.

2. The properties in the longitudinal direction (i.e. $L_{33}, e_{33}, \kappa_{33}$) are highest in the case of 1-3 type long porous composite as shown in Fig.14 The variation of the electromechanical constants is mostly linear with increasing porosity volume fraction. The lowest values for longitudinal constants are seen in the case of the 0-3 type porous cuboidal composite with the 0-3 type cylinder and 0-3 type spherical pores showing intermediate trends between the two bounds. The longitudinal constants for 0-3 type composites is significantly lower than those of 1-3 type composites because of the higher volume fraction of the pore along the 3-direction. The 0-3 type composite, however, shows a matrix (ceramic)-dominated non-linear behaviour due to the pore being completely enclosed in the ceramic matrix phase.

3. The properties in the transverse direction (i.e. $L_{11}, L_{22}, \kappa_{11}$) are highest for the 0-3 type cuboidal porous composite while the 1-3 type long porous composites have the lowest values for the transverse properties. As expected, for all geometric configurations the transverse constants show a monotonically decreasing trend with an increase in the porosity volume fraction. The properties exhibit characteristics of matrix-dominated behaviour in each of the two transverse (i.e. 1 and 2) directions.

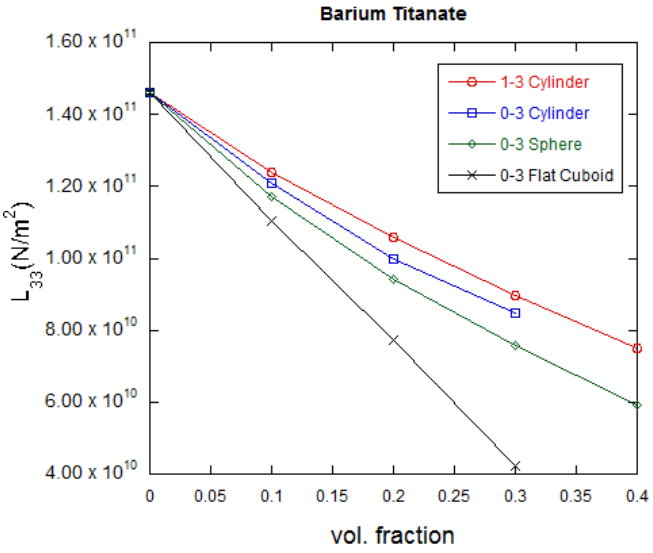

(a)

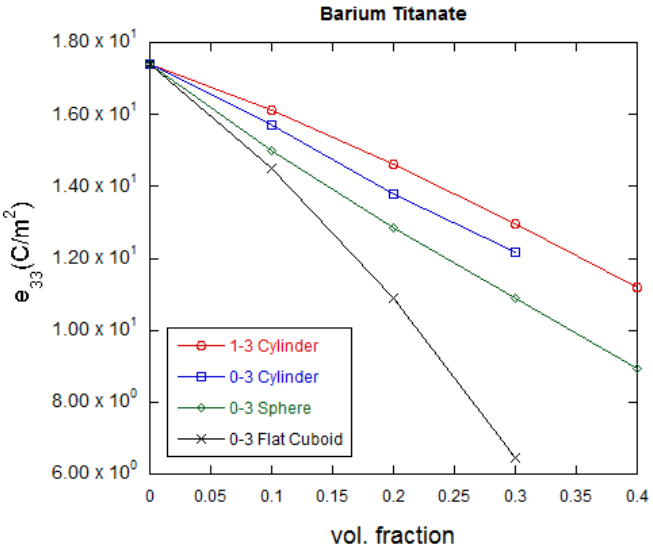

(b)

Figure 14: Trends showing the finite-element results for Barium Titanate-1

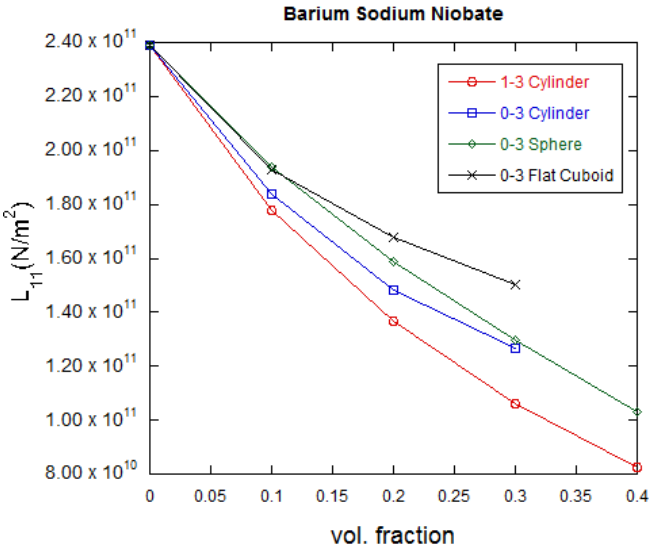

(a)

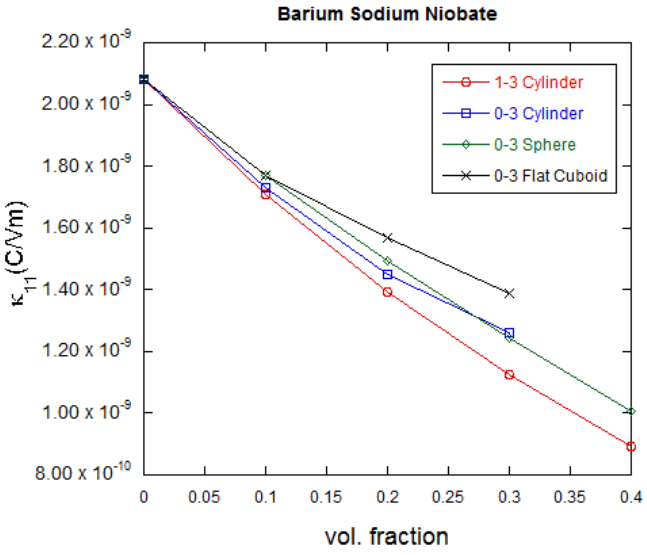

(b)

Figure 15: Trends showing the finite-element results for Barium Sodium Niobate-1

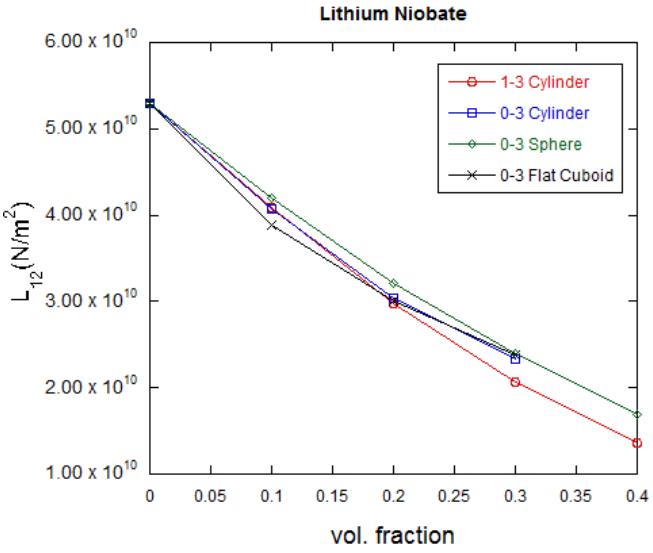

(a)

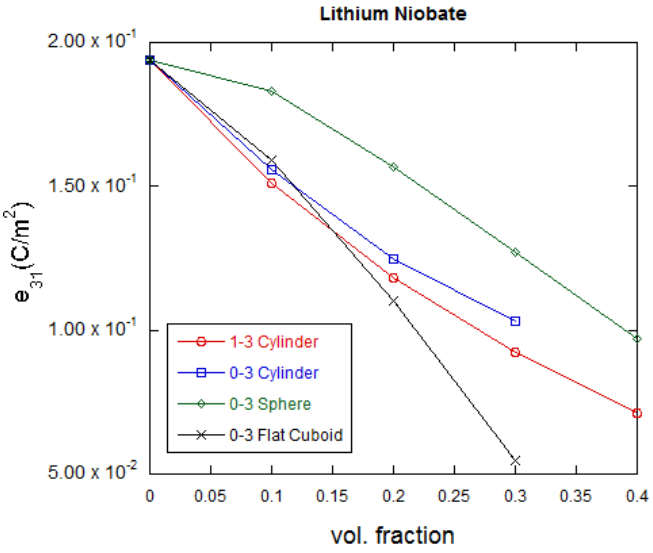

(b)

Figure 16: Trends showing the finite-element results for Lithium Niobate-1

4. The properties, $L_{12}, L_{13}, L_{23}, e_{31}$, are also dependent on the nature of the geometric connectivity of the pore with the 0-3 type spherical and 0-3 type cuboidal pore having the highest values for the constants for the case of a Barium Titanate system. (The trends differ in the case of Barium Sodium Niobate and Lithium Niobate system where the 0-3 spherical pore shows the highest value for the properties).

5. The properties L_{44}, L_{55}, L_{66} show a matrix-dominated trend with L_{44} and L_{55} being highest for 1-3 type long porous composite. The highest value for L_{66} is obtained for the 0-3 cuboidal porous system.

The overall trends for the electromechanical properties with varying porosity volume fraction show a strong dependence on the load partitioning between the matrix and the porous region, which in turn is influenced by the geometric connectivity of the pore within the ceramic phase.

10.2.2 Effects on Crystal Symmetry

The finite element model used in the study of porous piezoelectric composite enables the determination of 45 independent electromechanical constants. The influence of the geometric arrangements of the pores on the crystal group of the matrix phase can be studied by looking at the relationship between the independent electromechanical properties. In the model system consisting of Barium Titanate as the matrix phase, a high order of crystal symmetry (i.e. 6mm) is observed. By introducing porosity into the system the crystal symmetry is reduced to the 4mm group (i.e. $L_{66} \neq (L_{11} - L_{12})/2$). For the Barium Sodium Niobate (mm2) and Lithium Niobate (3m) based porous-ceramic composite system no change in crystal symmetry is noted with the introduction of porosity.

10.2.3 Effects on Figures of Merit

The following observations were made after a study on the role of porosity geometry on the effective figures of merits:

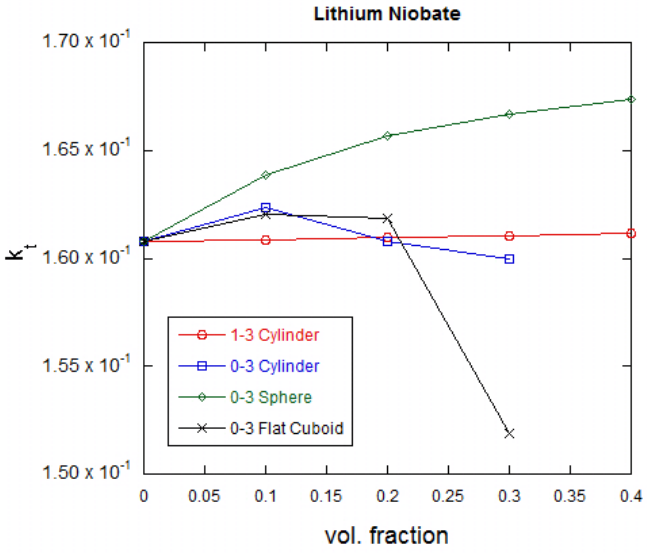

(a)

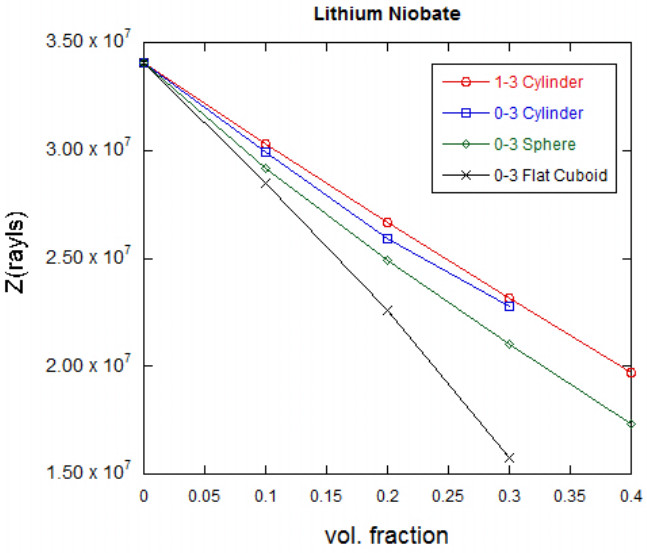

(b)

Figure 17: Trends showing the Figures of merit for Lithium Niobate-1

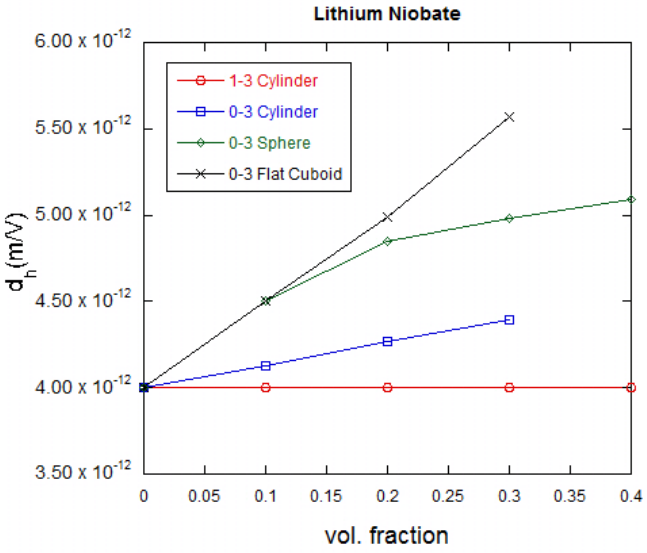

(a)

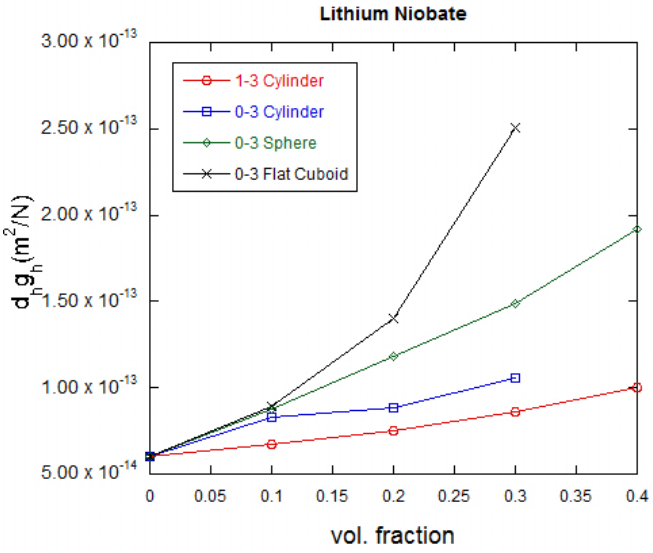

(b)

Figure 18: Trends showing the Figures of merit for Litihum Niobate-2

1. Overall, the electromechanical coupling constant (k_t) shows an increasing trend with an increase in the porosity volume fraction for a Barium Titanate based porous-ceramic system. The highest value for k_t was observed in the case of 1-3 type long porous composite as shown in Fig.19. The coupling constant for 0-3 type spherical and 0-3 type cuboidal porous systems have the lowest values with the 0-3 type cuboidal porous system showing an almost linear trend with increasing porosity volume fraction. The trends for k_t in the case of Barium Sodium Niobate and Lithium Niobate system show invariance with increasing porosity volume fraction with the highest values being observed for 1-3 type long pores and 0-3 type spherical pores respectively can be seen in Figs.17, 20.

2. The trends for acoustic impedance (Z) show a linearly decreasing trend with increasing porosity volume fraction. The highest value for acoustic impedance in all porous-ceramic configurations was obtained for 1-3 type long circular cross-sectional pores. 0-3 flat cuboidal pores had the lowest value for acoustic impedance in all cases of ceramic-porous configurations.

3. The piezoelectric charge coefficient (d_h) and hydrostatic figure of merit ($d_h g_h$) are highest for the 0-3 type flat cuboidal pore and lowest for 1-3 type long cylindrical pore. The difference in the d_h and $d_h g_h$ value between the 0-3 type flat cuboidal pore and other geometric configuration is quite significant (upto 223% and 1818% respectively, between 0-3 type flat cuboid and 1-3 type long cylindrical pore for ceramic Barium Titanate system) at 30% volume fraction. Similar trends were observed in the Barium Sodium Niobate and Lithium Niobate systems, where the 1-3 type flat cuboid had the highest value for the piezoelectric charge coefficient and the hydrostatic figure of merit as seen in Fig.20 The percentage difference for respective d_h and $d_h g_h$ values between 0-3 type flat cuboidal and 1-3 type long cylindrical pore being 24% and 117% for Barium Titanate (mm2) system and 40% and 191% for a Lithium Niobate (3m) system at 30% volume fraction. The charge coefficient for 1-3 type

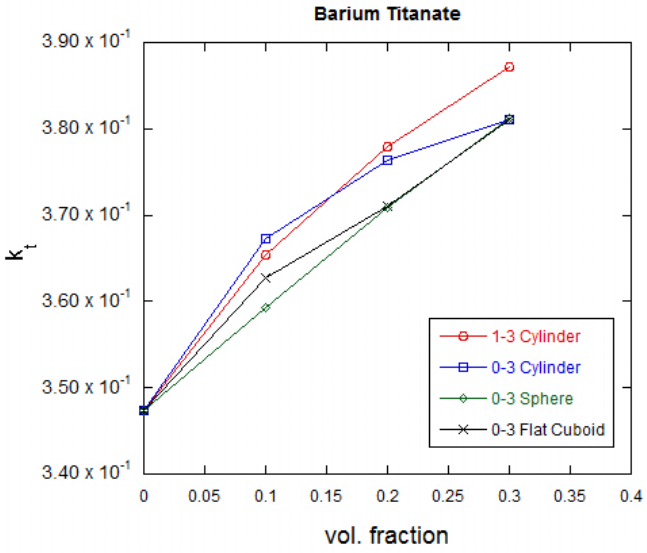

(a)

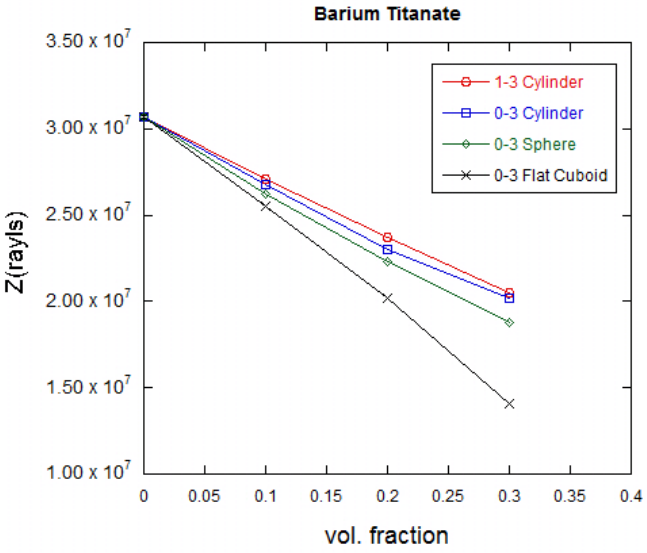

(b)

Figure 19: Trends showing the Figures of merit for Barium Titanate-1

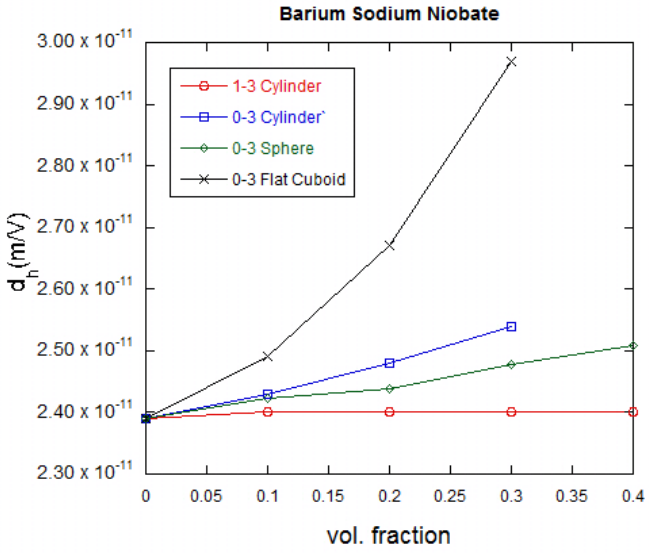

(a)

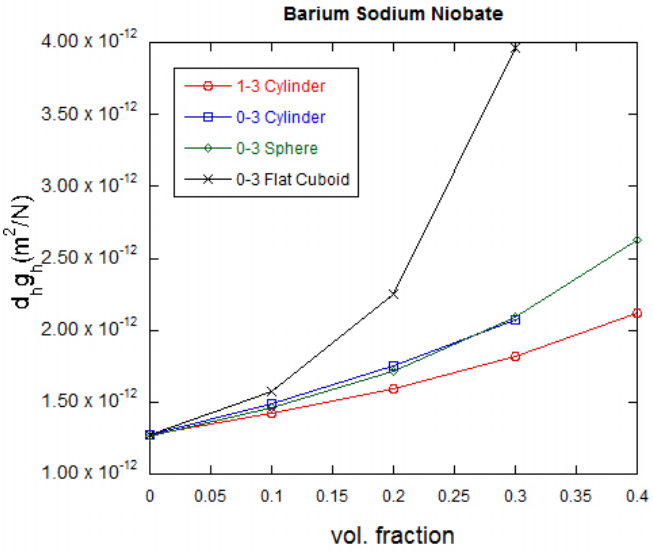

(b)

Figure 20: Trends showing the Figures of merit for Barium Sodium Niobate-1

porous system does not vary with change in porosity volume fraction, a trend which has been explained by the author in Ref. [18]

4. On analyzing the difference between d_h and $d_h g_h$ for 0-3 flat cuboidal pore and 0-3 long cylindrical porous system i.e. the two bounding geometric configuration of 0-3 type, a considerable improvement was noted in the figures of merit in the 0-3 cuboidal pore over the 0-3 cylindrical pore configuration. At the 30% volume fraction the percentage difference in d_h and $d_h g_h$ was observed to be 107% and 664% respectively in the case of Barium Titanate being used as the matrix phase. For the case where Barium Sodium Niobate and Lithium Niobate were as matrix phases the difference in d_h and $d_h g_h$ between the two geometric configurations at 30% volume fraction was found to be 17% and 91% and 27% and 137% respectively. These results show that 0-3 flat cuboidal pore configuration is better for hydrophone sensor applications in which a high d_h and $d_h g_h$ is considered desirable.

The important conclusions drawn from the finite element study of porous piezoelectric composites are highlighted in the following section.

CHAPTER 11

Conclusion

A three-dimensional finite element model and an analytic model based on the Suquet's estimates have been presented to analyse the effect of porosity geometry and connectivity on the electromechanical response of piezoelectric ceramics. The author had earlier compared the results of the finite element analysis to the analytic model presented by Mikata [18] for the case of a 0-3 type spherical pore in a piezoelectric medium. In this study the results for the case of a 1-3 type cylindrical pores and 0-3 type spherical pores have have been compared to an analytic model based on homogenization estimates. The principal conclusions drawn from the study are as follows:

1. The analytic model derived in the present work provides explicit solutions to the effective tensors of a two phase piezocomposite by extending the previous work by Suquet. The model is applied to three materials belonging to different symmetry classes for a case of a square distribution of cylindrical voids and a cubic distribution of spherical voids. The effective properties were found to show good agreement with the finite-element scheme developed in the second part of the current work.

2. The finite element model used in the present study was able to predict the electromechanical properties of four geometric configurations of pores i.e. 0-3 type cuboidal pore, 0-3 type spherical pore, 0-3 type cylindrical pore, and 1-3 type long cylindrical pore.

3. The unit-cell based three-dimensional finite element model produced results for the all the electromechanical properties of materials belonging to three different symmetry classes, i.e. Barium Titanate (4mm), Barium Sodium Niobate (mm2), and Lithium Niobate (3m).

4. The elastic, piezoelectric and dielectric properties vary monotonically with increase in porosity volume fraction with the constants in the longitudinal direction being greatest in the case of 1-3 type long pores with circular cross-section for all three symmetry classes.

5. On comparing the piezoelectric charge coefficient (d_h) and the hydrostatic figure of merit ($d_h g_h$) between the 0-3 type cylindrical pore and 0-3 type cuboidal pore, the latter was found to have a significantly larger value for the same volume fraction. This trend, of a thin flat pore having relatively higher d_h and $d_h g_h$ values, has been previously noted by Topolov et al. in [28], where they have considered a 0-0-3 system consisting of needle-like spheroidal pores embedded in a polymer matrix. The observed trends indicate that 0-3 type cuboidal pores are better suited for hydrophone applications.

Appendix A

The microstructural tensors P, $\boldsymbol{V}$, T

The explicit expressions for the components of the mircrostructural tensor **P**, which characterizes the microstructure of the square distribution of cylindrical pores and cubic distribution of spherical pores are given in this section.

A.1 Periodic square distribution

For the periodic square distribution of long cylindrical voids, the base vectors defined in section 3, so that expression for **P**, $\boldsymbol{V}$, **T** specializes to:

$$P_{ijkl} = \sum_{\substack{p=-\infty \\ -\{p=q=0\}}}^{+\infty} \sum_{q=-\infty}^{+\infty} H_{ijmn} \frac{4J_1^2(bk)}{b^2k^2}, \tag{128}$$

$$V_{ijk} = \sum_{\substack{p=-\infty \\ -\{p=q=0\}}}^{+\infty} \sum_{q=-\infty}^{+\infty} J_{ijk} \frac{4J_1^2(bk)}{b^2k^2}, \tag{129}$$

$$T_{ij} = \sum_{\substack{p=-\infty \\ -\{p=q=0\}}}^{+\infty} \sum_{q=-\infty}^{+\infty} G_{ij} \frac{4J_1^2(bk)}{b^2k^2}, \tag{130}$$

where $\xi_1 = p$, $\xi_2 = q$, $b = \sqrt{\frac{c^{(2)}}{\pi}}$, and $k = 2\pi\sqrt{p^2+q^2}$ and it is recalled that $J_1(\cdot)$ is the Bessel function of first kind and $c^{(2)}$ is the volume fraction of the particle phase.

A.2 Periodic cubic distribution

For the periodic cubic distribution of spherical voids, the expressions for $\mathbf{P}$, $\boldsymbol{V}$, $\mathbf{T}$ specializes to:

$$P_{ijkl} = \sum_{\substack{p=-\infty \\ -\{p=q=r=0\}}}^{+\infty} \sum_{q=-\infty}^{+\infty} \sum_{r=-\infty}^{+\infty} H_{ijmn} \left[\frac{3\left(-bk\cos(bk) + \sin(bk)\right)}{b^3k^3} \right]^2, \tag{131}$$

$$V_{ijk} = \sum_{\substack{p=-\infty \\ -\{p=q=r=0\}}}^{+\infty} \sum_{q=-\infty}^{+\infty} \sum_{r=-\infty}^{+\infty} J_{ijk} \left[\frac{3\left(-bk\cos(bk) + \sin(bk)\right)}{b^3k^3} \right]^2, \tag{132}$$

$$T_{ij} = \sum_{\substack{p=-\infty \\ -\{p=q=r=0\}}}^{+\infty} \sum_{q=-\infty}^{+\infty} \sum_{r=-\infty}^{+\infty} T_{ij} \left[\frac{3\left(-bk\cos(bk) + \sin(bk)\right)}{b^3k^3} \right]^2, \tag{133}$$

where $\xi_1 = p$, $\xi_2 = q$, $\xi_3 = r$, $b = \left[\frac{3c^{(2)}}{4\pi}\right]^{\frac{1}{3}}$, and $k = 2\pi\sqrt{p^2+q^2+r^2}$.

Appendix B

Additional plots for Barium Titanate, Barium Sodium Niobate and Lithium Niobate

Additional results from finite-element analysis and the analytic model have been presented in this appendix.

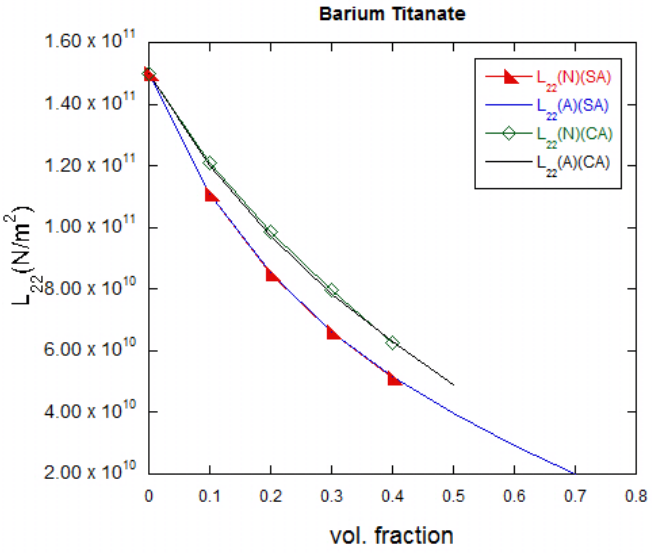

(a)

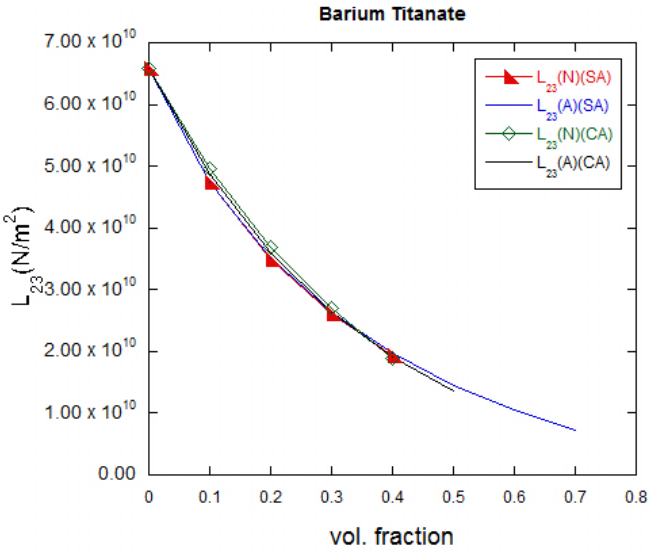

(b)

Figure 21: Trends showing the variation of elastic constants for Barium Titanate-4.

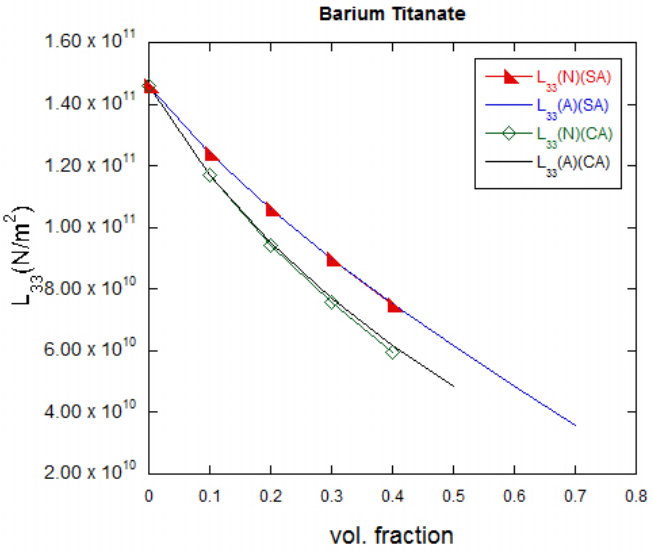

(a)

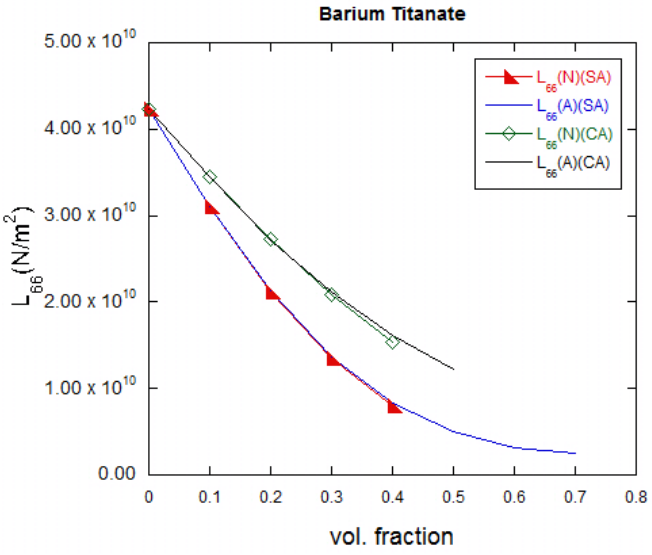

(b)

Figure 22: Trends showing the variation of elastic constants for Barium Titanate-5.

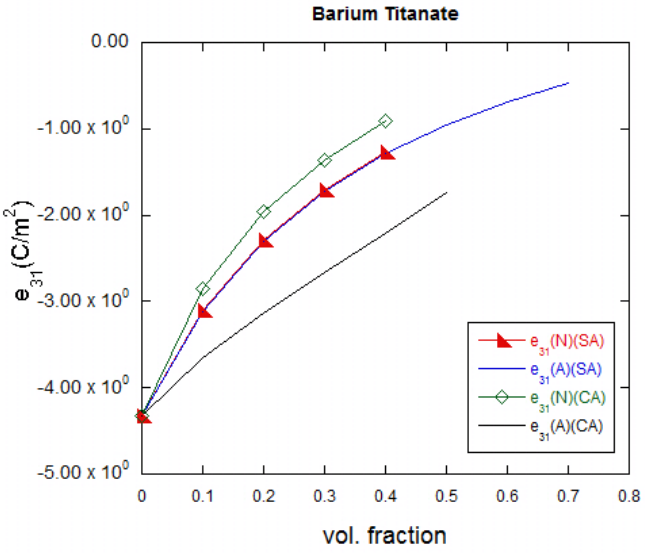

(a)

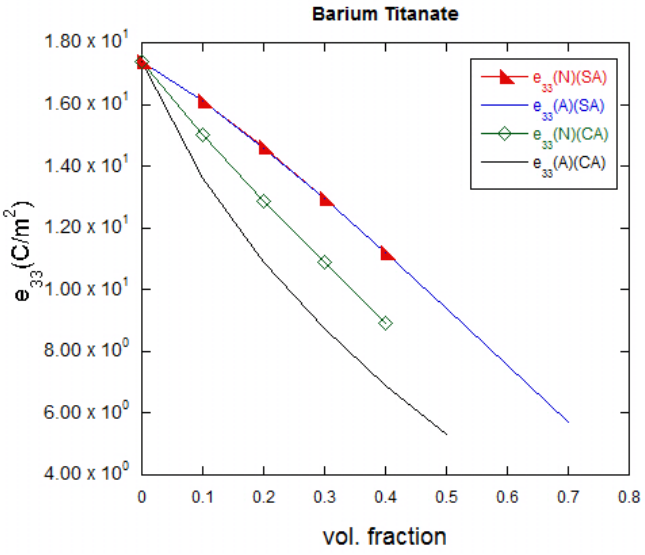

(b)

Figure 23: Trends showing the variation of piezoelectric constants for Barium Titanate-6.

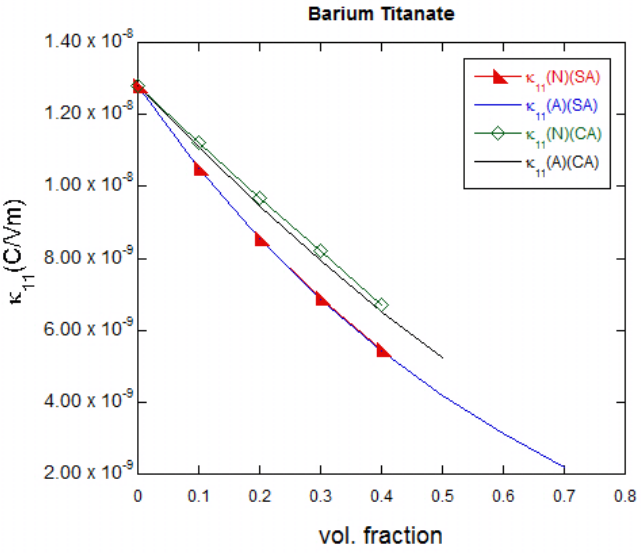

(a)

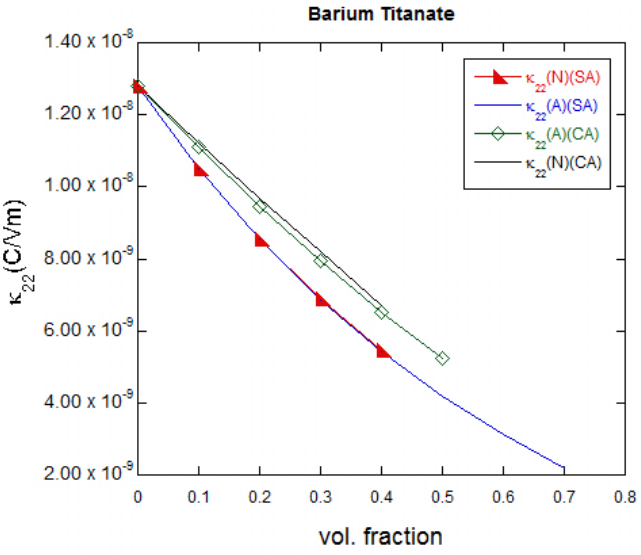

(b)

Figure 24: Trends showing the variation of dielectric constants for Barium Titanate-7.

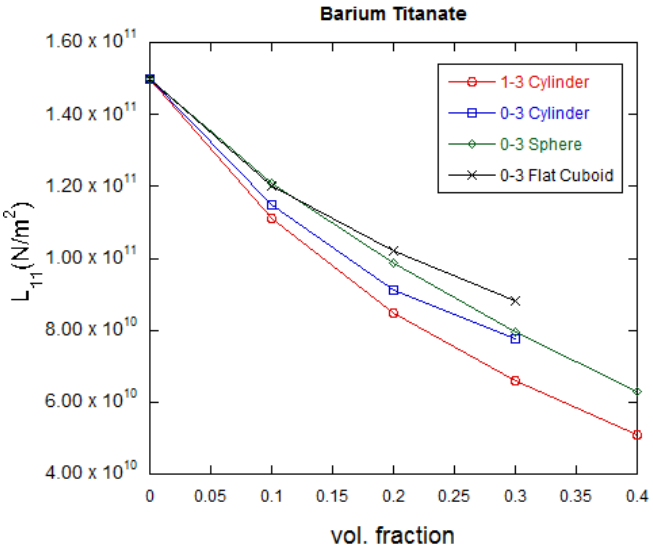

(a)

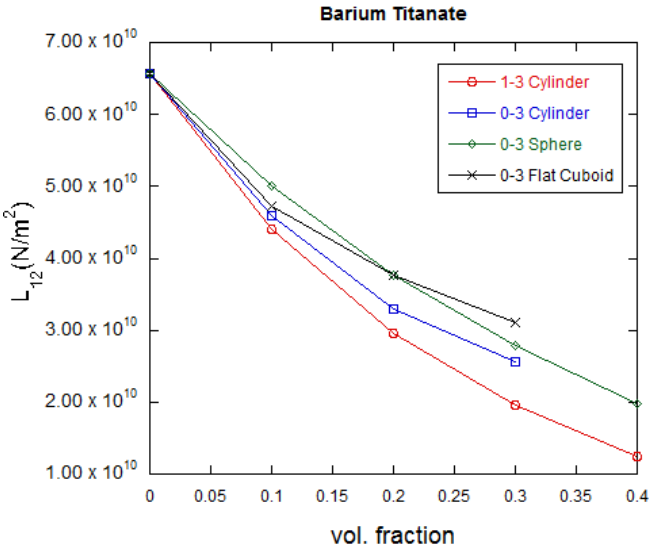

(b)

Figure 25: Trends showing the finite-element results for Barium Titanate-2

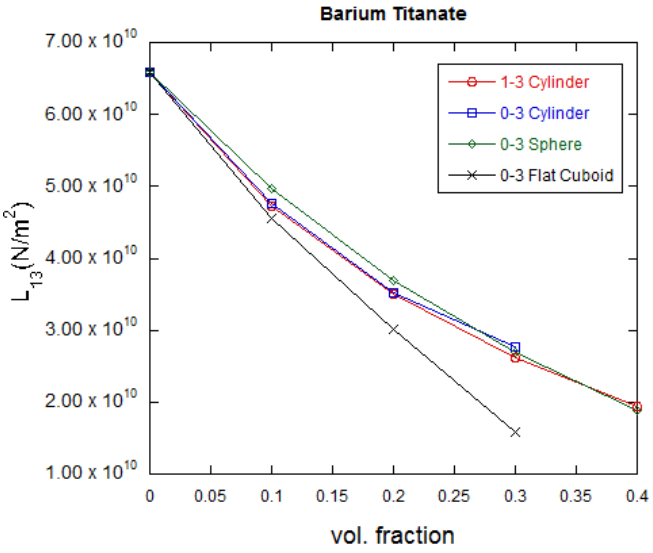

(a)

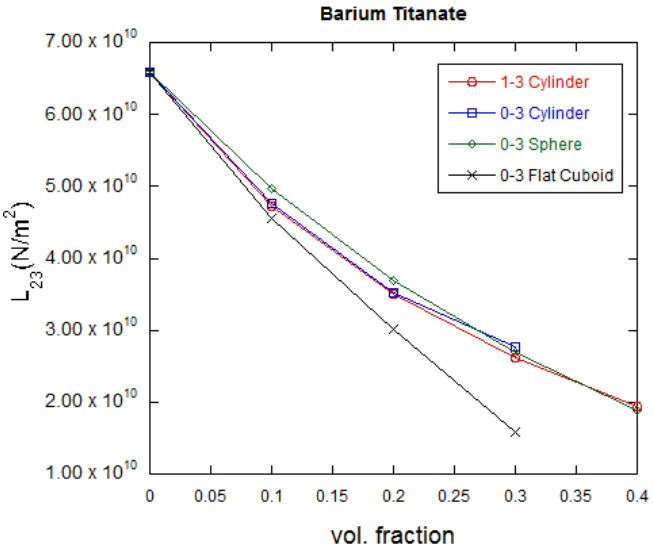

(b)

Figure 26: Trends showing the finite-element results for Barium Titanate-3.

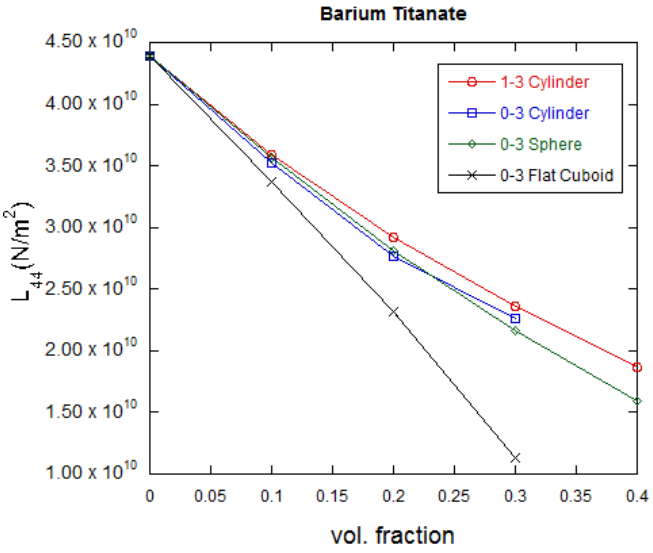

(a)

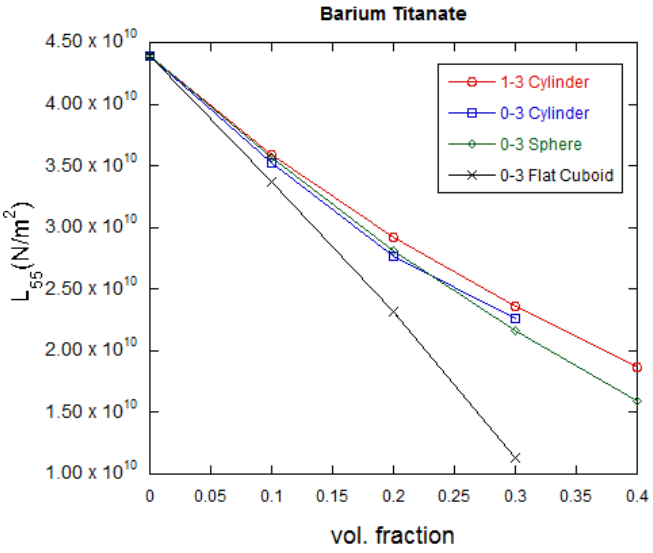

(b)

Figure 27: Trends showing the finite-element results for Barium Titanate-4.

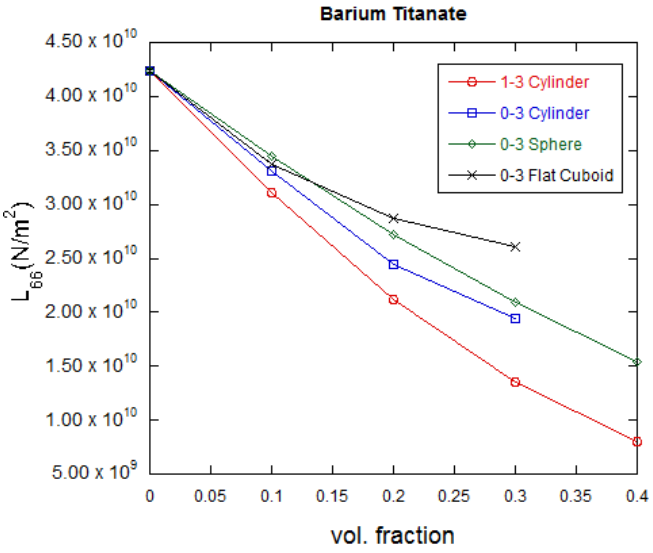

(a)

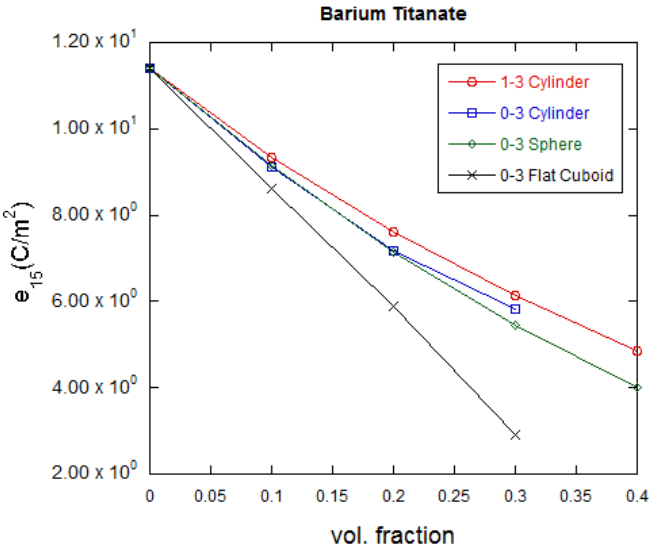

(b)

Figure 28: Trends showing the finite-element results for Barium Titanate-5.

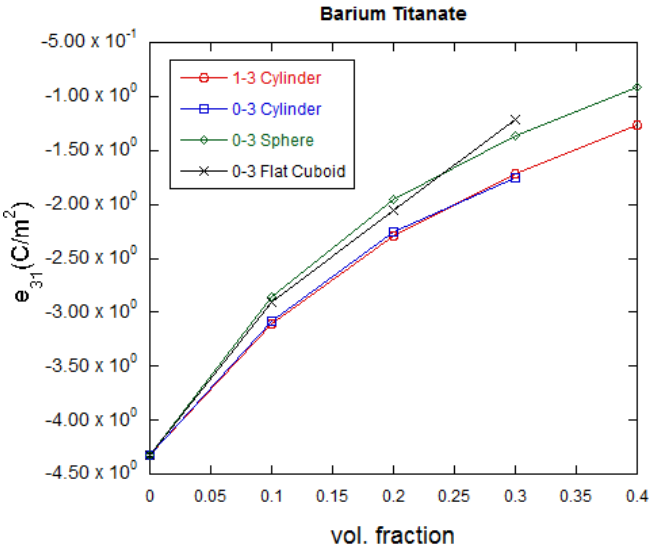

(a)

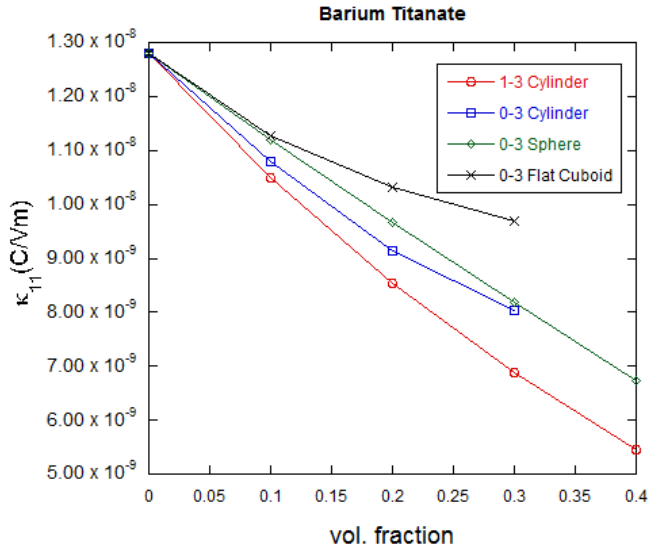

(b)

Figure 29: Trends showing the finite-element results for Barium Titanate-6.

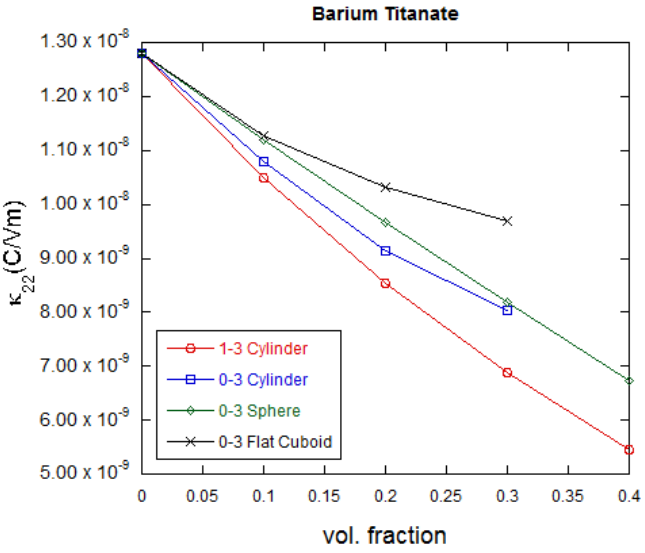

(a)

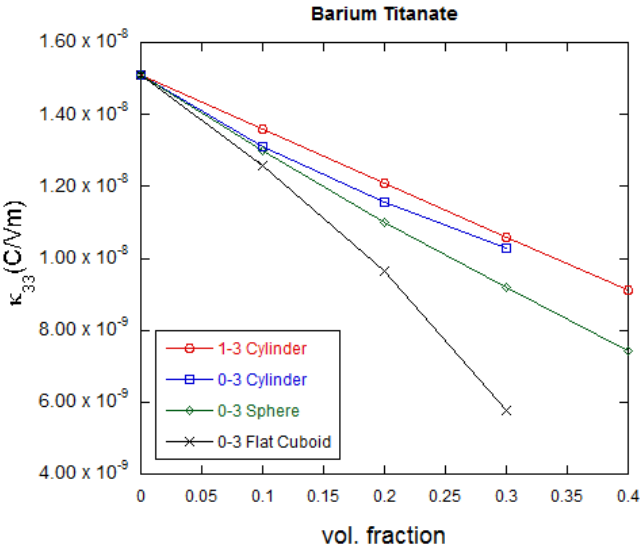

(b)

Figure 30: Trends showing the finite-element results for Barium Titanate-7.

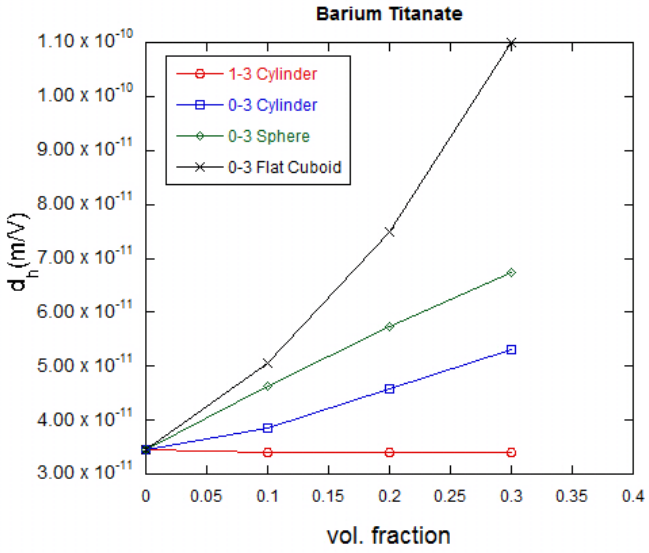

(a)

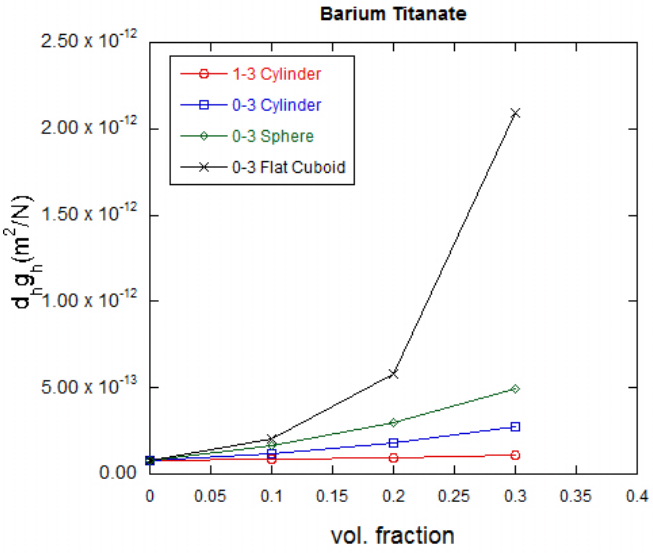

(b)

Figure 31: Trends showing the Figures of merit for Barium Titanate-2.

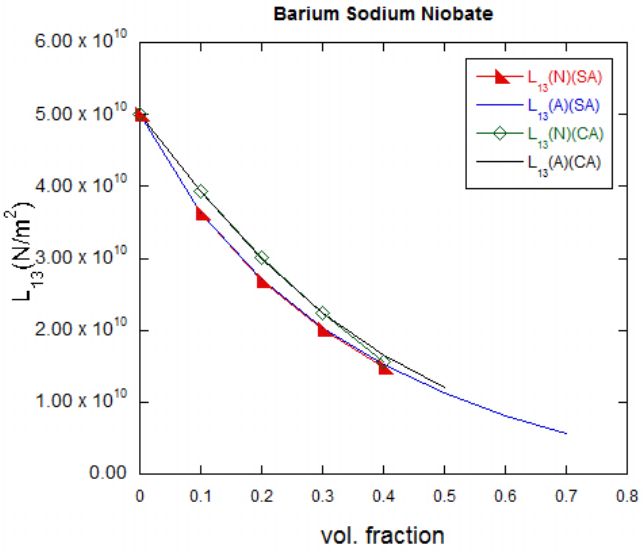

(a)

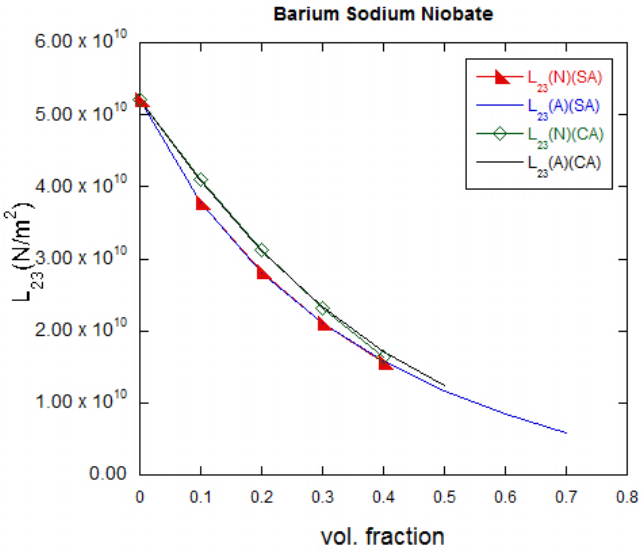

(b)

Figure 32: Trends showing the variation of elastic constants for Barium Sodium Niobate-3.

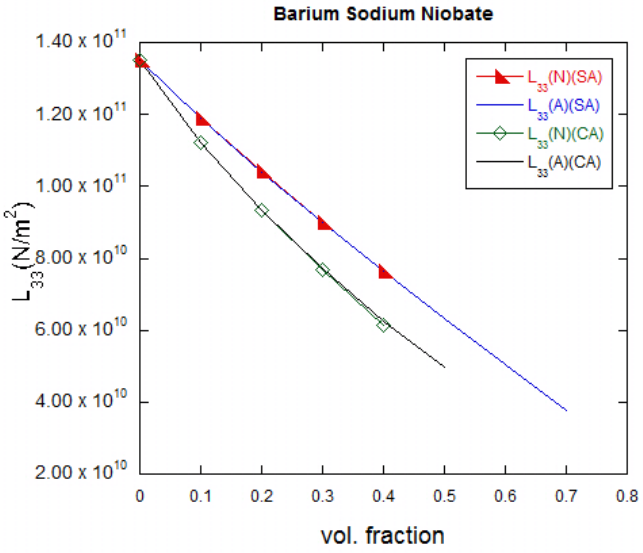

(a)

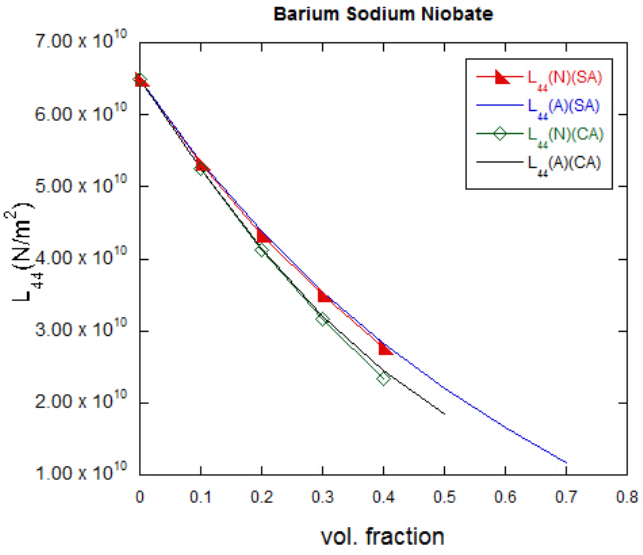

(b)

Figure 33: Trends showing the variation of elastic constants for Barium Sodium Niobate-4.

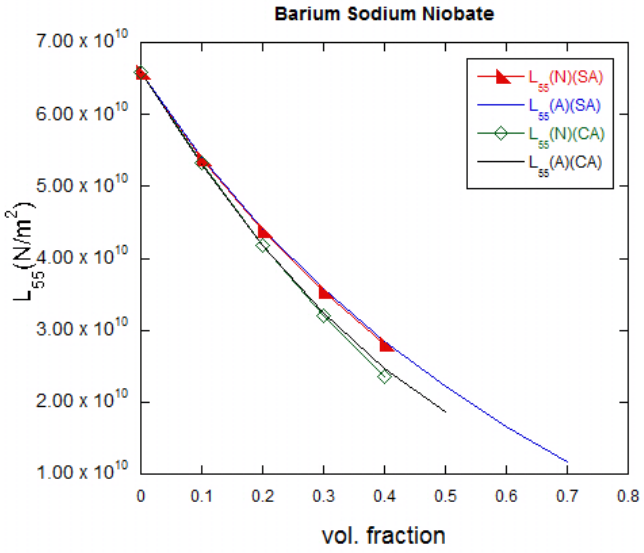

(a)

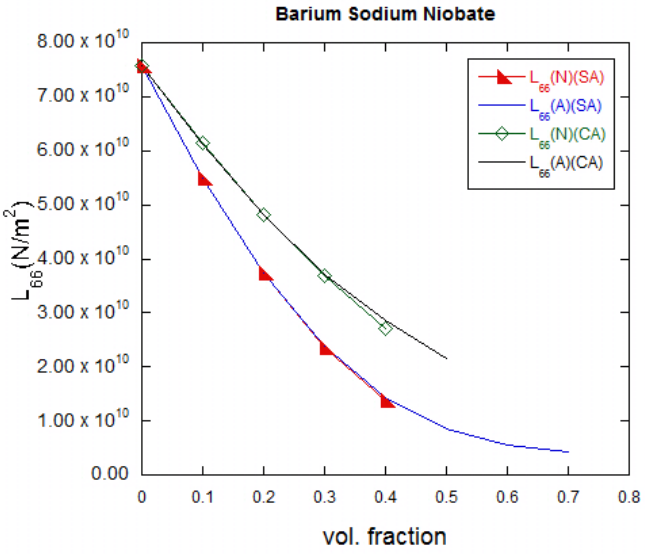

(b)

Figure 34: Trends showing the variation of elastic constants for Barium Sodium Niobate-5.

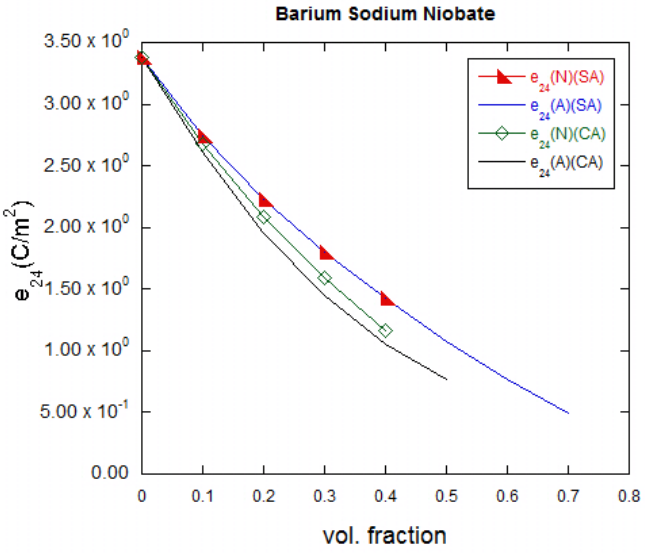

(a)

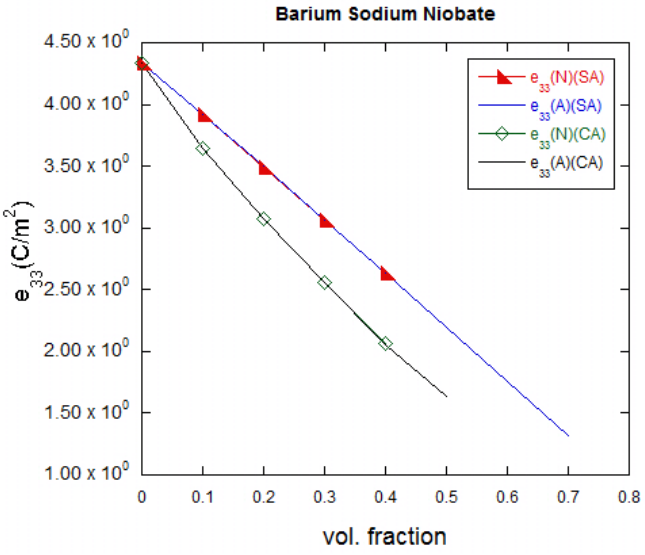

(b)

Figure 35: Trends showing the variation of piezoelectric constants for Barium Sodium Niobate-6.

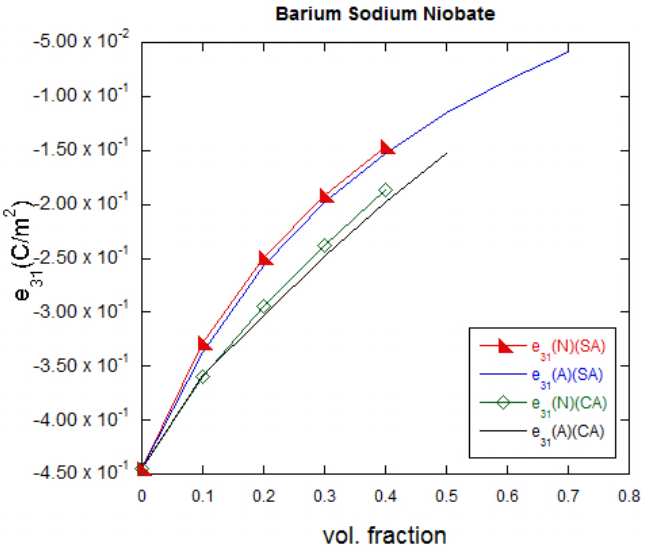

(a)

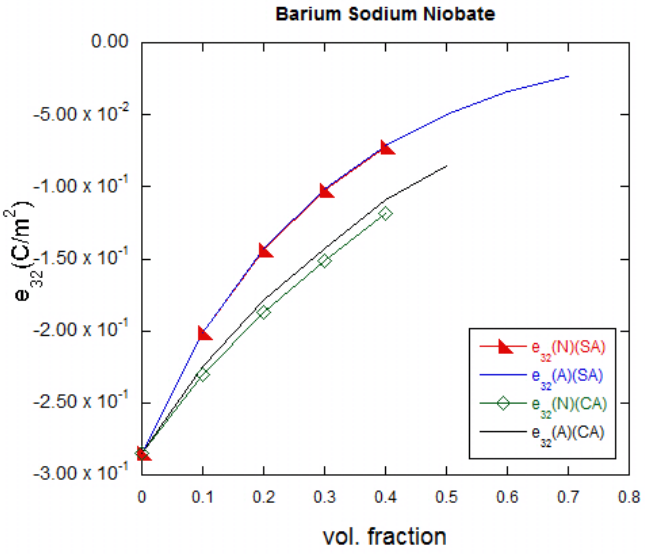

(b)

Figure 36: Trends showing the variation of piezoelectric constants for Barium Sodium Niobate-7.

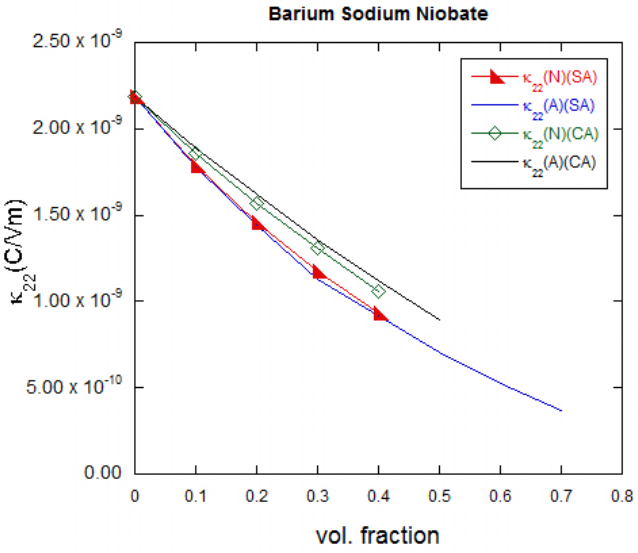

(a)

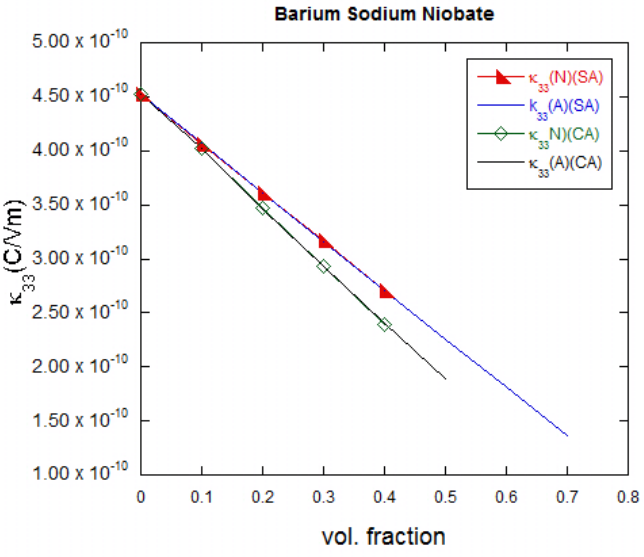

(b)

Figure 37: Trends showing the variation of dielectric constants for Barium Sodium Niobate-8.

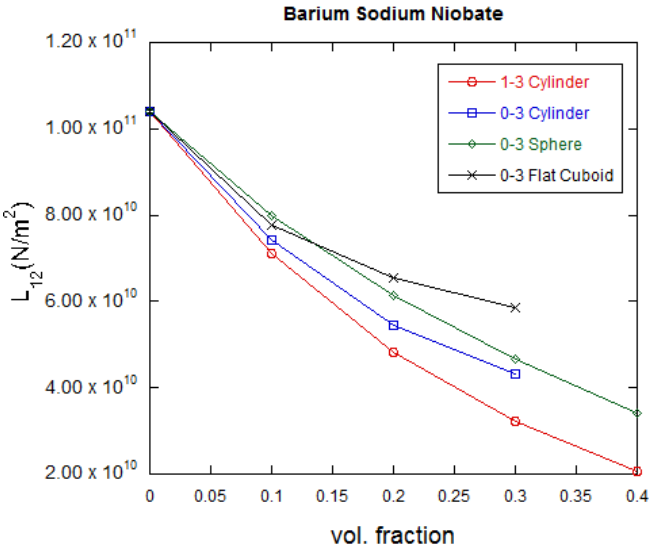

(a)

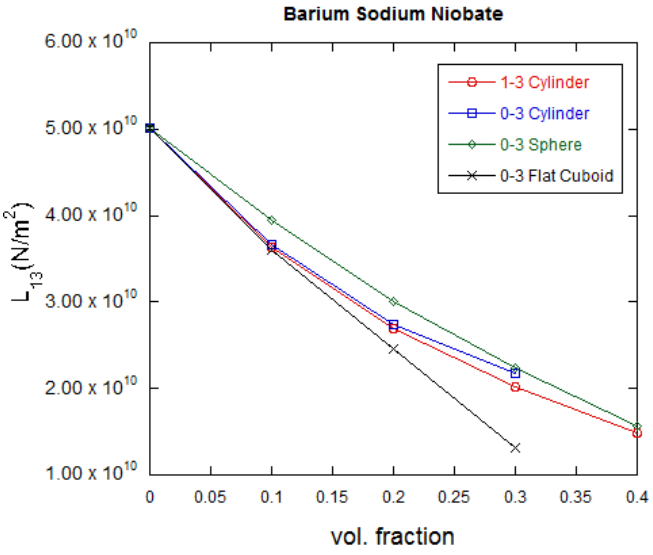

(b)

Figure 38: Trends showing the finite-element results for Barium Sodium Niobate-2.

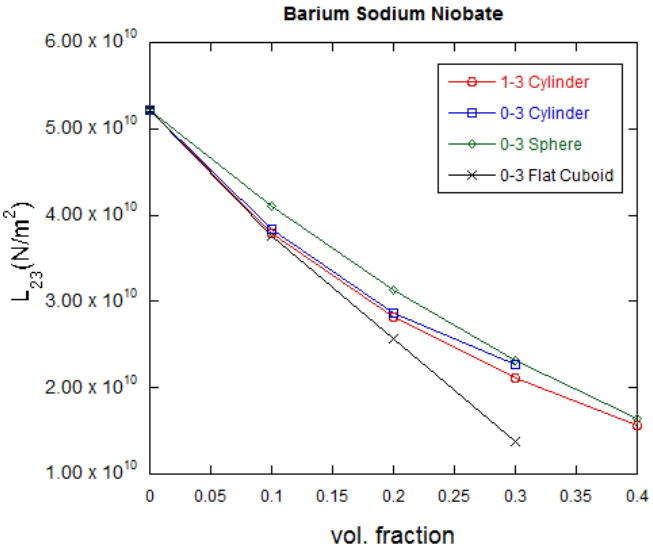

(a)

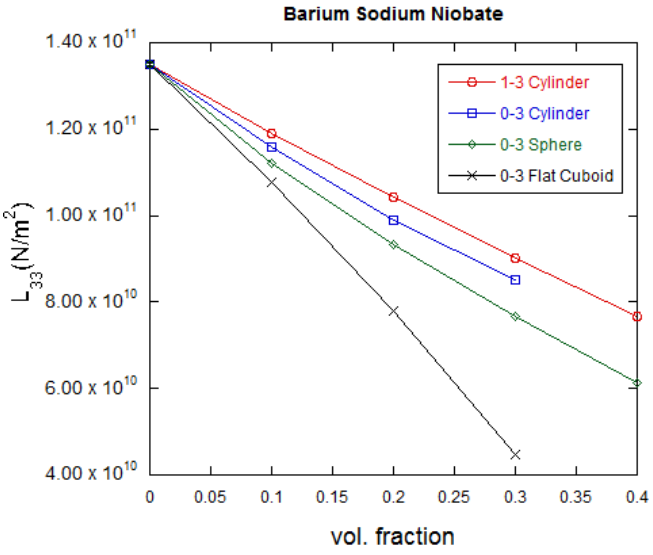

(b)

Figure 39: Trends showing the finite-element results for Barium Sodium Niobate-3.

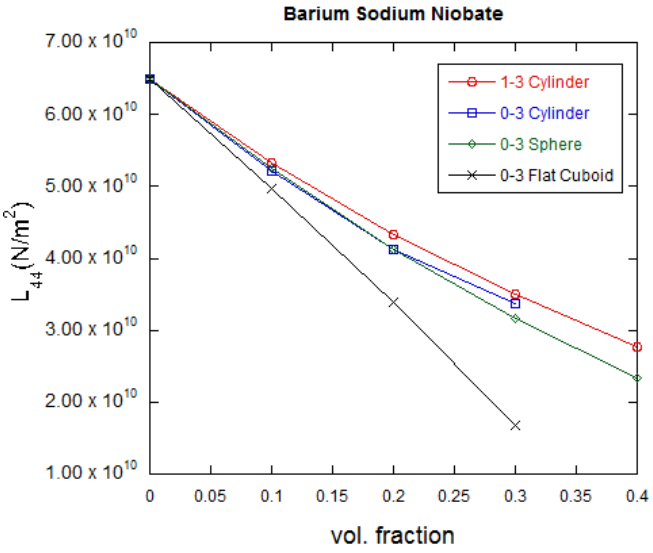

(a)

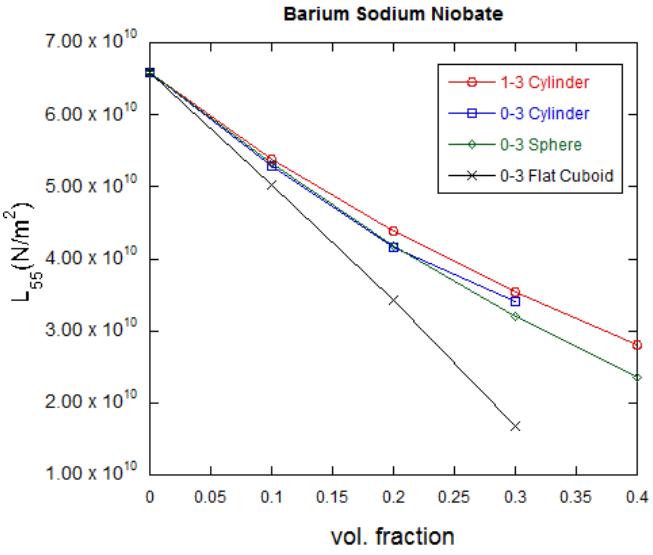

(b)

Figure 40: Trends showing the finite-element results for Barium Sodium Niobate-4.

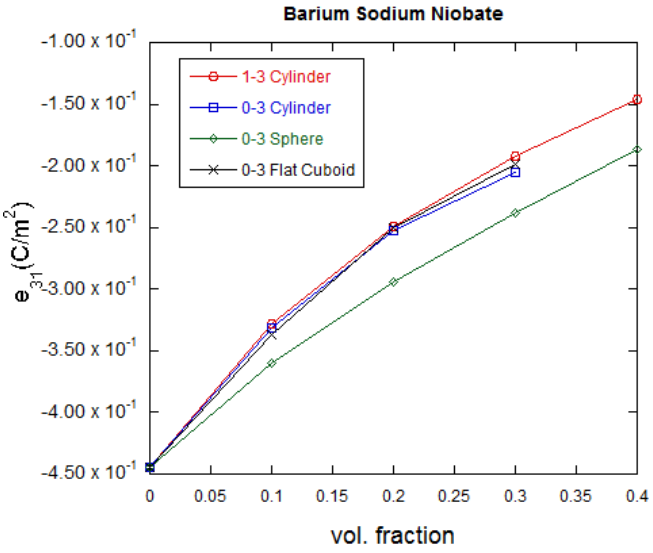

(a)

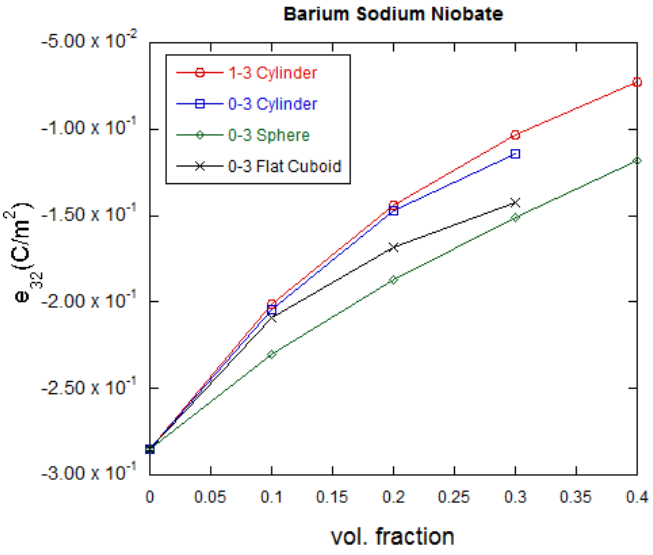

(b)

Figure 41: Trends showing the finite-element results for Barium Sodium Niobate-5.

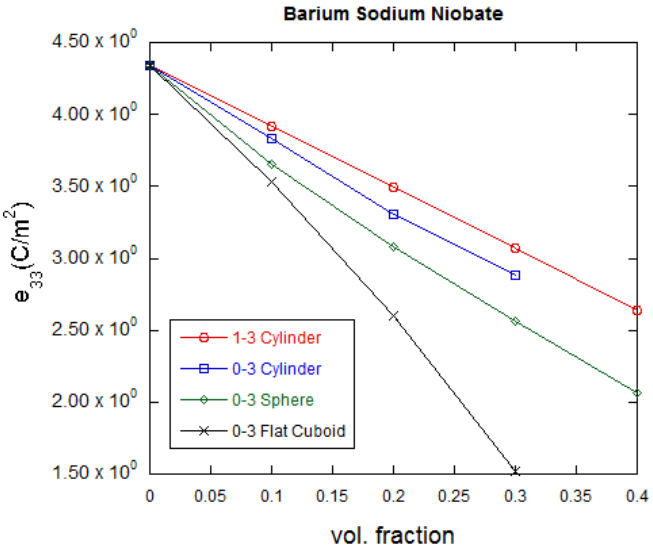

(a)

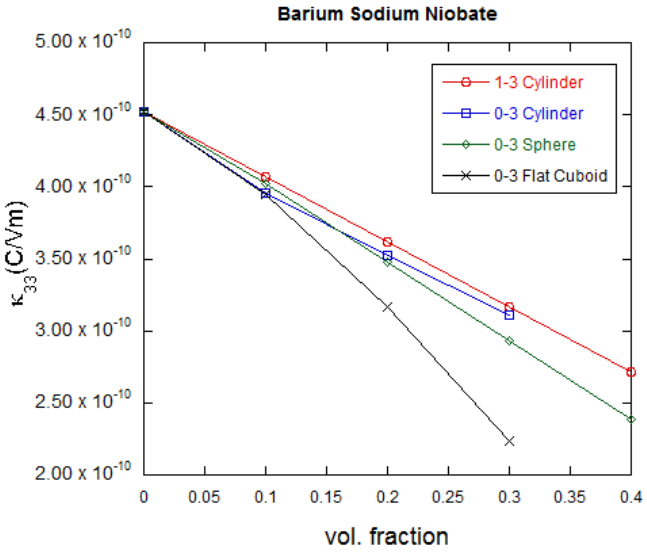

(b)

Figure 42: Trends showing the finite-element results for Barium Sodium Niobate-6.

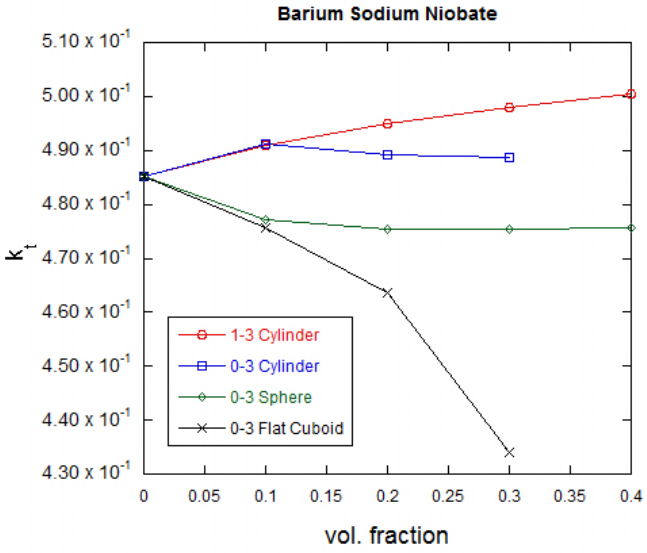

(a)

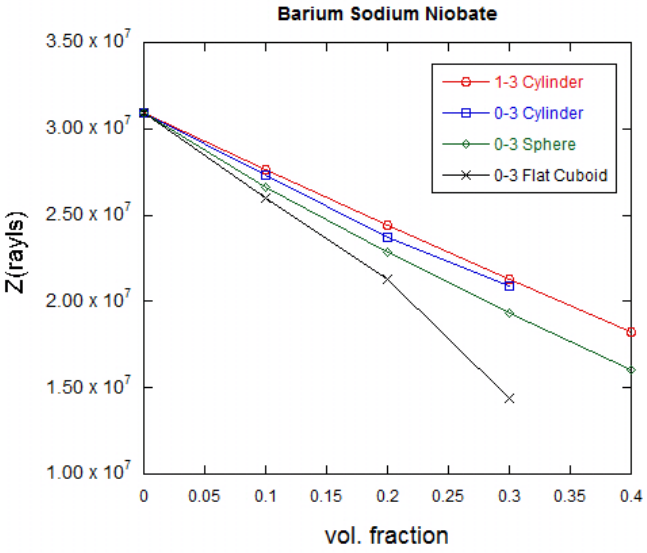

(b)

Figure 43: Trends showing the Figures of merit for Barium Sodium Niobate-2

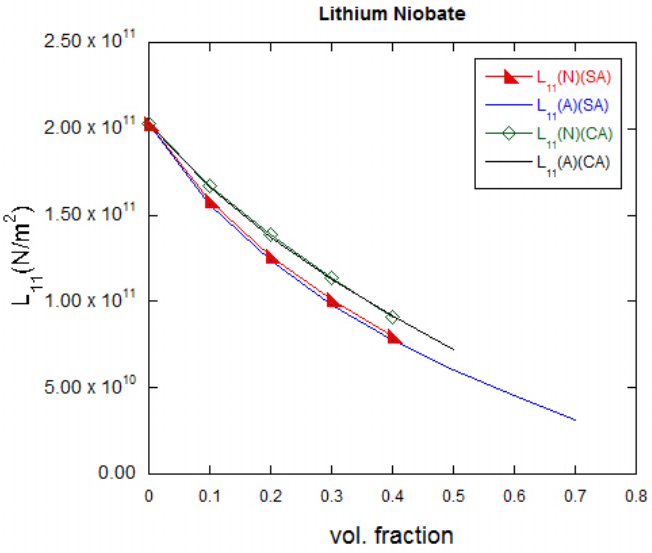

(a)

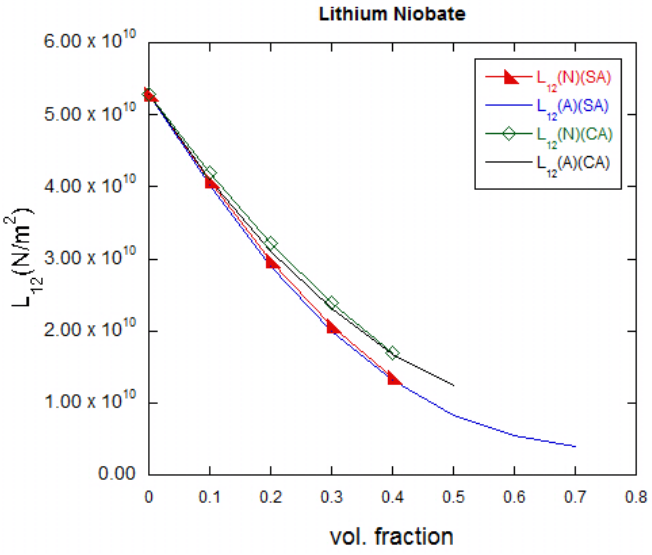

(b)

Figure 44: Trends showing the variation of elastic constants for Lithium Niobate-2.

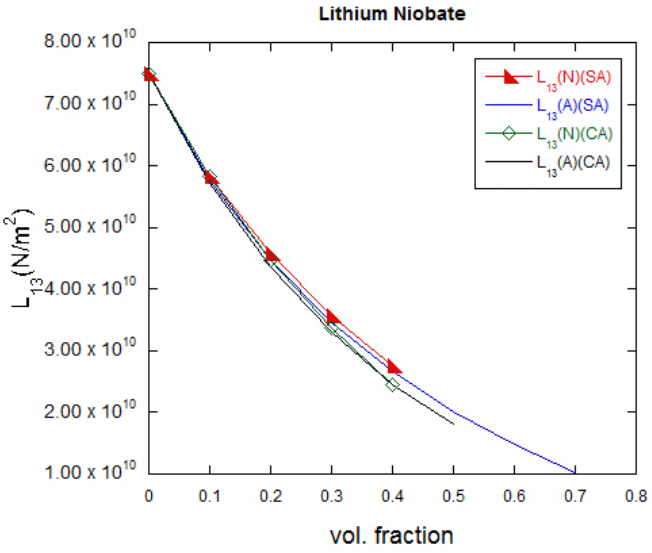

(a)

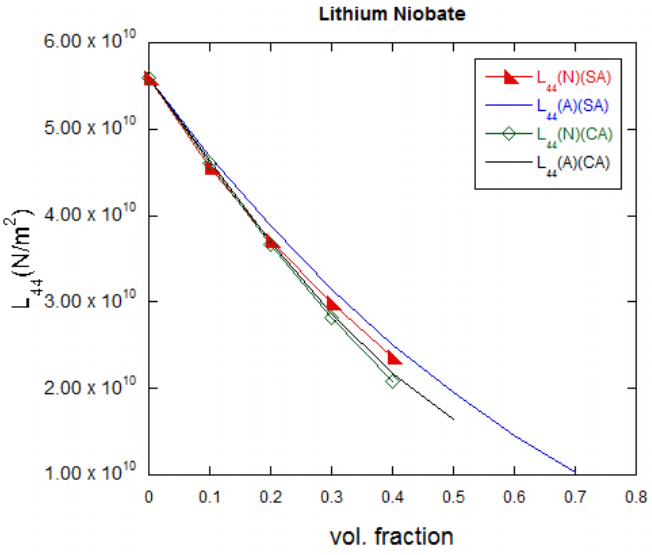

(b)

Figure 45: Trends showing the variation of elastic constants for Lithium Niobate-3.

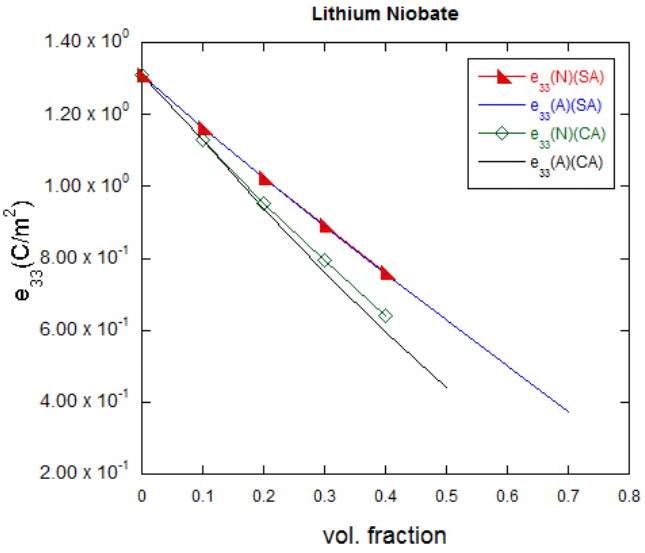

(a)

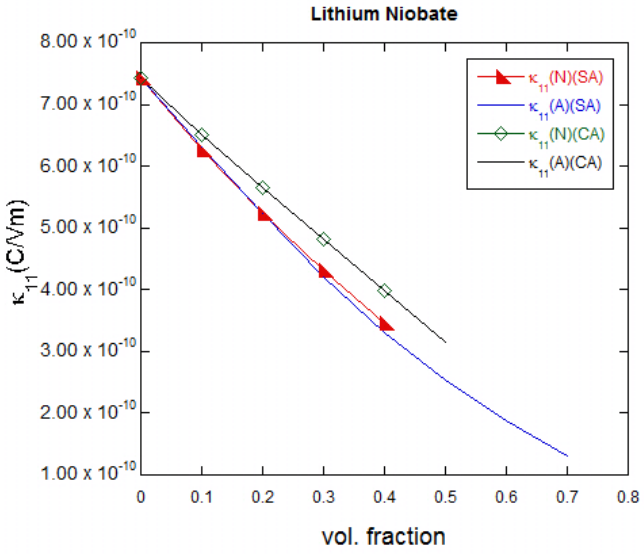

(b)

Figure 46: Trends showing the variation of piezoelectric and dielectric constants for Lithium Niobate-2.

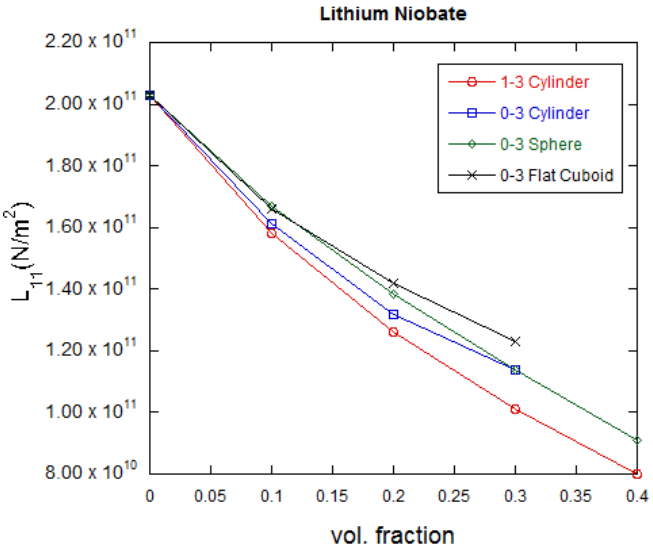

(a)

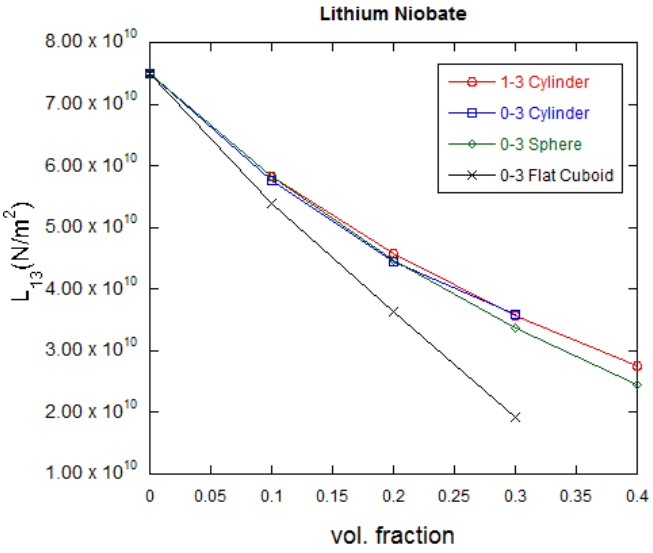

(b)

Figure 47: Trends showing the finite-element results for Lithium Niobate-2

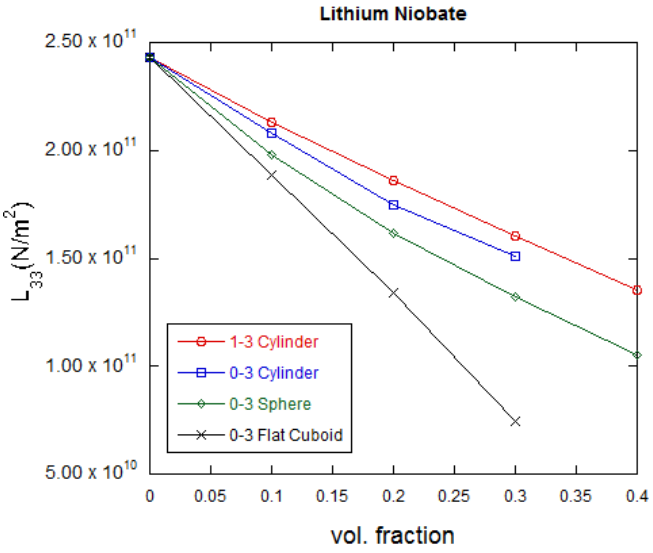

(a)

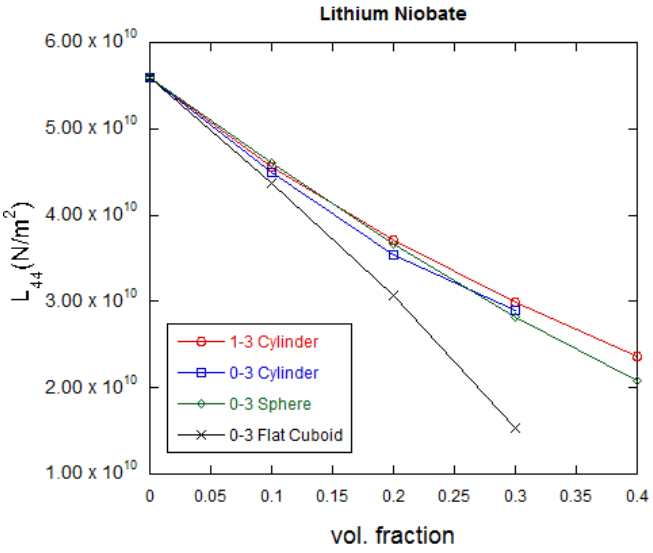

(b)

Figure 48: Trends showing the finite-element results for Lithium Niobate-3

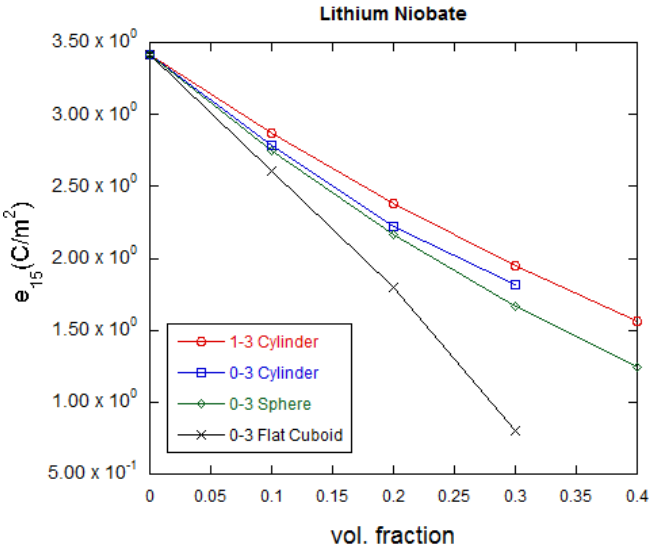

(a)

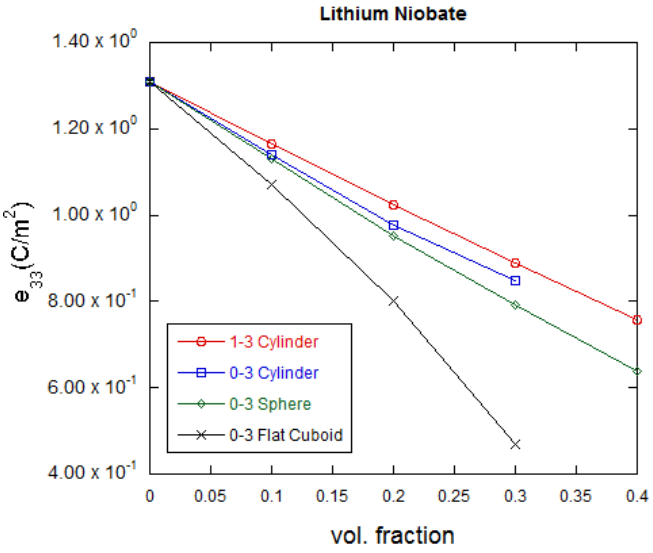

(b)

Figure 49: Trends showing the finite-element results for Lithium Niobate-4

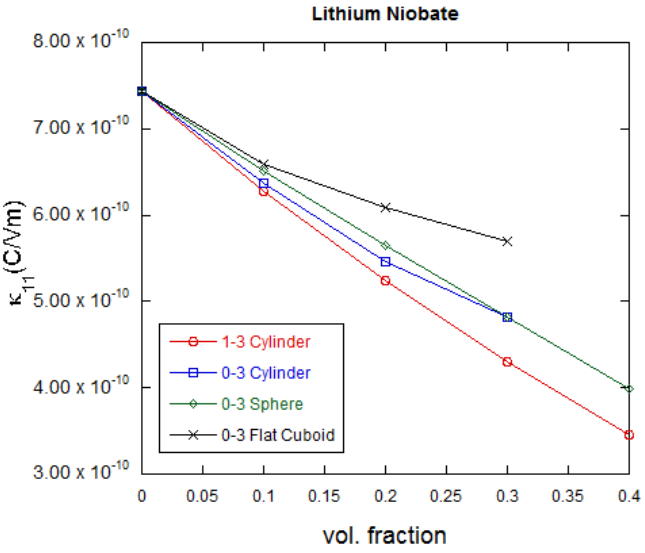

(a)

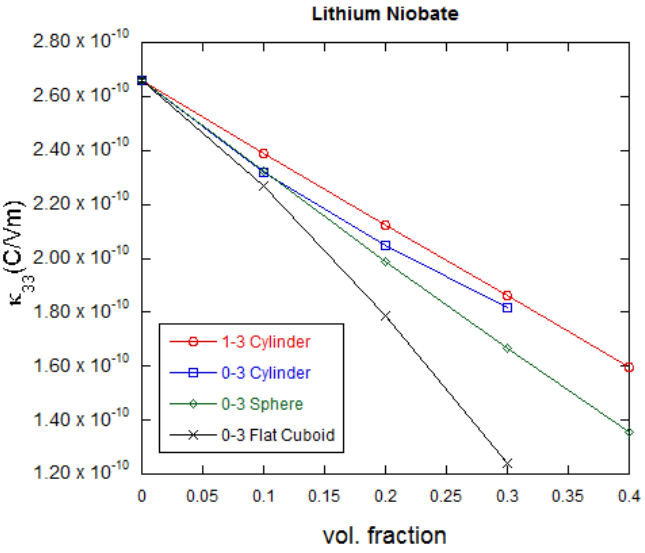

(b)

Figure 50: Trends showing the finite-element results for Lithium Niobate-5

Bibliography

[1] T. E. G. Alavarez-Arenas and F. M. Espinosa. Highly coupled dielectric behavior of porous ceramics embedding a polymer. *Applied Physics Letters*, 68:263–265, 1996.

[2] H. Banno. Effects of shape and volume fraction of closed pores on dielectric, elastic and electromechanical properties of dielectric and piezoelectic ceramics - a theoretical approach. *American Ceramic Society Bulletin*, 66:1332, 1987.

[3] U. Bast and W. Wersing. The influence of internal voids with 31 connectivity on the properties of piezoelectric ceramics prepared by a new planar process. *Ferroelectrics*, 94:229, 1989.

[4] Y. Benveniste. The determination of the elastic and electric fields in a piezoelectric inhomogeneity. *Journal of Applied Physics*, 72:1086–1095, 1992.

[5] P. Bisegna and R. Luciano. Variational bounds for the overall properties of piezoelectric composites. *Journal of the Mechanics and Physics of Solids*, 44:583–602, 1996.

[6] P. Bisegna and R. Luciano. On methods for bounding the overall properties of periodic piezoelectric fibrous composites. *Journal of the Mechanics and Physics of Solids*, 45:1329–1356, 1997.

[7] C. Bowen and V. Topolov. Piezoelectric sensitivity of pbtio3-based ceramic/polymer composites with 03 and 33 connectivity. *Acta Materialia*, 51:4965–4976, 2003.

[8] G. A. C. and D. C. Lagoudas. On the numerical evaluation of eshelby's tensor and its application to elastoplastic fibrous composite. *Computational Mechanics*, 7:13–19, 1990.

[9] T. Chen. Green's functions and the non-uniform transformation problem in a piezoelectric medium. *Mechanics Research Communications*, 20:271–278, 1993a.

[10] W. F. J. Deeg. *The analysis of dislocation, crack, and inclusion problems in piezoelectric solids*. PhD thesis, Stanford Univ., CA., 1980.

[11] M. L. Dunn and M. Taya. An analysis of piezoelectric composite materials containing ellipsoidal inhomogeneities. *Proceedings of The Royal Society A*, 443:265–287, 1993.

[12] M. L. Dunn and M. Taya. Electromechanical properties of porous piezoelectric ceramics. *Journal of the American Ceramic Society*, 76:1697–1706, 1993.

[13] M. L. Dunn and H. A. Wienecke. Inclusions and inhomogeneities in transversely isotropic piezoelectric solids. *International Journal of Solids and Structures*, 34:3571–3582, 1997.

[14] J. D. Eshelby. The determination of the elastic field of an ellipsoidal inclusion, and related problems. *Proceedings of the Royal Society of London. Series A, Mathematical and Physical Sciences*, 241:376–396, 1957.

[15] K. Y. Hashimoto and M. Yamaguchi. Elastic, piezoelectric and dielectric properties of composite materials. *IEEE 1986 Ultrasonics Symposium*, 0.1109/ULTSYM.1986.198824:697–702, 1986.

[16] R. Hill. Discontinuity relations in mechanics of solids. *Progress Solid Mechanics*, 2:245–276, 1961.

[17] M. J. Huan and R. E. Newnham. An experimental and theoretical study of 1-3 and 1-3-0 piezoelectric pzt-polymer composites for hydrophone applications. *Ferroelectrics*, 68:123–139, 1986.

[18] S. Iyer and T. A. Venkatesh. Electromechanical response of porous piezoelectric materials: Effects of porosity connectivity. *Applied Physics Letters*, 97(7):072904–1–3, Aug. 2010.

[19] R. Kar-Gupta, C. Marcheselli, and T. A. Venkatesh. Electromechanical response of 13 piezoelectric composites: Effect of fiber shape. *Journal OF Applies Physics*, 104:024105–1–17, 2008.

[20] R. Kar-Gupta and T. Venkatesh. Electromechanical response of 1-3 piezoelectric composites: Effect of poling characteristics. *Applied Physics Letters*, 98:054102–1–3, 2005.

[21] R. Kar-Gupta and T. Venkatesh. Electromechanical response of porous piezoelectric materials. *Acta Materialia*, 54:4063–4078, 2006.

[22] R. Kar-Gupta and T. Venkatesh. Electromechanical response of porous piezoelectric materials: Effects of porosity distribution. *Applied Physics Letters*, 97:062904–1–3, 2007.

[23] R. Kar-Gupta and T. Venkatesh. Electromechanical response of piezoelectric composites: Effects of geometric connectivity and grain size. *Acta Materialia*, 56:3810–3823, 2008.

[24] N. Kinoshita and T. Mura. Elastic fields of inclusions in anisotropic media. *physica status solidi (a)*, 5:759–768, 1971.

[25] F. Levassort, M. Lethiecq, Member, IEEE, D. Certon, and F. Patat. A matrix method for modeling electroelastic moduli of 0-3 piezo-composites. *IEEE Transactions on Ultrasonics, Ferroelectrics, and Frequency Control*, 44:445–452, 1997.

[26] F. Levassort, M. Lethiecq, Member, IEEE, R. Desmare, and L. P. Tran-Huu-Hue. Effective electroelastic moduli of 3-3(0-3) piezocomposites.

IEEE Transactions on Ultrasonics, Ferroelectrics, and Frequency Control, 46:1028–1034, 1999.

[27] F. Levassort, M. Lethiecq, Member, IEEE, C. Millar, and L. Pourcelot. Modeling of highly loaded 0-3 piezoelectric composites using a matrix method. *IEEE Transactions on Ultrasonics, Ferroelectrics, and Frequency Control*, 45:1497–1505, 1998.

[28] F. Levassort, V. Y. Topolov, and M. Lethiecq. A comparative study of different methods of evaluating effective electromechanical properties of 0-3 and 1-3 ceramic/polymer composites. *Journal of Physics D: Applied Physics*, 33:2064–2068, 2000.

[29] J. Michel, H. Moulinec, and P. Suquet. Effective properties of composite materials with periodic microstructure: a computational approach. *Computer Methods in Applied Mechanics and Engineering*, 172:109–143, 1999.

[30] Y. Mikata. Determination of piezoelectric eshelby tensor in transversely isotropic piezoelectric solids. *International Journal of Engineering Science*, 38:605–641, 2000.

[31] Y. Mikata. Explicit determination of piezoelectric eshelby tensors for spheroidal inclusion. *International Journal of Solids and Structures*, 38:7045–7063, 2001.

[32] R. Newnham, D. Skinner, and L. Cross. Connectivity and piezoelectric-pyroelectric composites. *Materials Research Bulletin*, 13:525–536, 1978.

[33] J. F. Nye. *Physical properties of crystals : their representation by tensors and matrices*. Oxford [Oxfordshire] : Clarendon Press ; New York : Oxford University Press, 1984.

[34] H. E. Pettermann and S. Suresh. A comprehensive unit cell model: a study of coupled effects in piezoelectric 1-3 composites. *International Journal of Solids and Structures*, 37:5447–5464, 2000.

[35] H. Taunaumang, I. L. Guy, and H. L. W. Chan. Electromechanical properties of 1-3 piezoelectric ceramic/piezoelectric polymer composites. *Journal of Applied Physics*, 76:484–489, 1994.

[36] R. Y. Ting. Piezoelectric properties of a porous pzt ceramic. *Ferroelectrics*, 65:11–20, 1985.

[37] L. J. Walpole. The elastic field of an inclusion in an anisotropic medium. *Proceedings of the Royal Society of London. Series A, Mathematical and Physical Sciences*, 300:270–289, 1967.

[38] L. J. Walpole. The determination of the elastic field of an ellipsoidal inclusion in an anisotropic medium. *Mathematics Proceedings of the Cambridge Philosophical Society*, 81:283–289., 1977.

[39] B. Wang. Three-dimensional analysis of an ellipsoidal inclusion in a piezoelectric material. *International Journal of Solids and Structures*, 29:293–308, 1992.

[40] Q. Xu, S. Chen, W. Chen, S. Wu, J. Zhou, H. Sun, and Y. Li. Synthesis and piezoelectric and ferroelectric properties of $(Na_{0.5}Bi_{0.5})_{1-x}Ba_xTiO_3$ ceramics. *Materials Chemistry and Physics*, 90:111–115, 2005.